A global apparent polar wander path for the last 320 Ma calculated from site-level paleomagnetic data

Bram Vaes[a*], Douwe J.J. van Hinsbergen[a], Suzanna H.A. van de Lagemaat[a], Erik van der Wiel[a], Nalan Lom[a], Eldert L. Advokaat[a,b], Lydian M. Boschman[a], Leandro C. Gallo[c], Annika Greve[a], Carl Guilmette[d], Shihu Li[e], Peter C. Lippert[f], Leny Montheil[g], Abdul Qayyum[a], Cor G. Langereis[a]

[a]Department of Earth Sciences, Faculty of Geosciences, Utrecht University, Utrecht, The Netherlands

[b]School of Geography, Earth and Environmental Sciences, University of Birmingham, United Kingdom

[c]Centre for Earth Evolution and Dynamics (CEED), University of Oslo, Oslo, Norway

[d]Géologie et Génie Géologique, Université Laval, Québec City, Quebec, Canada

[e]State Key Laboratory of Lithospheric Evolution, Institute of Geology and Geophysics, Chinese Academy of Sciences, Beijing, 100029, China

[f]Department of Geology and Geophysics, University of Utah, Salt Lake City, United States of America

[g]Géosciences Montpellier, CNRS-Université de Montpellier-Université des Antilles, F-34095 Montpellier, France

* Corresponding author (B. Vaes: b.vaes@uu.nl)

Highlights

- New paleomagnetic reference frame for the last 320 million years
- Global apparent polar wander path computed from site-level data rather than poles
- First-order geometry similar to previous models but with smaller uncertainties
- Peaks in apparent polar wander may result from a temporal bias in the data
- Future improvement of the reference frame requires new, high-quality data

Key words: paleomagnetism, apparent polar wander path, paleogeography, paleomagnetic pole, reference frame, paleolatitude, plate reconstruction

Abstract

Apparent polar wander paths (APWPs) calculated from paleomagnetic data describe the motion of tectonic plates relative to the Earth's rotation axis through geological time, providing a quantitative paleogeographic framework for studying the evolution of Earth's interior, surface, and atmosphere. Previous APWPs were typically calculated from collections of paleomagnetic poles, with each pole computed from collections of paleomagnetic sites, and each site representing a spot reading of the paleomagnetic field. It was recently shown that the choice of how sites are distributed over poles strongly determines the confidence region around APWPs and possibly the APWP itself, and that the number of paleomagnetic data used to compute a single paleomagnetic pole varies widely and is essentially arbitrary. Here, we use a recently proposed method to overcome this problem and provide a new global APWP for the last 320 million years that is calculated from simulated site-level paleomagnetic data instead of from paleopoles, in which spatial and temporal uncertainties of the original datasets are incorporated. We provide an updated global paleomagnetic database scrutinized against quantitative, stringent quality criteria, and use an updated global plate motion model. The new global APWP follows the same trend as the most recent pole-based APWP but has smaller uncertainties. This demonstrates that the first-order geometry of the global APWP is robust and reproducible, indicating that paleomagnetism provides a reliable reference frame as basis for reconstructing, for instance, paleogeography and paleoclimate. Moreover, we find that previously identified peaks in APW rate disappear when calculating the APWP from site-level data and correcting for a temporal bias in the underlying data. Finally, we show that a higher-resolution global APWP frame may be determined for time intervals with high data density, but that this is not yet feasible for the entire 320-0 Ma time span. Future collection of large and well-dated paleomagnetic datasets from stable plate interiors are needed to improve the quality and resolution of the global APWP, which may contribute to solving detailed Earth scientific problems that rely on a paleomagnetic reference frame.

1. Introduction

Paleomagnetism provides one of the principal tools for the quantitative reconstruction of Earth's paleogeography. Paleomagnetic data are used to construct apparent polar wander paths (APWPs) that describe the apparent motion of the paleomagnetic pole relative to a fixed continent or tectonic plate through time (e.g., Creer et al., 1954). Assuming that the time-averaged geomagnetic pole coincides with the Earth's spin axis allows the translation of an APWP into the motion of a continent or plate relative to the geographic pole. By combining paleomagnetic data from all major plates using reconstructions of relative plate motions, a global APWP may be constructed that places a global model of relative plate motions into an 'absolute' reference frame (e.g., Phillips and Forsyth, 1972; Besse and Courtillot, 1991; 2002; Torsvik et al., 2008; 2012). Such a paleomagnetic reference frame is widely used by paleomagnetists to determine relative paleolatitudinal motions or vertical-axis rotations (e.g., Demarest, 1983; Butler, 1992) and also allows the estimation of the paleolatitude

(through time) of any given location on Earth (e.g., van Hinsbergen et al., 2015), providing key input for paleoclimate, paleoenvironment, and paleobiology interpretation. These applications rely on the quality of the underlying global APWP and the robust quantification of its confidence limits. However, there is increasing recognition that the statistical approach used to calculate the widely used (global) APWPs and their uncertainty, which has changed little over the last >60 years, has several shortcomings.

First, the paleomagnetic poles (or paleopoles) that are used as input for APWP construction are commonly assigned equal weight, regardless of the uncertainties in the position of the paleopole or in the age of the rocks from which they were derived. Second, such paleopoles are calculated from widely different, and essentially arbitrary numbers of paleomagnetic sites (Vaes et al., 2022), whereby each site is interpreted to represent a 'spot reading' of the past geomagnetic field (e.g., McElhinny and McFadden, 2000). In previous APWPs, each input paleopole was assumed to have averaged 'out' the paleosecular variation (PSV) of the geomagnetic field, but Vaes et al. (2022) showed that the dispersion of input paleopoles around the most recent global APWP becomes larger with a smaller number of sites, creating a bias towards poles based on smaller datasets with larger uncertainty. Thus, the classical approach allows the calculation of non-unique APWPs with different uncertainties using the same underlying data depending on the subjective choice of how to distribute data over paleopoles (Vaes et al., 2022).

To overcome these problems, APWPs may instead be computed from site-level paleomagnetic data, that is, from virtual geomagnetic poles (VGPs) (e.g., McElhinny et al., 1974; Hansma and Tohver, 2020, van Hinsbergen et al., 2017, Vaes et al., 2022), or by weighting paleopoles against the number of sites (McFadden and McElhinny, 1995). In these approaches, equal weight is assigned to each 'spot reading' of the past geomagnetic field (that is, a site) rather than to each paleopole based on some collection of site-level data (Fig. 1). However, building a database with site-level data for the many hundreds of studies that reported relevant input data is not straightforward as paleomagnetic data is not always reported at the site-level, particularly in older publications, and it would require an enormous effort to compile those that are only listed in the original publication and not in databases such as MagIC (Jarboe et al., 2012). Vaes et al. (2022) recently introduced an alternative approach: they showed that when site-level data are parametrically re-sampled from reported paleopoles and their statistical parameters, a distribution of synthetic VGPs may be obtained that provides an accurate, albeit conservative approximation (i.e., with a somewhat larger dispersion) of the original data. This approach thus provides a promising avenue to use published paleomagnetic poles to compute APWPs from site-level data, allowing the incorporation of key uncertainties in the construction of APWPs as well as the weighting of datasets against the number of sites. Although recent studies have incorporated key sources of uncertainty, such as spatial and age uncertainties, in the computation of an APWP (e.g., Swanson-Hysell et al., 2019; Hansma and Tohver, 2020; Gallo et al., 2021; Wu et al., 2021), this has not yet been applied to the computation of a global APWP.

In this study, we compute the first global apparent polar wander from site-level paleomagnetic data, for the last 320 Ma, in which the key uncertainties in the underlying paleomagnetic datasets, in position and age, are incorporated and weighted. To transfer paleomagnetic data to a common reference plate, we use an updated global plate circuit that includes the most recent marine geophysics-based ocean basin reconstructions. We also provide an updated paleomagnetic database that updates the compilation of Torsvik et al. (2012). We have filtered that database using stringent, statistics-based, quantitative quality criteria and have extended the database with new, high-quality paleomagnetic datasets from stable plate interiors that have been published in the last decade. We also compiled data from regions that were previously not incorporated, such as the China Blocks, Iberia, and the Antarctic Peninsula, for the time period during which their motions relative to major tectonic plates are determined independently of paleomagnetism. We compute a global APWP from parametrically re-sampled VGPs at a 10 Ma resolution using a 20 Ma time window. We first evaluate whether there is reason to suspect that the obtained distributions of re-sampled VGPs are affected by biases in the underlying data (e.g., due to overlooked tectonic rotations or plate reconstruction errors). Next, we compare the new APWP with previous global APWPs that were based on paleopoles and highlight differences between them. In addition, we evaluate how the geometry of the new global APWP, and the rates of apparent polar wander, are influenced by the chosen temporal resolution of the path. Finally, we provide an outlook for the future construction of APWPs and highlight opportunities for improving the quality and resolution of the paleomagnetic reference frame.

2. Background

2.1 History of APWP computation

The paleogeographic and tectonic applications of paleomagnetism rely on the key assumption that the Earth's time-averaged magnetic field closely resembles that of a geocentric axial dipole (GAD) field, such that the position of the geomagnetic pole coincides with the Earth's rotation axis (e.g., Runcorn, 1959; Butler, 1992; Johnson and McFadden, 2007). The GAD hypothesis was already applied by Hospers (1954) and Creer et al. (1954) to determine the position of the past paleomagnetic pole relative to the sampling locations of rocks from different geological periods. One of the main advantages of assuming a dipolar field structure is that it provides a simple relationship between the paleomagnetic inclination and the paleolatitude of the location from which the paleomagnetic samples are derived: the so-called dipole formula (e.g., Runcorn, 1959; Irving, 1964). Most studies that investigated the nature of the past geomagnetic field find that the Earth's magnetic field is not a perfect geocentric axial dipole, and non-dipolar contributions to the past geomagnetic field have been estimated to be on the order of up to 5% (e.g., Butler, 1992; Besse and Courtillot, 2002; Bono et al., 2020). However, the axial dipole contribution to the field is considered to be dominant, and it has now been widely accepted that the time-averaged geomagnetic field is well-approximated by a GAD field

since at least mid-Carboniferous times (e.g., Butler, 1992; McElhinny and McFadden, 2000; Johnson and McFadden, 2007; Biggin et al., 2020).

The application of the GAD assumption allows the determination of the position of the geographic pole relative to a fixed plate or continent. When the position of the time-averaged paleomagnetic pole, as a proxy for the geographic pole, is plotted for different moments in the geological past, it seems to 'wander' relative to the present-day geographic pole position, as first observed by Creer et al. (1954). This 'apparent' polar wander reflects the motion of the plate or continent relative to the Earth's rotation axis, providing an 'absolute' frame of reference for past plate tectonic motions. This motion is the combined result of two processes: plate tectonic motion relative to the rotation axis and the rotation of the entire crust-mantle system relative to the rotation axis; the latter known as true polar wander (TPW, e.g., Goldreich and Toomre, 1969; Gordon and Livermore, 1987; Evans, 2003). It is important to note that while APWPs provide quantitative constraints on the paleolatitude and azimuthal orientation of tectonic and plates and continents through geological time, they do not provide any constraints on paleolongitude, due to the symmetrical structure of the assumed GAD field.

Apparent polar wander paths are constructed as a time series of paleomagnetic reference poles relative to the coordinate frame of a chosen reference plate (Fig. 1). Calculating an APWP requires a method to compute these reference poles by combining, averaging, or fitting available paleomagnetic data derived from rocks of different ages (e.g., McElhinny and McFadden, 2000; Tauxe et al., 2010). Creer et al. (1954) constructed the first APWP by connecting a sequence of individual paleomagnetic poles derived from rocks of different geological epochs sampled on the British Isles. But with the publication of an increasing number of 'study mean' paleopoles from rocks with overlapping ages in the following decades, reference poles were calculated by averaging available paleopoles from a given geological period (e.g., Irving, 1964, Phillips and Forsyth, 1972, Van der Voo and French, 1974). Since the late 1970s, the continuous increase in the amount of data allowed the construction of APWPs at a higher resolution by averaging paleopoles that fall within a chosen time window that was shorter than (most) geological time periods using a running mean (or sliding window) (e.g., Irving, 1977, 1979; Van Alstine and De Boer, 1978, Harrison and Lindh, 1982). This approach is appealing because of its simplicity and reproducibility (e.g., Torsvik et al., 2008), and was also used to compute the most widely used global APWPs of the last two decades (Besse and Courtillot, 2002; Kent and Irving, 2010; Torsvik et al., 2008; 2012). These APWPs were calculated at a 10 Ma interval by averaging paleopoles whose mean rock age falls within a 20 Ma sliding window centered on that age. The paleomagnetic data used to compute an APWP may be derived either from a single continent, tectonic plate, or geological terrane, or from multiple continents or plates. The advent of high-resolution global plate tectonic reconstructions enabled paleomagnetists to rotate paleomagnetic data from all the major tectonic plates and continents into a common reference plate, providing a 'global' APWP that describes the motion of all plates and geological terranes that are linked by the plate motion model relative to a fixed rotation axis (e.g., Phillips and Forsyth, 1972; Besse and Courtillot, 1991; 2002; Torsvik et al.,

2008; 2012). South Africa, or the African plate, is typically used as reference plate for the computation of a global APWP (Besse and Courtillot, 2002; Torsvik et al., 2008; 2012), because it is considered to have been relatively stationary (also longitudinally) for the last few 100 Ma, as it has been surrounded mostly by spreading ridges since the breakup of Pangea (e.g., Torsvik et al., 2008).

2.2 Shortcomings of conventional approaches, and alternatives

The conventional approach to calculating APWPs has several important limitations. First, known sources of uncertainty, such as uncertainties in the position or age of the input paleopoles, are typically not taken into account during the calculation of the APWP (Fig. 1b). In standard paleomagnetic procedures, directional uncertainties are quantified firstly at the level of individual paleomagnetic directions (often expressed as the maximum angular deviation; see e.g., Tauxe et al., 2010), secondly, at the level of individual site-mean directions (with an α_{95} confidence cone around the Fisher (1953) mean direction), and thirdly, at the level of paleomagnetic poles (with an A_{95} confidence cone around the Fisher (1953) mean of the input VGPs). However, these uncertainties are traditionally not propagated through this hierarchical framework (Heslop and Roberts, 2016; 2020). By computing an APWP from paleopoles without error propagation, it is implicitly assumed that the uncertainties and random biases in the individual paleomagnetic poles are effectively averaged 'out' by averaging up to a few dozen coeval paleopoles in the calculation of the reference poles of the APWP (e.g., Irving, 1964; Torsvik et al., 2008; 2014).

Vaes et al. (2022) showed that the assumption that paleopoles used to compute recent (global) APWPs average 'out' PSV is invalid. In fact, the dispersion of paleopoles around an APWP increases with a decreasing number of sites underpinning each paleopole. Despite the fact that the number of VGPs that underlie each input paleopole varies substantially (Vaes et al., 2022), each input paleopole is assigned equal weight in the classical running mean approach. Hence, the position and statistical properties of pole-based APWPs may be strongly affected by subjective choices in how data are distributed over poles. For example, site-level paleomagnetic data from multiple paleomagnetic studies of the same volcanic or sedimentary sequence may either be included in the computation of an APWP as a single paleopole (after combining the data on the site-level) or as separate entries. Hansma and Tohver (2020) explained that there is, in fact, no phenomenological basis for first averaging a certain number of VGPs to a 'study mean' pole to average PSV, and to then average the resulting poles again in the determination of an APWP.

It is important to note that there have been many previous efforts to propagate or weight uncertainties in the computation of apparent polar wander, for instance using a weighted running mean or spherical spline (e.g., Thompson and Clark, 1981; Harrison and Lindh, 1982; Torsvik et al., 1996; Schettino and Scotese, 2005; Swanson-Hysell et al., 2019; Wu et al., 2021; Gallo et al., 2021; Rose et al., 2022). However, the majority of the APWPs computed in these studies were still derived from paleopole-level data, and these weighting methods did not account for the subjectivity in the choice of the number of data underpinning each paleopole.

The approach chosen in this paper is aimed at overcoming these problems: we compute an APWP from site-level paleomagnetic data instead of from paleopoles (e.g., McElhinny and McFadden, 1974; Hansma and Tohver, 2020; Vaes et al., 2022). In this approach, equal weight is given to each VGP that is determined for a single 'site'. We here define a paleomagnetic 'site' as a geological unit that was formed in a short period of time relative to the time scale over which the geomagnetic field changes, such that the site mean direction represents a 'spot reading' of the paleomagnetic field (e.g., the site-mean direction from a lava flow, or a thin dyke) (see e.g., McElhinny and McFadden, 2000). Although it is often difficult to estimate the amount of geological time contained in a single sedimentary bed, individual samples obtained from sedimentary rocks may also provide independent readings of the past geomagnetic field (Tauxe and Kent, 2004; Bilardello and Kodama, 2010b). Demonstrating this may be challenging for small sediment-based datasets, but Vaes et al. (2021) recently formulated a stringent set of criteria to determine whether large paleomagnetic datasets (n>80 directions) derived from sediments represent collections of paleomagnetic spot readings. *Site-level data* referred to hereafter in this manuscript thus includes site-mean directions from lavas flows or thin dykes, as well as individual directions obtained from a single sedimentary horizon or bed. The use of site-level data rather than paleopoles better reflects the underlying paleomagnetic data by assigning larger weight to larger datasets of independent measurements of the past geomagnetic field and avoids the subjectivity surrounding the definition of a paleopole.

3. Methods

3.1 Calculating apparent polar wander from site-level data

We developed an approach to compute a global APWP for the last 320 Ma from site-level paleomagnetic data. To obtain a paleomagnetic dataset at the site-level, we use an iterative, parametric re-sampling approach (Fig. 2). Although it would be possible to calculate a global APWP directly from published site-level data, compiling these from the many hundreds of studies with relevant input data would require a major effort and is complicated by the fact that not all these studies have reported their data at the site-level. Recent analysis, however, showed that parametric re-sampling of VGPs from a set of reported paleopoles and their statistical parameters provides an accurate approximation of the original distribution of VGPs, albeit with a slightly larger dispersion (Vaes et al., 2022). To generate a site-level dataset, we first compiled a database of 'classical' paleomagnetic poles as reported in literature, with statistical properties that describe the number of underlying paleomagnetic sites and their dispersion, the sampling location, uncertainties associated with inclination shallowing correction, and age (see section 5). Using this database, we generate synthetic site-level paleomagnetic data from each paleopole included in our compilation and repeat this procedure 2000 times (Fig. 2). This large number of iterations ensures the robustness of the resulting APWP and allows the propagation of both spatial and temporal uncertainties in the confidence bounds of the APWP. For each iteration, we parametrically re-sample a set of *pseudo*-VGPs from a Fisher (1953) distribution that is centered around the paleopole and defined by its Fisher

(1953) precision parameter K. We generate the same number of VGPs as the number of sites that was included in the calculation of the paleopole (or grand mean paleomagnetic direction) reported in the original publication. In our approach, equal weight is thus assigned to each (*pseudo*-)VGP rather than to each paleopole, and the weight of each paleomagnetic dataset directly depends on its number of sites.

In our workflow, we also address the important source of uncertainty in the computation of APWPs that is known as 'inclination shallowing', which affects paleomagnetic datasets derived from sedimentary rocks. A 'blanket' correction factor (of f=0.6 in Torsvik et al., 2012) has often been used in the computation of APWPs (e.g., Torsvik et al., 2012; Wu et al., 2021; Kulakov et al., 2021) but this underestimates the natural variation in the magnitude of inclination shallowing and assumes that all sediments are affected by shallowing which is not always the case (e.g., Bilardello and Kodama, 2010a; Bilardello et al., 2011; Kodama, 2012; Gallo et al., 2017; Kent and Muttoni, 2020; Vaes et al., 2021; Pierce et al., 2022). In the computation of our global APWP, we only include datasets from sedimentary rocks to which an inclination shallowing correction has been applied and whereby the uncertainty in the correction is quantified. Except for two datasets that were corrected using an anisotropy-based correction technique (Kodama, 2009; Brandt et al., 2019), all sedimentary datasets were corrected for inclination shallowing using the elongation-inclination (E/I) method of Tauxe and Kent (2004).

To incorporate the uncertainty in the shallowing correction in our workflow, we build upon the recent work of Pierce et al. (2022). These authors developed a way to express the uncertainty of the E/I correction as an uncertainty in paleomagnetic pole position along the great-circle between the paleopole and the sampling locality, i.e., in the co-latitude direction. Using the ensemble of flattening factor obtained from the bootstrapped ensemble of paleomagnetic directions, they computed the ensemble of possible paleomagnetic pole positions, each with a different paleomagnetic paleo- and co-latitude. Pierce et al. (2022) noted that the distribution of estimated paleolatitudes approximates that of a normal distribution. Here, we assume that the distribution of paleolatitudes, and thus the co-latitudes, approximates a normal distribution, and use this to incorporate the extra uncertainty in the co-latitude direction resulting from inclination shallowing. To this end, we compute the standard deviation of the colatitude distribution for every inclination shallowing corrected dataset in our compilation. We obtain this value either by applying the E/I correction to the individual paleomagnetic directions that were published in the original paper or provided to us by the authors. If we were unable to obtain the directional dataset, we derived the standard deviation from the reported 95% confidence regions on the inclination or paleolatitude by taking these confidence regions as two standard deviations. For the two datasets corrected by an anisotropy-based approach, we use the reported confidence regions on the correction to obtain this value. For each iteration in our workflow, we first re-sample the paleomagnetic co-latitude from a normal distribution with a mean corresponding to the co-latitude of the shallowing-corrected pole and the listed standard deviation. We then compute a new position of the paleopole – along the great-circle between the sampling location and the reported shallowing-corrected paleopole – using this re-sampled co-

295 latitude and the paleomagnetic declination computed from the original shallowing-corrected pole.
296 This procedure yields a new position of each sediment-derived paleopole, thereby incorporating the
297 additional uncertainty in the co-latitude direction resulting from inclination shallowing. Next, pseudo-
298 VGPs are generated from this new paleopole position, following the workflow outlined above (Fig. 2a).
299 The second step in our workflow is to propagate the uncertainties in the age of the sampled
300 rocks. To this end, we randomly draw an age for each *pseudo*-VGP from a uniform distribution that
301 corresponds to the age uncertainty range listed for each paleopole in the database. Quantifying the
302 age uncertainty by a uniform distribution is intuitive for sediment-derived datasets, whose age
303 uncertainty range is often determined by bio- and/or magnetostratigraphy, and a uniform
304 distribution may straightforwardly be defined by the upper and lower age limit of the geological time
305 period or interpreted magnetozones. The age of igneous rocks, on the other hand, is often based on
306 radiometric dating, for which the uncertainty on individual age determinations is often reported as
307 one or two standard deviation(s), and a Gaussian distribution could thus be used to quantify the
308 uncertainty in age (see e.g., Swanson-Hysell et al., 2019; Wu et al., 2021, Gallo et al., 2021; Rose et al.,
309 2022). However, because the age of sampled igneous rocks is typically determined by multiple
310 radiometric ages, either from multiple dated samples or determined for the regional magmatic activity
311 (e.g., for a large igneous province (LIP)), it is difficult to use a Gaussian distribution for the age
312 uncertainty for all igneous datasets. We therefore choose a slightly more conservative approach and
313 also use a uniform distribution between the upper and lower limit reported for the age of the
314 paleomagnetic datasets that were derived from igneous rocks.
315 In the third step of our workflow, we transfer the obtained collection of *pseudo*-VGPs to the
316 same coordinate frame, for which we use an updated global model of relative plate motions (see
317 section 4 and Tables 1 and S1). For each tectonic plate included in the plate circuit, we computed the
318 Euler rotation poles per million years relative to a given reference plate, interpolating between
319 reported total reconstruction poles assuming constant rotation rates. Here, we use South Africa as our
320 main reference plate, as is commonly done in the construction of global APWPs (e.g., Besse and
321 Courtillot, 2002; Torsvik et al., 2008, 2012). We use this plate model to rotate each individual *pseudo*-
322 VGP to South Africa coordinates after rounding its assigned age to the nearest integer. This procedure
323 thus propagates the effect of uncertainties in age on the relative plate motion and position of the
324 tectonic plates from which the paleomagnetic data is derived.
325 In the fourth step, we determine a reference pole of the global APWP at a chosen interval (we
326 use an interval of 10 Ma) and with a chosen sliding window (here, 20 Ma). Because datasets cannot
327 constrain variations that are smaller than the uncertainties of that dataset, we only include data
328 collections in the analysis with an age uncertainty that is smaller than the chosen sliding window. The
329 reference pole is computed based on all *pseudo*-VGPs whose assigned age falls within the chosen age
330 window of the pole (Fig. 2b). In cases where the age uncertainty of a paleopole overlaps only partially
331 with the time window of a reference pole, only the *pseudo*-VGPs are used that were assigned an age
332 that falls in that time window. The contribution of each paleomagnetic dataset to a given reference

pole of the APWP is thus weighted against the overlap between the age range of the dataset and the time window of the reference pole. Because in each iteration, the *pseudo*-VGPs are redrawn and are assigned a new random age, the number of VGPs that falls within the chosen time window will differ between iterations. So, although the total number of *pseudo*-VGPs that are generated for the entire APWP is equal for each iteration, the exact number of VGPs that is used to compute each reference pole will vary due to the re-sampling of ages.

We compute each reference pole by taking the Fisher (1953) mean of the *pseudo*-VGPs that fall within the time window, yielding a reference *pseudo*-pole that provides an estimate of the time-averaged paleomagnetic pole position – and thus the rotation axis – in a South African coordinate frame. In addition, we compute a range of statistical parameters from the distribution of *pseudo*-VGPs, including the number of VGPs (N), the Fisher (1953) precision parameter (K), the 95% confidence region (A_{95}), the circular standard deviation (S) and the elongation parameter (E, computed as the ratio of eigenvalues τ_2/τ_3, see Tauxe et al., 2004). We use these statistical parameters to assess the robustness and identify potential biases in the distributions of re-sampled VGPs that underlie the reference poles.

Finally, we repeat the above procedure 2000 times to average the variation in the obtained reference poles resulting from parametric re-sampling and to allow the determination of confidence regions for the global APWP (see Fig. 2c). We compute the final reference poles of the APWP by taking the Fisher (1953) mean of the 2000 reference *pseudo*-poles for each time step. We define the confidence region of the reference poles of the global APWP by the circle that includes 95% of the 2000 reference *pseudo*-poles, which we refer to as the P95.

In this approach to calculating global apparent polar wander and its confidence, we thus incorporate a number of key uncertainties, including spatial and temporal uncertainties in the paleomagnetic datasets, the uncertainty associated with the E/I correction for inclination shallowing of sedimentary rocks, as well as uncertainties in the rotation of the VGPs to the reference coordinate system that results from uncertainties in age. All these uncertainties are reflected in the dispersion of the *pseudo*-VGPs, which is largely controlled by the between-pole dispersion of the coeval paleopoles and their K values that are used to parametrically re-sample the *pseudo*-VGPs. Other incidental errors in the dataset, such as incorrect age assignments, unrecognized regional vertical-axis rotations, or unrecognized magnetic overprints, cannot be explicitly taken into account or corrected for, but such errors would likely lead to increased dispersion in the pseudo-VGPs per time window. We will compare the average scatter, elongation, and Fisher (1953) precision parameter of the *pseudo*-VGPs with values expected from PSV to assess whether and which reference poles may suffer from such errors.

3.2 Selection criteria

We applied a number of selection criteria during the compilation of the paleomagnetic datasets that were used for construction of the global APWP (see section 5 for more details on the compilation).

First, we re-compiled the data that were included in the compilation of Torsvik et al. (2012) from the original publications. We excluded data for which evidence was reported that it does not represent a reliable estimate of the time-averaged field at the time of formation of the sampled rocks, as concluded by the original authors or by others in more recent work that evaluated that particular dataset. We also rejected datasets for which no modern demagnetization techniques were used, as is common procedure (van der Voo, 1990a; Meert et al., 2020). In addition, we removed duplicates: in some cases, the paleomagnetic data used to compute a paleopole that was included in the Torsvik et al. (2012) database were also used (and combined with other or newer data) to compute more recently published paleopoles. Reasons for exclusion are provided in Table S2 and include, for instance, evidence for remagnetization or unremoved magnetic overprints, local or regional vertical-axis rotations, erroneous structural corrections, or poor age control. We note that paleomagnetic datasets that were not originally compiled by Torsvik et al. (2012), e.g., because they were published after their compilation, and that did not satisfy the above criteria, were immediately rejected, and are not included in Table 2.

We then applied the following criteria to all paleomagnetic datasets:

1) We exclude datasets derived from less than 5 sites that are interpreted as independent spot readings of the past geomagnetic field. This number is essentially arbitrary but establishing whether such small datasets accurately represent PSV is difficult, and in our site-level computation of the APWP, the impact of such small datasets is negligible. We do not require that sites are based on averages of multiple samples, as this was shown to have minor effects on paleopole position or precision (Gerritsen et al., 2022).

2) We exclude paleomagnetic datasets from igneous rocks if their A_{95} values fall outside of the N-dependent reliability envelope of Deenen et al. (2011). This criterion evaluates whether the dispersion of VGPs is consistent with what may be expected from secular variation. If the reported A_{95} cone of confidence of the paleopole falls outside of the $A_{95,\,min\text{-}max}$ reliability envelope, this suggests that the dataset is likely affected by one or more sources of additional scatter that are unrelated to PSV (if $A_{95}>A_{95,\,max}$), or that PSV was insufficiently sampled by the dataset (if $A_{95}<A_{95,\,min}$), for instance, due to the limited temporal coverage of the sampled sites (see Deenen et al. (2011) for a detailed explanation).

3) We only include sediment-derived datasets whereby the paleopole and statistical parameters were calculated from a collection of paleomagnetic directions that approximately represent independent readings of the past geomagnetic field, and whereby these directions were corrected for potential inclination shallowing. To select such datasets, we use the reliability criteria formulated by Vaes et al. (2021), which assess under which conditions sedimentary datasets may be reliably corrected for inclination shallowing by the E/I correction, while satisfying the underlying assumption of that method that each of the paleomagnetic directions may be considered an independent reading of the past geomagnetic field. We only include E/I-corrected sedimentary datasets that would receive a grade 'A' or 'B' according to the evaluation scheme of Vaes et al. (2021). In addition, we have included

two datasets that satisfy these criteria but were corrected for inclination shallowing using an anisotropy-based approach (Kodama, 2009; Brandt et al., 2019). We note that these criteria for sedimentary rocks are far more stringent than in previous compilations for the computation of APWPs, and only 29 sediment-derived datasets are used in the computation of the global APWP.

4) As a final selection criterion, we only include datasets with an age uncertainty range of <20 Ma: datasets with larger age uncertainties can only be included in APWPs with sliding windows larger than 20 Ma, which we do not compute here, and which would lead to needless smoothing of the global APWP.

4. Global plate model

The global apparent polar wander path is computed from paleomagnetic data from all stable plate interiors after rotating them relative to a single tectonic plate using a global model of relative plate motions. These relative plate motions are quantitatively described by Euler rotation poles that are mostly derived from marine magnetic anomaly identifications and fracture zone data. In the global plate model, each tectonic plate is linked – either directly or via a chain of neighboring plates – to the reference plate South Africa. We only include the major plates and continental blocks whose motions relative to South Africa are well-established, such that the available paleomagnetic data may be reliably combined to construct a global APWP. A schematic representation of the global plate circuit is shown in Fig. 3.

In our global plate model, we incorporate recently published Euler rotation poles based on the highest-resolution marine geophysical records. The original sources of the rotation poles for each tectonic plate are listed in Table 1, and we provide all rotation poles in Table S1. We note that many of these rotation poles were already used for the construction of previous global APWPs (e.g., Kent and Irving, 2010; Torsvik et al., 2008, 2012), as well as in global plate models (Seton et al., 2012; Torsvik and Cocks, 2016; Müller et al., 2016, 2019). The latest updates have mostly added more detail to the plate motion histories (e.g., DeMets and Merkouriev, 2021), but do not significantly change the long-term motions. Importantly, we have converted the ages of all the interpreted magnetic anomalies to the most recent geological time scale of Gradstein et al. (2020), which may shift the age of anomalies by up to a few million years compared to the ages assigned by the original authors.

Our global APWP uses data from the following tectonic plates or lithospheric fragments (with plate identification number) whose relative motions are constrained for the entire time period from which data were compiled for our global APWP, i.e., the last 330 Ma (Fig. 3): North America (101), Greenland (102), South America/Amazonia (201), Parana (202), Colorado (290), Patagonia (291), Eurasia (301), India (501), Arabia (503), South Africa (701), Madagascar (702), Moroccan Meseta (707), Somalia (709), Northwest Africa (714), Northeast Africa (715), Australia (801), and East Antarctica (802).

In addition, we have added several tectonic plates and blocks to our plate circuit, which were not included in the previous data compilation of Torsvik et al. (2012). The motions of these plates relative to South Africa are not sufficiently well-constrained (e.g., by marine geophysical data) for the entire time period covered by our global APWP but are well-constrained for a more limited time period. We thus include them for the period for which their motions relative in the global plate model are determined independently from paleomagnetic data (Table 1).

We have included paleomagnetic data from Iberia (304) for times after chron 34n (~83.65 Ma, the end of the Cretaceous Normal Superchron; CNS). Although marine magnetic anomaly-based Euler rotations are available for Iberian motion before the superchron, we do not incorporate data from this time because the interpretation and robustness of the underlying anomalies are under debate (e.g., Bronner et al., 2011; Tucholke and Sibuet, 2012). We have included data from the North and South China Blocks (601, 602) for times younger than 130 Ma, corresponding to the youngest age estimates for the cessation of significant motion along the Mongol-Okhotsk suture zone (e.g., van der Voo et al., 2015; Yang et al., 2015). We have included paleomagnetic data from the Antarctic Peninsula and neighboring islands (803) for the last 140 Ma, for which time it was rigidly attached to East Antarctica (van de Lagemaat et al., 2021). We include the Caribbean plate (2007) back to 38 Ma, for which time there is no relative motion of the Cuba segment relative to North America and relative Caribbean-North America motions are constrained by marine magnetic anomalies on the oceanic crust that underlies the Cayman Trough (Leroy et al., 2000; Boschman et al., 2014). Finally, we have included the Pacific (901) and Nazca (911) Plates in our plate circuit (for which marine magnetic anomaly data are available for times after 83.65 and 22.34 Ma, respectively), allowing us to rotate the paleomagnetic data obtained from young volcanic rocks (<10 Ma) to South Africa. The Nazca Plate is reconstructed relative to the Pacific Plate using the Euler rotation poles from Tebbens and Cande (1997) that were updated by Wright et al. (2016). The Pacific Plate (901) is linked to the 'main' plate circuit of the major continent-hosting plates via a relative plate motion chain through Marie Byrd Land (using rotation poles of Croon et al., 2008; Wright et al., 2016) and East Antarctica (Cande and Stock, 2004; Granot et al., 2013; Granot and Dyment, 2018).

In contrast to Torsvik et al. (2012), we have excluded data from the Colorado Plateau from North America for times before 40 Ma. After 40 Ma, widespread extension affected the western USA forming the Basin and Range province, but a detailed kinematic restoration of this extension of McQuarrie and Wernicke (2005) showed that the rotation of the Colorado Plateau relative to North America in this time window was no more than ~1°, which we consider negligible. For times prior to 40 Ma, the Colorado Plateau moved relative to North America during shortening in the Laramide and Sevier fold-thrust belts (Yonkee and Weil, 2015, Arkula et al., 2023), and these motions have only been quantified based on paleomagnetically determined rotations, with an estimated rotation of the Colorado Plateau relative to North America ranging from ~5 to ~13° (e.g., Bryan and Gordon, 1990; Molina-Garza et al., 1998; Steiner, 2003; Kent and Witte, 1993). Including data from this block using a paleomagnetism-based rotation correction would thus introduce circular reasoning.

Adria has often been proposed to be part of stable Africa and is rich in paleomagnetic data, which has led several authors to use Adria-derived paleomagnetic data as input for APWP computation (e.g., Muttoni et al., 2013; Kent and Muttoni, 2020; Channell et al., 2022). However, there is unequivocal evidence for rotation in GPS measurements today, and Adria must have experienced both a Neogene rotation during the extension in the Sicily Channel, as well as a Triassic-Jurassic rotation during the opening of the oceanic eastern Mediterranean basin whose ocean floor is preserved in the Ionian Sea today (van Hinsbergen et al., 2020, and references therein). While these rotations of Adria relative to Africa may have been small (5-10° in the reconstruction of van Hinsbergen et al., 2020), the arguments for and against inclusion of Adria are based on the paleomagnetic data itself (Channell et al., 2022; van Hinsbergen et al., 2014), and using this data would thus introduce circular reasoning. Data for Adria are therefore not used in our compilation.

Finally, for times prior to ~270 Ma, there is an ongoing debate about whether Pangea may be considered a single continent (e.g., Domeier et al., 2012) or was cut by an enigmatic and unpreserved megashear (e.g., Muttoni and Kent, 2019). The latter model is based on paleomagnetic arguments, and its predicted relative plate motions can therefore not be used as an independent basis for computing a global APWP from paleomagnetic data from all major plates. For this reason, we compute a global APWP for the 330-270 Ma time period under the assumption of a Pangea A configuration (i.e., a single plate from ~320 Ma, following Torsvik et al., 2008; 2012), which is obtained by closing the oceanic basins between the major continents using marine geophysical constraints. In section 7, we evaluate whether the data from the northern and southern continents, or from the mobile belts that formed during Pangea formation as recently suggested by Pastor-Galán (2022), display systematic mismatches. Similar to the Pangea debate, Cogné et al. (2013) suggested that Asia and Europe moved in Cenozoic time over ~10° or more back and forth along enigmatic faults in the Ural and eastern Europe, to explain differences in paleomagnetic data from East Asia and the global APWP of Besse and Courtillot (2002). However, in absence of geological evidence for major Cenozoic cross-cutting fault zones, we treat Eurasia as a single plate in the Cenozoic.

5. Paleomagnetic database

We present here an updated database of paleomagnetic datasets for the tectonic plates and continental blocks described in the previous section (see Fig. 4, Table 2). Our compilation builds upon the efforts of the many paleomagnetists that collected, evaluated, and tabulated paleomagnetic results from hundreds of paleomagnetic studies of the last ~60 years, overviews of which have been published in a series of seminal papers (e.g., Irving, 1964, 1977; Irving and Irving, 1982; Van der Voo, 1990b; Lock and McElhinny, 1991; Torsvik et al., 2008; 2012). In this study, we used the data compilation presented in Torsvik et al. (2012) as a starting point. We have expanded this database by adding high-quality paleomagnetic results from undeformed or mildly folded regions that may be considered part of the stable plate interior, and that were published from 2012 to 2022, i.e., after the

database of Torsvik et al. (2012) was compiled, as well as newly compiled datasets from the additional regions. We have also included datasets that were published prior to 2012 that were not incorporated by Torsvik et al. (2012), but that were included in recent compilations of 'cratonic' paleopoles (e.g., Gallo et al., 2021; Kulakov et al., 2021; Gonzaléz et al., 2022). For transparency, we have included all paleomagnetic data that were published from stable plate interiors and that fit the basic criteria for inclusion (primary magnetization, modern demagnetization techniques, principal component analysis). When these data were subsequently excluded based on the Deenen et al. (2011) criteria (for igneous rocks), the Vaes et al. (2021) criteria (for sedimentary rocks) or for its large age uncertainty, this is indicated in the database (Table S2).

For the last 10 Ma, we have limited our data compilation to the paleomagnetic datasets that were included in the PSV10 database (Cromwell et al., 2018). This database consists of 83 paleomagnetic datasets that are obtained from volcanic rocks that formed in the last 10 Ma. Not all of these datasets were used for the calculation of the global APWP, however, as some do not satisfy the selection criteria described in section 3.2. We note that not all of these datasets are obtained from regions that would be considered as 'stable' plate interiors. Following Cromwell et al. (2018), we assume that regional deformation has not significantly influenced the paleomagnetic results from these young rocks (predominantly <3 Ma) and assign each dataset to the most appropriate tectonic plate that is included in the global plate circuit as described in section 4 (e.g., a PSV10 dataset from Alaska is considered to be derived from North America). The paleomagnetic data in the PSV10 database is compiled on the site-level and contains 2401 VGPs. Instead of using the published site-level data, we have calculated the paleomagnetic poles from each dataset and generate synthetic VGPs from those poles, to ensure consistency in our parametric re-sampling approach. We note that the application of this approach to the PSV10 database yields a distribution of (synthetic) VGPs that mimics that of the published VGPs, as recently shown by Vaes et al. (2022).

We have compiled metadata and statistical parameters for each paleomagnetic dataset (Table 2), based on the information provided in the original publications. For the application of our selection criteria, we have classified the lithology of the sampled rocks as either igneous or sedimentary. We have listed the paleopole (latitude, longitude) for each entry in our database in south pole coordinates. When available, we used the paleopole from the original publication (if provided) or computed the pole by taking the Fisher (1953) mean of the reported site-level VGPs. If the authors only provided the grand mean paleomagnetic direction, we used the mean sampling location to determine the position of the associated paleopole. We have listed the statistical parameters that underlie our sampling approach in Table 2, which include the number of sites, the Fisher (1953) precision parameter K and the A_{95} cone of confidence about the paleopole. These parameters were either obtained from the original publication or from other reported statistical parameters from which the missing values may be determined. If the number of sites and either the Fisher (1953) precision parameter K or the 95% cone of confidence (A_{95}) is provided, the other parameter was calculated if it was not reported (see e.g., Ch. 11 in Tauxe et al., 2010). For studies in which Fisher (1953) statistics have been applied to the

site-level paleomagnetic directions instead of the VGPs – yielding a mean paleomagnetic direction with an α95/k and an elliptical confidence region on the paleopole described by the parameters dp/dm (e.g., Butler, 1992) - we use the analytical formula of Cox (1970) to convert the *k* (and associated α95) to K (and A95), after estimating the paleolatitude using the reported mean paleomagnetic inclination (see Deenen et al., 2011 for more details).

For each paleomagnetic dataset, we have listed an age range that describes the uncertainty of the age determination of the sampled rocks, whereby we mostly follow the age assignment of the original authors. This may correspond to the uncertainty of an individual radiometric age, to the mean computed from multiple radiometric age determinations, or to a certain age interval from which the rocks are derived. For biostratigraphically or magnetostratigraphically dated sediments, we have updated the numerical ages using the most recent geological timescale, of Gradstein et al. (2020), which was also used for the plate model. When new age constraints were available, we have updated the ages of individual database entries, e.g., for data from LIPs. We emphasize here that not all age determinations are without controversy and that there are likely revised age determinations that we were not aware of during the compilation of our database. Finally, we note that additional details on the age determination, statistical parameters and the dominant lithology of the sampled rocks are provided in the extended database in Table S2.

6. Results

We computed a global APWP for the last 320 Ma using a 10 Ma time interval and a 20 Ma sliding window. The APWP is based on a total of 13737 parametrically re-sampled VGPs that are derived from 350 different paleomagnetic datasets (Table 2), yielding a mean and median number of sites per dataset of ~39 and 19, respectively. Of these datasets, 162 were included in the compilation of Torsvik et al. (2012), 71 in the PSV10 database (Cromwell et al., 2018) and 117 were added during our data compilation (most of which were published post-2011).

The new global APWP is shown in Fig. 5 as reference poles per 10 Ma that are plotted as south poles in South African coordinates (see also Table 3). The global APWP in the coordinate frame of other major tectonic plates, including North America, South America, Eurasia, India, Australia, Antarctica and the Pacific is given in Table 4. Because the *pseudo*-VGPs are not necessarily evenly distributed around the center age of the sliding window, we also report the average age of the re-sampled VGPs behind each reference pole in Table 3. In the following, we describe the geometry and statistical parameters of the global APWP as calculated for a South African coordinate frame (see also Figs. 5 and 6).

The reference poles of the global APWP in South African coordinates plot along smooth path segments intervened by sharp cusps (Fig. 5). The APWP shows a relatively smooth path from the present back to an Early Cretaceous (140 Ma) cusp that was also observed in previous global APWPs in South Africa coordinates (Besse and Courtillot, 2002; Schettino and Scotese, 2005; Torsvik et al.,

595 2008; 2012). The reference poles of the 140-230 Ma segment of the APWP form another relatively
596 smooth path, except for the 170 Ma pole which defines a minor 'kink' in the path. Notably, the
597 reference poles at 230 and 240 Ma (Early Triassic) show a large angular difference of ~10.4°. This is
598 in large contrast to the 250 and 260 Ma reference poles which are separated by only ~0.8° and define
599 another 'cusp' in our global APWP. The oldest (320-260 Ma) part of the APWP forms two segments
600 that are separated by a kink defined by the 290 Ma reference pole, although we note that the oldest
601 320-300 Ma segment has the largest uncertainties of our APWP.
602 The 95% confidence regions of the global APWP are defined by the circle that includes 95% of
603 the pseudo-poles computed for 2000 iterations (the P95). The size of the confidence regions ranges
604 from 0.7° to 3.5° (for the 0 and 170 Ma reference poles, respectively), with an average (and standard
605 deviation) of 1.6° (0.7°) (Table 3). The reference poles of the APWP are computed from, on average,
606 813 parametrically re-sampled VGPs. The lowest data density is observed for the Late Jurassic, with
607 only ~110-150 sites per time window. As expected, the highest data density is obtained for the last 10
608 Ma, provided by the large number of sites included in the PSV10 dataset. Additionally, the early
609 Cenozoic (50-60 Ma) and Late Triassic (200-220 Ma) segments of the APWP are also based on large
610 datasets of re-sampled VGPs.
611 For each time window, we computed the mean values of the Fisher (1953) precision parameter
612 (K), the circular standard deviation (CSD) and elongation (E) for each iteration from the distribution
613 of re-sampled VGPs that were included in that window (Table 3, Fig. 6b). The values for K are on
614 average 20.9, ranging between 12.4 and 34.7. We obtain an average angular standard deviation for all
615 time windows of 18.3°, with minimum and maximum values of 13.8° and 23.1°. The elongation ranges
616 from 1.07 to 1.42 (Table 3), with an average value of 1.16, indicating that the distribution of *pseudo*-
617 VGPs that fall within the same time window is approximately circularly symmetric (see also Fig. 2a).
618 We calculated the rate of apparent polar wander per 10 Ma time period from the great-circle
619 distance between reference poles of successive age (Fig. 6a). We obtain an average APW rate of 0.40
620 ± 0.21°/Ma (one standard deviation). Except for a notable spike in APW rate of 1.04°/Ma between 230
621 and 240 Ma and two peaks of ~0.8°/Ma at 100-110 Ma and 300-310 Ma, all APW rates are ~0.6°/Ma
622 or lower. There seems to be no clear correlation between the APW rate and age, and age bins with
623 relatively low APW rates alternate with slightly faster APW throughout the studied time span of the
624 pole path. On the other hand, the observed APW rates and position of the reference poles may be
625 influenced by an uneven temporal distribution of the re-sampled VGPs. For example, a large dataset
626 with relatively tight age constraints may 'pull' a reference pole toward the paleopole with large N. This
627 temporal bias may be identified from a relatively large difference between the center age of the
628 window and the mean age of the re-sampled VGPs that fall within that time window (see Fig. 6c). For
629 example, the high APW rate between 230 and 240 Ma may be explained by the difference in mean age
630 of the re-sampled VGPs of ~18 Ma. To correct for this effect, we have also computed the APW rates
631 per 10 Ma time interval by dividing the angular distance by the difference in mean age of the re-
632 sampled VGPs (Fig. 6a). Although the average APW rate (with one standard deviation) remains similar

633 (0.42 ± 0.18°/Ma), all the peaks in APW rate mentioned above disappear. Instead, we now observe a
634 single peak in the APW rate of 0.8-1.0°/Ma between 82 to ~95 Ma. Whether the observed spikes in
635 APW rate are robust features of our global APWP will be discussed in section 7.2.
636
637 # 7. Discussion
638 ## 7.1 Robustness of the global APWP
639 Our approach to compute a global APWP from site-level paleomagnetic data critically builds on the
640 assumption that the dominant sources of uncertainty in paleomagnetism are (more) effectively
641 averaged by assigning equal weight to each paleomagnetic site rather than to a paleopole that is an
642 average of an arbitrary collections of those sites (Vaes et al., 2022). On the one hand, our approach
643 allows us to straightforwardly propagate uncertainties in the age of the sampled rocks and the
644 uncertainty caused by paleosecular variation of the past magnetic field. On the other hand, there are
645 multiple sources of uncertainty and error that are independent of the number of sites, e.g., due to
646 unremoved magnetic overprints or remagnetization, dating errors, or non-rigidity of assumed rigid
647 plates. Besse and Courtillot (2002) suspected that because some degree of deformation is often
648 necessary for rocks to be exposed at the surface, unrecognized local deformation (such as local
649 rotations caused by plunging fold axes) may be an important source of noise in APWPs. In the
650 conventional approach in which each paleopole is assigned equal weight, the bias resulting from a
651 single dataset that is affected by one or more of the above artifacts is unlikely to be large. However, if
652 such a dataset has a large number of sites, its relatively large weight may cause considerable bias in
653 the APWP calculated from site-level data.
654 We first evaluate the influence of large datasets on the global APWP by parametrically re-
655 sampling only 50 VGPs for all paleomagnetic datasets that are based on more than 50 sites. The
656 resulting APWP is very similar to the one presented in the previous section (Fig. 7). As expected, the
657 confidence regions for many reference poles are larger, as they are based on fewer sites. We observe
658 two main differences. First, the 50 and 70 Ma poles are at a large angular distance from the 60 Ma
659 pole, as they are pulled less towards the larger datasets with ages of ~60 Ma. Second, the 240-300 Ma
660 segment of the APWP becomes a smoother path. This shows that although no major differences are
661 observed, large datasets indeed alter some segments of the APWP. However, since we do not know
662 the 'true' APWP, it is difficult to assess whether the influence of a large datasets represents a bias in
663 the path or provides improved constraints on the position of the 'true' time-average pole. The most
664 straightforward way of testing the robustness of these features of the global APWP is by collecting
665 more large high-quality datasets for these time intervals.
666 In addition, we assess the robustness of the new global APWP using a set of statistical
667 parameters that describe the distribution of the re-sampled VGPs per time window (see Table 4, Fig.
668 6b). The dispersion of *pseudo*-VGPs – as quantified by K or CSD – is shown to be similar to what may
669 be expected from 'normal' PSV. Typical values for K range from 10 to 70 (e.g., Deenen et al., 2011;

Meert et al., 2020) and for CSD (or VGP scatter, S) from 10 to 25 (e.g., Butler, 1992; Cromwell et al., 2018; Doubrovine et al., 2019). The mean K and CSD values obtained for each time window of the global APWP all fall within these ranges (Fig. 6b). In addition, the mean elongation of the *pseudo*-VGPs that fall within each age bin show that the re-sampled VGPs have a nearly circular symmetric distribution (Table 3), similar to what may be expected from PSV (e.g., Tauxe and Kent, 2004). Interestingly, the time intervals with the lowest dispersion of pseudo-VGPs approximately coincide with the Cretaceous Normal Superchron (~83-121 Ma, Gradstein et al., 2020) and Permo-Carboniferous Reversed Superchron (~267-318 Ma, Gradstein et al., 2020). Even though these dispersion values are not obtained from 'real' VGP-level data, we hypothesize that this may reflect a suppression in the magnitude of PSV during these intervals with stable magnetic field polarity, as was previously proposed (e.g., Brandt et al., 2019; Handford et al., 2021). We note, however, that the lowest dispersion of *pseudo*-VGPs is observed for the age windows centered at 130 and 140 Ma, whereby the majority of the input data is derived from large igneous datasets of South America and southern African that are associated with the Parana-Etendeka LIP. This low dispersion of *pseudo*-VGPs may be explained by the fact that the data is obtained from rocks of a relatively short age interval and is likely less affected by noise resulting from unrecognized local deformation or plate reconstruction errors.

In summary, the statistical parameters obtained for the global APWP indicate that the errors that undoubtedly exist in our dataset due to e.g., unresolved overprints, unrecognized tectonic deformation, plate circuit errors, or age errors, do not form a major contribution to the scatter of the data that drives the dispersion beyond values that typically represent PSV. This suggests that the global APWP presented here is robust and that it represents the time-averaged paleomagnetic field for each interval.

7.2 Comparison to previous global APWPs

Because of the fundamentally different approach used here, it is interesting to evaluate how the site-level-based path compares to previous global APWPs that were computed using the conventional running mean approach applied to paleopoles. We find that our new global APWP has a mean angular difference (with one standard deviation) of 2.5 ± 1.1° when compared to the global APWP of Torsvik et al. (2012) (Fig. 8a). This difference is similar to the mean angular difference of 2.6° between the global APWP (in South African coordinates) of Besse and Courtillot (2002) and Torsvik et al. (2012), but notably smaller than the difference between the APWP of Torsvik et al. (2012) and those of Torsvik et al. (2008) and Kent and Irving (2010), which yielded average angular differences of 3.9° and 4.1°, respectively. These APWPs were all computed using the same running mean approach with a time step of 10 Ma and a sliding window of 20 Ma, and the observed differences thus resulted from differences between the compilations of paleopoles and plate reconstruction parameters. But even though we constructed our path using (i) parametrically re-sampled VGPs instead of paleopoles, (ii) an updated paleomagnetic database obtained with more stringent selection criteria and (iii) an updated global plate circuit, we obtain a path that is, to first-order, similar to the most recent pole-

708 based APWP of Torsvik et al. (2012) (see Fig. 5a). This clearly shows that the overall geometry of the
709 path is well-constrained, and strengthens confidence that paleomagnetism provides a reliable and
710 reproducible reference frame as basis for paleogeography and paleoclimate for the last 320 Ma.
711 One of the main differences between our VGP-based APWP and the pole-based APWP of Torsvik
712 et al. (2012) is the size of the 95% confidence regions (Fig. 5a). Particularly for time intervals with
713 high data density, such as for the Cenozoic, Early Cretaceous and Late Triassic, the confidence regions
714 of the new global APWP are <1.5°, compared to A_{95} values of ~2-3° of the Torsvik et al. (2012) path
715 for those intervals. The smaller confidence regions may seem counterintuitive, since the approach
716 used for the VGP-based path incorporates both temporal and spatial uncertainties that were set to
717 zero in the computation of the APWP of Torsvik et al. (2012). We interpret this as simply the result of
718 the significant increase in data points from dozens of paleopoles to hundreds or even thousands of re-
719 sampled *pseudo*-VGPs. The increase in independent data points thus outweighs the larger dispersion
720 of simulated VGPs (with a K of ~15-35) compared to that of coeval paleopoles (with K values of ~100,
721 see Rowley, 2019; Vaes et al., 2022). The smaller confidence regions obtained from using site-level
722 data instead of paleopoles was previously observed for the PSV10 dataset by Vaes et al. (2022). This
723 suggests that the resolution and precision obtained with paleomagnetic data has long been
724 underestimated by artificially decreasing the number of data points underlying APWPs due to the
725 averaging of arbitrarily defined collections of sites into paleopoles.
726 Although the first-order geometry of our new global APWP is similar to that of Torsvik et al.
727 (2012), there are several time intervals for which there are notable differences. For instance, the
728 reference poles of the 30-40, 90-100 and 310-320 Ma segments of the path, as well as the poles at 200
729 and 230 Ma, are at an angular distance of >3° (Fig. 8a). We interpret these differences as being mainly
730 caused by our site-level approach and the updated paleomagnetic database, to which we added
731 recently published data but from which we also excluded many paleomagnetic datasets due to the
732 application of our more stringent selection criteria.
733 The largest difference between our new global APWP and that of Torsvik et al. (2012) is
734 observed for the 140-170 Ma segment, yielding an angular difference of ~4° (Fig. 5, 8a). This segment
735 of the APWP of Torsvik et al. (2012) was based on relatively few paleopoles (<20 per time window),
736 and the observed differences may partly be explained by the inclusion of recently published datasets
737 in our database, e.g., those from Cervantes-Solano et al. (2020) and Kulakov et al. (2021). Despite these
738 differences, our new APWP is similar to that of Torsvik et al. (2012) in that it does not include a phase
739 of rapid polar wander between ~165 and 140 Ma as shown in the APWP of Kent and Irving (2010).
740 This rapid polar shift is often referred to as the 'Jurassic monster polar shift' and has been interpreted
741 as fast true polar wander (e.g., Kent et al., 2015; Muttoni and Kent, 2019; Yi et al., 2019). Our new
742 global APWP does not support such anomalously fast polar wander in the Late Jurassic, consistent
743 with recently published paleomagnetic results (Kulakov et al., 2021; Gao et al., 2021). We note,
744 however, that our APWP does not rule out the occurrence of a phase of relatively 'slow' TPW in the
745 late Jurassic.

Another notable difference is the ~4° angular distance between our reference pole at 100 Ma and that of Torsvik et al. (2012), yielding a very different estimate of the APW rate at mid-Cretaceous times. The 110-100 Ma spike in APW rate observed by Torsvik et al. (2012) is much less pronounced in our global APWP and disappears entirely when correcting for the 'effective' age difference between successive reference poles (Fig. 8b). We find that the re-sampled VGPs that fall in the age windows centered on 100 Ma and 110 Ma have mean ages of ~95 Ma and ~115 Ma, respectively (Fig. 6c, Table 3), indicating that the spike in uncorrected APW rate may be the result from an uneven age distribution of the input data. This suggests that previous estimates of APW rate based on the center ages of each time window may be influenced by temporal biases and shows the importance of taken into account the uncertainties in ages and their distribution.

Intriguingly, after applying a correction for the effective age difference between successive reference poles, the APW rates calculated for South Africa for the last 320 Ma show only a single spike at ~82-95 Ma. Although a detailed analysis of this phase of rapid APW is beyond the scope of this paper, we note that this spike coincides with a ~80-92 Ma peak in the convergence rate during a counterclockwise rotation of Africa relative to Eurasia, as part of a recently proposed tectonic chain reaction (Gürer et al., 2022). The spike in APW rate observed in our APWP may thus be related to a phase of relatively rapid plate motion of (South) Africa.

Finally, we note that there are a number of previously inferred and long-debated 'anomalies' in paleomagnetic data, such as those between the major continents of Gondwana, Laurentia, and Baltica for ~320-250 Ma which underpin the Pangea A vs B controversy (e.g., Domeier et al., 2012; 2021; Gallo et al., 2017; Kent and Muttoni, 2020, Kent et al., 2021; Pastor-Galan, 2022), or the 'east Asian inclination anomaly' in the Paleogene (e.g., Cogné et al., 2013). The observed mismatches between paleomagnetic data and APWPs of different continents and tectonic plates have generally been based on analyses using pole-level data. These discrepancies may be re-evaluated using a site-level approach, in which spatial and temporal uncertainties are explicitly incorporated, which have often been omitted in comparative analyses. Evaluating whether previously inferred anomalies still exist when using our site-level approach requires a detailed review of the underlying data, which is beyond the scope of this paper. We note, however, that there is no systematic increase in the dispersion of re-sampled VGPs that underlie our site-based global APWP in the time intervals of the long-standing debates. We thus find no reason to infer a significant error in the relative plate motion model in these time intervals (e.g., Muttoni et al., 2003, Cogné et al., 2013), or a systematic time-dependent non-dipole field (e.g., Torsvik and van der Voo, 2002, Dupont-Nivet et al., 2010).

7.3 Resolution of the global APWP

We calculated the reference poles of the global APWP at a resolution of 10 Ma using a sliding window of 20 Ma, similar to previously published global APWPs of Besse and Courtillot (2002), Kent and Irving (2010) and Torsvik et al. (2008; 2012). The use of such overlapping time windows results in the smoothing of the pole path and is expected to increase the extent to which random biases and noise

in the underlying data are averaged. On the other hand, too much smoothing could cause the removal of short-duration features in the APWP that may be real (e.g., Muttoni et al., 2005; Dupont-Nivet et al., 2010), as illustrated, for instance, by the spherical spline path of Torsvik et al. (2008) that smoothed 'away' a peak in APW rate. To assess the influence of the temporal resolution on the shape of the global APWP, we also computed the path at a higher resolution, using a time step of 5 Ma and a sliding window of 10 Ma (Fig. 9). The geometry of the path is notably more irregular than the APWP calculated using a 20 Ma sliding window, showing more distinct features such as relative standstills and cusps that separate segments of the path covering shorter time intervals. For example, while the 10 Ma-resolution-APWP showed a relative smooth path for the last 140 Ma, the 5 Ma-resolution-APWP shows a relative stand-still during the 30-50 Ma interval (Fig. 9a). For time intervals with relatively high APW rates, such as from 180 to 230 Ma, the 5 Ma-resolution-path is nearly identical to the 10 Ma-resolution-path. This finding is consistent with that of Besse and Courtillot (2002) who also computed their global APWP at a 5 Ma resolution (with a 10 Ma window) and who illustrated the large similarities between both paths in the coordinate frame of the relatively fast-moving Indian plate, noting that all the 'essential' features were captured by both paths. The use of a smaller time window leads to a decrease in the degree of smoothing of the path, resulting in ~40% higher APW rates with an average of 0.58 ± 0.30°/Ma (after correcting for the effective age) and seven intervals of 5 Ma that yield an APW rate of >1.0°/Ma (Fig. 9b). Notably, the peak in APW rate observed for the 10 Ma-resolution-APWP between 82 and ~95 Ma is also identified for the 5-Ma-resolution-APWP, which shows a ~1.2°/Ma APW rate between 86 and ~94 Ma.

The reference poles of the 5 Ma-resolution-APWP are, unsurprisingly, based on about half as many re-sampled VGPs (417 versus 813) compared to the 10 Ma-resolution-APWP. Notably, ~17% of the reference poles have a mean number of sites of <100 (see Fig. 9c, Table S3). The reduced number of sites behind each reference pole leads to larger confidence regions that have an average (and standard deviation) of 2.5° (1.2°) compared to 1.6° (0.7°) for the 10 Ma-resolution-APWP (Fig. 9a). Intriguingly, the distribution of re-sampled VGPs shows a very similar mean dispersion, with a K value of 22.2 for the 5 Ma-resolution-APWP compared to 20.9 for the 10 Ma-resolution-APWP, further supporting that the distributions of re-sampled VGPs underpinning our global APWP provide a robust approximation of the dispersion expected from PSV (Fig. 9c). But because of the lower number of re-sampled VGPs per time window, the APWP and associated APW rates are more likely to be biased by random noise or an uneven temporal distribution of the re-sampled VGPs.

7.4 Outlook

The calculation of a global APWP based on parametrically re-sampled VGPs provides a next step in the propagation of key sources of uncertainty in the computation of APWPs, building on previous efforts and approaches aimed to incorporate uncertainties in paleopoles or APWPs (e.g., McFadden and McElhinny, 1995; Swanson-Hysell et al., 2019; Hansma and Tohver, 2020; Gallo et al., 2021; Vaes et al., 2022; Pierce et al., 2022). Future improvements in the propagation of errors may concentrate on

some of the following aspects. First, errors in the Euler rotation poles that are used to rotate the VGPs to a common coordinate frame are not yet propagated. Although methods have been developed to propagate such uncertainties throughout a plate circuit (Doubrovine and Tarduno, 2008), the uncertainties of many Euler rotation poles computed from ocean floor anomalies have not been reported and the size of error ellipses of marine magnetic anomaly-derived are typically an order of magnitude smaller than uncertainties induced by PSV (e.g., DeMets and Merkouriev, 2021). We foresee that the propagation of these errors will provide only marginal gains.

Second, a statistical framework for the full propagation of the errors through the hierarchical levels of paleomagnetic data, that is from the individual demagnetization steps to the VGP or paleopole - has yet to be developed. Recent advances in the statistical treatments of paleomagnetic data (Heslop and Roberts, 2016; 2020) or directional statistics (e.g., Scealy et al., 2022) may provide promising avenues for improved propagation of these fundamental uncertainties behind paleomagnetic data. Ideally, future APWPs could be computed from 'real' site-level data rather than from parametrically re-sampled VGPs. Such an approach would avoid the necessity of adopting a pre-defined distribution of VGPs, such as the assumed Fisher (1953) distribution used here. When using a parametric re-sampling approach, the Fisher (1953) distribution is essentially the only option, however, for the simple reason that statistical parameters describing the paleomagnetic data distributions have traditionally been reported in the framework of Fisher (1953). Building the database from the 'real' VGPs would also allow the systematic application of selection criteria and data filters on the site-level. Apart from the fact that not all site-level data is available for the studies included in the data compilations that underlie global APWPs, the compilation of more than ten thousand sites from hundreds of publications would require an enormous effort. Whether the calculation of an APWP from the published VGPs would yield different results from our re-sampling approach remains to be investigated. To enable the computation of VGP-based APWPs in the future, we strongly recommend paleomagnetists to archive their published data, e.g., in the MagIC database (Jarboe et al., 2012) or the Paleomagnetism.org data library (Koymans et al., 2020).

We emphasize that the calculation of a reference APWP from site-level data provides opportunities to significantly improve intervals of the global APWP by collecting large datasets of independent readings of the past geomagnetic field (e.g., from thick sequences of lava flows or sedimentary rocks), particularly for time intervals that have a relative low data coverage. Moreover, Dupont-Nivet et al. (2010) already argued that the precision and temporal resolution of reference APWPs provides a limiting factor in the analysis of detailed tectonic problems, such as the estimation of convergence rates between tectonic terranes that are not included in a plate circuit. They therefore tried to stimulate the paleomagnetic community to focus part of their efforts on collecting datasets from stable plate interiors that may improve the accuracy and precision of the global APWP. We suggest here that rock formations that have provided reliable paleomagnetic data in the past but that include, as of yet, only a relatively limited number of sites may provide particularly useful sampling locations for this purpose. In addition, we highlight that our new approach allows the comparison of

independent paleomagnetic datasets against the global APWP at the site-level, which may improve the robustness of future determinations of relative tectonic displacements such as paleolatitudinal motions and vertical-axis rotations (see Vaes et al., 2022). Finally, we note the site-level approach holds great promise to optimize the resolution of APWPs for key time intervals, such as those containing mass extinctions or climate crises: collecting data from such well-dated intervals allows computing a high-resolution paleomagnetic reference frame that may be used as input for detailed studies of such events. We foresee that the continuous improvement of the global APWP, both in terms of data coverage and uncertainty incorporation, will enable Earth Scientists to place better quantitative constraints on, for instance, orogenic evolution, the rate and magnitude of TPW, plate tectonic reconstructions and the paleogeographical influence on paleoclimate, paleoenvironment and paleobiology.

8. Conclusions

In this study, we presented a global apparent polar wander path for the last 320 Ma calculated from simulated site-level paleomagnetic data, using an updated paleomagnetic database and relative plate motion model. Based on our new APWP, we conclude the following:

- A parametric re-sampling approach allows the straightforward incorporation of both spatial and temporal uncertainties in the paleomagnetic data, as well as uncertainty in the widely used E/I correction for inclination shallowing. Even though these uncertainties are taken into account in our approach, the 95% confidence regions of the site-level APWP are smaller than that of previously computed global APWPs because the much larger number of re-sampled VGPs per time window compared to the number of paleopoles in the conventional approach outweighs the larger dispersion of synthetic VGPs compared to paleopoles.
- The distributions of parametrically re-sampled VGPs that fall within a given age bin resemble the dispersion of VGPs expected for normal geomagnetic field behavior (that is, PSV) in the last few hundred Ma. This indicates that there are no major sources of noise that significantly enhance the dispersion beyond expected values for PSV and that would bias the global APWP.
- The first-order geometry of the new global APWP is similar to the most recent pole-based APWP of Torsvik et al. (2012), with an average angular difference of 2.8° between similar-aged reference poles. The average APW rate for South Africa is 0.38° ± 0.23° (1σ), slightly lower than the 0.43° $\pm$ 0.22° obtained by Torsvik et al. (2012). The similarity between the previous pole-based global APWP and our APWP computed from site-level data, using more stringent selection criteria, an updated database and global plate model, indicates that the global APWP is robust and reproducible.
- Peaks in APW rate may result from a temporal bias in paleomagnetic data. By correcting for the mean age of the re-sampled VGPs that underlie each reference pole, we observe that previously

identified spikes in APW rate (for South Africa) disappear, while a new peak in APW rate is identified between 100-80 Ma.

- The calculation of the global APWP at a higher resolution using a time step of 5 Ma and a sliding window of 10 Ma results in a more irregular path with time intervals that show standstills that alternate with segments with relatively high APW rates. We find that the data coverage is certainly high enough to compute a reliable path at this resolution for some time intervals, but not for the entire 320-0 time period.
- Calculating APWPs from site-level data provides opportunities to significantly improve the temporal resolution and robustness of the global APWP by collecting large high-quality paleomagnetic datasets from stable plate interiors, particularly from rocks derived from age intervals and/or tectonic plates that are underrepresented in the current database. Finally, we emphasize that such datasets may also contribute to future re-assessments of previously observed systematic differences between similarly aged paleomagnetic data from different tectonic plates (e.g., the Pangea controversy), or provide a better-constrained paleomagnetic reference frame for time intervals of rapid Earth system change, such as climate crises and mass extinctions.

Acknowledgements

BV, DJJvH, SHAvdL, EvdW, NL, and AQ acknowledge NWO Vici grant 865.17.001 to DJJvH. LCG has received funding from the European Union's Horizon 2020 research and innovation program under the Marie Skłodowska-Curie grant agreement No. 101025975. LMB acknowledges NWO Veni grant 212.247. We thank Hayfaa Abdul Aziz, Hemmo Abels, Mohamed Amenna, Daniele Brandt, Luca Foresi, Miguel Garcés, Peter Giles, Andrey Guzhikov, Mark Hounslow, Paula Iglesia-Llanos, Dennis Kent, Maud Meijers, Florencia Milanese, Vladimir Pavlov, and Vicente Carlos Ruiz-Martinez for providing the sample-level paleomagnetic directions that we needed for the application of the E/I correction for inclination shallowing.

Data Availability

No new paleomagnetic and marine magnetic anomaly data is used in this study. The paleomagnetic data compilation includes datasets from previously published peer-reviewed articles and builds on compilations by Torsvik et al. (2012) and Cromwell et al. (2018). The complete database can be found in Table S2. The global plate circuit presented in this study consists of previously published Euler rotation poles that are provided in Table S1. The Python codes used for the computation of the global APWP, its statistical parameters and the associated figures will be made publicly available on Github and archived on Zenodo upon acceptance of this manuscript.

References

Abdul Aziz, H., van Dam, J., Hilgen, F. J., & Krijgsman, W. (2004). Astronomical forcing in Upper Miocene continental sequences: implications for the Geomagnetic Polarity Time Scale. *Earth and Planetary Science Letters, 222*(1), 243-258. doi:10.1016/j.epsl.2004.02.018

Abels, H. A., Aziz, H. A., Ventra, D., & Hilgen, F. J. (2009). Orbital Climate Forcing in Mudflat to Marginal Lacustrine Deposits in the Miocene Teruel Basin (Northeast Spain). *Journal of Sedimentary Research, 79*(11), 831-847. doi:10.2110/jsr.2009.081

Abels, H. A., Hilgen, F. J., Krijgsman, W., Kruk, R. W., Raffi, I., Turco, E., & Zachariasse, W. J. (2005). Long-period orbital control on middle Miocene global cooling: Integrated stratigraphy and astronomical tuning of the Blue Clay Formation on Malta. *Paleoceanography*, *20*(4).

Ahn, H.-S., Kidane, T., Otofuji, Y.-i., Yamamoto, Y., Ishikawa, N., and Yoshimura, Y. (2021). High-resolution palaeomagnetic results of Ethiopian trap series from Lima Limo section: implications for the Oligocene geomagnetic field behaviour and timing of volcanism. *Geophysical Journal International, 225*(1), 311-328.

Alvey, A. D. (2009). *Using crustal thickness and continental lithosphere thinning factors form gravity inversion to refine plate reconstruction models for the Arctic & North Atlantic* (Doctoral dissertation, University of Liverpool).

Arkula, C., Lom, N., Wakabayashi, J., Rea-Downing, G., Qayyum, A., Dekkers, M. J., ... and van Hinsbergen, D. J. (2023). The forearc ophiolites of California formed during trench-parallel spreading: Kinematic reconstruction of the western USA Cordillera since the Jurassic. *Earth-Science Reviews*, *237*, 104275.

Audin, L., Quidelleur, X., Coulié, E., Courtillot, V., Gilder, S., Manighetti, I., . . . Kidane, T. (2004). Palaeomagnetism and K-Ar and40Ar/39Ar ages in the Ali Sabieh area (Republic of Djibouti and Ethiopia): constraints on the mechanism of Aden ridge propagation into southeastern Afar during the last 10 Myr. *Geophysical Journal International, 158*(1), 327-345. doi:10.1111/j.1365-246X.2004.02286.x

Besse, J., and Courtillot, V. (1991). Revised and synthetic apparent polar wander paths of the African, Eurasian, North American and Indian plates, and true polar wander since 200 Ma. *Journal of Geophysical Research: Solid Earth*, *96*(B3), 4029-4050.

Besse, J., and Courtillot, V. (2002). Apparent and true polar wander and the geometry of the geomagnetic field over the last 200 Myr. *Journal of Geophysical Research: Solid Earth*, 107(B11), EPM-6.

Biggin, A. J., Bono, R. K., Meduri, D. G., Sprain, C. J., Davies, C. J., Holme, R., and Doubrovine, P. V. (2020). Quantitative estimates of average geomagnetic axial dipole dominance in deep geological time. *Nature communications*, *11*(1), 1-9.

Bilardello, D., and Kodama, K. P., (2010a). Palaeomagnetism and magnetic anisotropy of Carboniferous red beds from the Maritime Provinces of Canada: evidence for shallow palaeomagnetic inclinations

and implications for North American apparent polar wander. *Geophysical Journal International*, 180(3), 1013-1029.

Bilardello, D., and Kodama, K. P., (2010b). Rock magnetic evidence for inclination shallowing in the early Carboniferous Deer Lake Group red beds of western Newfoundland. *Geophysical Journal International*, 181(1), 275-289.

Bilardello, D., Jezek, J., and Kodama, K. P., (2011). Propagating and incorporating the error in anisotropy-based inclination corrections. *Geophysical Journal International*, 187(1), 75-84.

Bono, R. K., Biggin, A. J., Holme, R., Davies, C. J., Meduri, D. G., and Bestard, J. (2020). Covariant giant Gaussian process models with improved reproduction of palaeosecular variation. *Geochemistry, Geophysics, Geosystems*, *21*(8), e2020GC008960.

Boschman, L.M., van Hinsbergen, D.J.J., Torsvik, T.H., Spakman, W. and Pindell, J.L., (2014). Kinematic reconstruction of the Caribbean region since the Early Jurassic. *Earth-Science Reviews*, 138: 102-136.

Brandt, D., Constable, C., & Ernesto, M. (2020). Giant Gaussian process models of geomagnetic palaeosecular variation: a directional outlook. *Geophysical Journal International, 222*(3), 1526-1541.

Brandt, D., Ernesto, M., Constable, C., Franco, D. R., Carlos Weinschutz, L., de Oliveira Carvalho Rodrigues, P., ... and Zhao, X. (2019). New late Pennsylvanian paleomagnetic results from Paraná Basin (Southern Brazil): is the recent giant Gaussian process model valid for the Kiaman superchron?. *Journal of Geophysical Research: Solid Earth*, *124*(7), 6223-6242.

Bronner, A., Sauter, D., Manatschal, G., Péron-Pinvidic, G. and Munschy, M., (2011). Magmatic breakup as an explanation for magnetic anomalies at magma-poor rifted margins. *Nature Geoscience*, 4(8): 549-553.

Brown, L. L., & Golombek, M. P. (1997). Tectonic stability of the San Luis Hills, Northern Rio Grande Rift, Colorado: Evidence from paleomagnetic measurements. *Geophysical Research Letters, 24*(4), 473-476. doi:10.1029/97gl00127

Brown, L. L., Singer, B. S., & Gorring, M. L. (2004). Paleomagnetism and40Ar/39Ar Chronology of Lavas from Meseta del Lago Buenos Aires, Patagonia. *Geochemistry, Geophysics, Geosystems, 5*(1), n/a-n/a. doi:10.1029/2003gc000526

Bryan, P., & Gordon, R. G. (1990). Rotation of the Colorado Plateau: An updated analysis of paleomagnetic poles. *Geophysical Research Letters, 17*(10), 1501-1504.

Bull, J. M., DeMets, C., Krishna, K. S., Sanderson, D. J., & Merkouriev, S. (2010). Reconciling plate kinematic and seismic estimates of lithospheric convergence in the central Indian Ocean. *Geology*, *38*(4), 307-310.

Butler, R. F. (1992). *Paleomagnetism: magnetic domains to geologic terranes* (Vol. 319). Boston: Blackwell Scientific Publications.

1006 Butler, R. F., Hervé, F., Munizaga, F., Beck, M. E., Burmester, R. F., & Oviedo, E. S. (1991).
1007 Paleomagnetism of the Patagonian Plateau Basalts, southern Chile and Argentina. *Journal of*
1008 *Geophysical Research: Solid Earth, 96*(B4), 6023-6034. doi:10.1029/90jb02698
1009 Camps, P., Henry, B., Nicolaysen, K., & Plenier, G. (2007). Statistical properties of paleomagnetic
1010 directions in Kerguelen lava flows: Implications for the late Oligocene paleomagnetic field. *Journal*
1011 *of Geophysical Research, 112*(B6). doi:10.1029/2006jb004648
1012 Cande, S. C., & Patriat, P. (2015). The anticorrelated velocities of Africa and India in the Late Cretaceous
1013 and early Cenozoic. *Geophysical Journal International*, *200*(1), 227-243.
1014 Cande, S. C., & Stock, J. M. (2004). Pacific—Antarctic—Australia motion and the formation of the
1015 Macquarie Plate. *Geophysical Journal International, 157*(1), 399-414.
1016 Cervantes Solano, M., Goguitchaichvili, A., Mena, M., Alva-Valdivia, L., Morales Contreras, J., Cejudo
1017 Ruiz, R., ... & Urrutia-Fucugauchi, J. (2015). Paleomagnetic pole positions and geomagnetic secular
1018 variation from the Cretaceous Ponta Grossa Dike Swarm (Brazil). *Geofísica internacional*, *54*(2),
1019 167-178.
1020 Cervantes-Solano, M., Goguitchaichvili, A., Bettucci, L. S., Morales-Contreras, J., Gogorza, C., & Núñez, P.
1021 (2020). An integrated paleomagnetic and multispecimen paleointensity study from the late
1022 Jurassic Zapicán dike swarm (Uruguay). *Journal of South American Earth Sciences*, *104*, 102815.
1023 Channell, J. E. T., Muttoni, G., and Kent, D. V. (2022). Adria in Mediterranean paleogeography, the origin
1024 of the Ionian Sea, and Permo-Triassic configurations of Pangea. *Earth-Science Reviews*, *230*,
1025 104045.
1026 Chenet, A.-L., Courtillot, V., Fluteau, F., Gérard, M., Quidelleur, X., Khadri, S. F. R., et al. (2009).
1027 Determination of rapid Deccan eruptions across the Cretaceous-Tertiary boundary using
1028 paleomagnetic secular variation: 2. Constraints from analysis of eight new sections and synthesis
1029 for a 3500-m-thick composite section. *Journal of Geophysical Research, 114*(B6).
1030 Clark, D. A., & Lackie, M. A. (2003). Palaeomagnetism of the Early Permian Mount Leyshon intrusive
1031 complex and tuckers igneous complex, North Queensland, Australia. *Geophysical Journal*
1032 *International*, *153*(3), 523-547.
1033 Clyde, W. C., Hamzi, W., Finarelli, J. A., Wing, S. L., Schankler, D., & Chew, A. (2007). Basin-wide
1034 magnetostratigraphic framework for the Bighorn Basin, Wyoming. *Geological Society of America*
1035 *Bulletin, 119*(7-8), 848-859. doi:10.1130/b26104.1
1036 Clyde, W. C., Krause, J. M., De Benedetti, F., Ramezani, J., Cúneo, N. R., Gandolfo, M. A., et al. (2021). New
1037 South American record of the Cretaceous–Paleogene boundary interval (La Colonia Formation,
1038 Patagonia, Argentina). *Cretaceous Research, 126*.
1039 Cogné, J. P., Besse, J., Chen, Y., and Hankard, F. (2013). A new Late Cretaceous to Present APWP for Asia
1040 and its implications for paleomagnetic shallow inclinations in Central Asia and Cenozoic Eurasian
1041 plate deformation. *Geophysical Journal International*, *192*(3), 1000-1024.

1042 Cojan, I., & Moreau, M. G. (2006). Correlation of Terrestrial Climatic Fluctuations with Global Signals
1043 During the Upper Cretaceous-Danian in a Compressive Setting (Provence, France). *Journal of*
1044 *Sedimentary Research, 76*(3), 589-604. doi:10.2110/jsr.2006.045
1045 Cox, A. (1970). Latitude dependence of the angular dispersion of the geomagnetic field. *Geophysical*
1046 *Journal International*, *20*(3), 253-269.
1047 Creer, K. M., Irving, E., and Runcorn, S. K. (1954). The direction of the geomagnetic field in remote
1048 epochs in Great Britain. *Journal of Geomagnetism and Geoelectricity*, *6*(4), 163-168.
1049 Cromwell, G., Johnson, C. L., Tauxe, L., Constable, C. G., & Jarboe, N. A. (2018). PSV10: A global data set
1050 for 0–10 Ma time-averaged field and paleosecular variation studies. *Geochemistry, Geophysics,*
1051 *Geosystems*, *19*(5), 1533-1558.
1052 Croon, M. B., Cande, S. C., & Stock, J. M. (2008). Revised Pacific-Antarctic plate motions and geophysics
1053 of the Menard Fracture Zone. *Geochemistry, Geophysics, Geosystems, 9*(7).
1054 Das, A., Mallik, J., & Shajahan, R. (2021). Geodynamics related to late-stage Deccan volcanism: Insights
1055 from paleomagnetic studies on Dhule-Nandurbar (DND) dyke swarm. *J. Ind. Geophys. Union*, *25*(6),
1056 28-44.
1057 De Kock, M. O., and Abubakre, A. O. (2022). Permian Magnetostratigraphy and End of the Kiaman
1058 Reverse Polarity Superchron From the Southeast Karoo Basin, South Africa. *Journal of Geophysical*
1059 *Research: Solid Earth, 127*(6).
1060 Deenen, M. H., Langereis, C. G., van Hinsbergen, D. J., and Biggin, A. J. (2011). Geomagnetic secular
1061 variation and the statistics of palaeomagnetic directions. *Geophysical Journal International*, *186*(2),
1062 509-520.
1063 Demarest Jr, H. H. (1983). Error analysis for the determination of tectonic rotation from
1064 paleomagnetic data. *Journal of Geophysical Research: Solid Earth*, *88*(B5), 4321-4328.
1065 DeMets, C., & Merkouriev, S. (2016). High-resolution estimates of Nubia–Somalia plate motion since
1066 20 Ma from reconstructions of the Southwest Indian Ridge, Red Sea and Gulf of Aden. *Geophysical*
1067 *Journal International*, *207*(1), 317-332.
1068 DeMets, C., & Merkouriev, S. (2019). High-resolution reconstructions of South America plate motion
1069 relative to Africa, Antarctica and North America: 34 Ma to present. *Geophysical Journal*
1070 *International*, *217*(3), 1821-1853.
1071 DeMets, C., & Merkouriev, S. (2021). Detailed reconstructions of India–Somalia Plate motion, 60 Ma to
1072 present: implications for Somalia Plate absolute motion and India–Eurasia Plate
1073 motion. *Geophysical Journal International*, *227*(3), 1730-1767.
1074 DeMets, C., Iaffaldano, G., & Merkouriev, S. (2015). High-resolution Neogene and quaternary estimates
1075 of Nubia-Eurasia-North America plate motion. *Geophysical Journal International*, *203*(1), 416-427.
1076 DeMets, C., Merkouriev, S., & Sauter, D. (2021). High resolution reconstructions of the Southwest
1077 Indian Ridge, 52 Ma to present: implications for the breakup and absolute motion of the Africa
1078 plate. *Geophysical Journal International*, *226*(3), 1461-1497.

1079 Diehl, J. F. (1991). The Elkhorn Mountains revisited: New data for the Late Cretaceous paleomagnetic
1080 field of North America. *Journal of Geophysical Research, 96*(B6). doi:10.1029/91jb00959
1081 Diehl, J. F., Beck, M. E., Beske-Diehl, S., Jacobson, D., & Hearn, B. C. (1983). Paleomagnetism of the Late
1082 Cretaceous-Early Tertiary north-central Montana Alkalic Province. *Journal of Geophysical Research:*
1083 *Solid Earth, 88*(B12), 10593-10609. doi:10.1029/JB088iB12p10593
1084 Diehl, J. F., McClannahan, K. M., & Bornhorst, T. J. (1988). Paleomagnetic results from the Mogollon-
1085 Datil Volcanic Field, southwestern New Mexico, and a refined Mid-Tertiary Reference Pole for
1086 North America. *Journal of Geophysical Research: Solid Earth, 93*(B5), 4869-4879.
1087 doi:10.1029/JB093iB05p04869
1088 Domeier, M., Font, E., Youbi, N., Davies, J., Nemkin, S., Van der Voo, R., ... & Torsvik, T. H. (2021). On the
1089 Early Permian shape of Pangea from paleomagnetism at its core. *Gondwana Research*, *90*, 171-198.
1090 Domeier, M., Font, E., Youbi, N., Davies, J., Nemkin, S., Van der Voo, R., et al. (2021). On the Early
1091 Permian shape of Pangea from paleomagnetism at its core. *Gondwana Research, 90*, 171-198.
1092 Domeier, M., Van der Voo, R., and Torsvik, T. H. (2012). Paleomagnetism and Pangea: the road to
1093 reconciliation. *Tectonophysics*, *514*, 14-43.
1094 Domeier, M., Van der Voo, R., Tomezzoli, R. N., Tohver, E., Hendriks, B. W., Torsvik, T. H., . . . Dominguez,
1095 A. (2011). Support for an "A-type" Pangea reconstruction from high-fidelity Late Permian and Early
1096 to Middle Triassic paleomagnetic data from Argentina. *Journal of Geophysical Research: Solid Earth,*
1097 *116*(B12).
1098 Doubrovine, P. V., Veikkolainen, T., Pesonen, L. J., Piispa, E., Ots, S., Smirnov, A. V., et al. (2019). Latitude
1099 dependence of geomagnetic paleosecular variation and its relation to the frequency of magnetic
1100 reversals: observations from the Cretaceous and Jurassic. *Geochemistry, Geophysics,*
1101 *Geosystems*, *20*(3), 1240-1279.
1102 Doubrovine, P.V. and Tarduno, J.A., (2008). Linking the Late Cretaceous to Paleogene Pacific plate and
1103 the Atlantic bordering continents using plate circuits and paleomagnetic data. *Journal of*
1104 *Geophysical Research*, 113(B7).
1105 Dupont-Nivet, G., Sier, M., Campisano, C. J., Arrowsmith, J. R., DiMaggio, E., Reed, K., . . . Hüsing, S.
1106 (2008). Magnetostratigraphy of the eastern Hadar Basin (Ledi-Geraru research area, Ethiopia) and
1107 implications for hominin paleoenvironments. In *The Geology of Early Humans in the Horn of Africa*.
1108 Dupont-Nivet, G., Van Hinsbergen, D. J., & Torsvik, T. H. (2010). Persistently low Asian paleolatitudes:
1109 Implications for the India-Asia collision history. *Tectonics*, *29*(5).
1110 Ernesto, M., Bellieni, G., Piccirillo, E. M., Marques, L. S., De Min, A., Pacca, I. G., ... & Macedo, J. W. P.
1111 (2003). Paleomagnetic and geochemical constraints on the timing and duration of the CAMP
1112 activity in northeastern Brazil. *GEOPHYSICAL MONOGRAPH-AMERICAN GEOPHYSICAL UNION*, *136*,
1113 129-150.
1114 Ernesto, M., Comin-Chiaramonti, P., & Gomes, C. d. B. (2015). The Early Triassic magmatism of the Alto
1115 ParaguayProvince, Central South America: Paleomagneticand ASM data. *Open Geosciences, 7*(1).
1116 doi:10.1515/geo-2015-0022

1117 Ernesto, M., Demarco, P. N., Xavier, P., Sanchez, L., Schultz, C., & Piñeiro, G. (2020). Age constraints on
1118 the Paleozoic Yaguarí-Buena Vista succession from Uruguay: paleomagnetic and paleontologic
1119 information. *Journal of South American Earth Sciences, 98*. doi:10.1016/j.jsames.2019.102489
1120 Ernesto, M., Zaffani, L. A., & Caminha-Maciel, G. (2021). New paleomagnetic data from the Paraná
1121 Magmatic Province: Brief emplacement time and tectonism. *Journal of South American Earth*
1122 *Sciences, 106*. doi:10.1016/j.jsames.2020.102869
1123 Evans, D. A. (2003). True polar wander and supercontinents. *Tectonophysics*, *362*(1-4), 303-320.
1124 Fisher, R. A. (1953). Dispersion on a sphere. *Proceedings of the Royal Society of London. Series A.*
1125 *Mathematical and Physical Sciences*, *217*(1130), 295-305.
1126 Font, E., Ernesto, M., Silva, P. F., Correia, P. B., & Nascimento, M. A. L. (2009). Palaeomagnetism, rock
1127 magnetism and AMS of the Cabo Magmatic Province, NE Brazil, and the opening of South Atlantic.
1128 *Geophysical Journal International, 179*(2), 905-922. doi:10.1111/j.1365-246X.2009.04333.x
1129 Fournier, M., Chamot-Rooke, N., Petit, C., Huchon, P., Al-Kathiri, A., Audin, L., ... & Merkouriev, S. (2010).
1130 Arabia-Somalia plate kinematics, evolution of the Aden-Owen-Carlsberg triple junction, and
1131 opening of the Gulf of Aden. *Journal of Geophysical Research: Solid Earth*, *115*(B4).
1132 Franco, D. R., Ernesto, M., Ponte-Neto, C. F., Hinnov, L. A., Berquó, T. S., Fabris, J. D., & Rosière, C. A.
1133 (2012). Magnetostratigraphy and mid-palaeolatitude VGP dispersion during the Permo-
1134 Carboniferous Superchron: results from Paraná Basin (Southern Brazil) rhythmites. *Geophysical*
1135 *Journal International*, no-no. doi:10.1111/j.1365-246X.2012.05670.x
1136 Fu, R. R., Kent, D. V., Hemming, S. R., Gutiérrez, P., and Creveling, J. R. (2020). Testing the occurrence of
1137 Late Jurassic true polar wander using the La Negra volcanics of northern Chile. *Earth and Planetary*
1138 *Science Letters, 529*.
1139 Gaina, C., & Jakob, J. (2019). Global eocene tectonic unrest: Possible causes and effects around the
1140 North American plate. *Tectonophysics*, *760*, 136-151.
1141 Gaina, C., Torsvik, T. H., van Hinsbergen, D. J., Medvedev, S., Werner, S. C., & Labails, C. (2013). The
1142 African Plate: A history of oceanic crust accretion and subduction since the
1143 Jurassic. *Tectonophysics*, *604*, 4-25.
1144 Gallo, L. C., Farjat, A. D., Tomezzoli, R. N., Calvagno, J. M., and Hernández, R. M. (2021). Sedimentary
1145 evolution of a Permo-Carboniferous succession in southern Bolivia: Responses to icehouse-
1146 greenhouse transition from a probabilistic assessment of paleolatitudes. *Journal of South American*
1147 *Earth Sciences*, *106*, 102923.
1148 Gallo, L. C., Tomezzoli, R. N., & Cristallini, E. O. (2017). A pure dipole analysis of the G ondwana
1149 apparent polar wander path: Paleogeographic implications in the evolution of P angea.
1150 *Geochemistry, Geophysics, Geosystems, 18*(4), 1499-1519.
1151 Ganerød, M., Smethurst, M. A., Rousse, S., Torsvik, T. H., & Prestvik, T. (2008). Reassembling the
1152 Paleogene–Eocene North Atlantic igneous province: New paleomagnetic constraints from the Isle
1153 of Mull, Scotland. *Earth and Planetary Science Letters, 272*(1-2), 464-475.
1154 doi:10.1016/j.epsl.2008.05.016

1155 Ganerød, M., Smethurst, M. A., Torsvik, T. H., Prestvik, T., Rousse, S., McKenna, C., . . . Hendriks, B. W. H.
1156 (2010). The North Atlantic Igneous Province reconstructed and its relation to the Plume
1157 Generation Zone: the Antrim Lava Group revisited. *Geophysical Journal International*, no-no.
1158 doi:10.1111/j.1365-246X.2010.04620.x
1159 Gao, Y., Zhang, S., Zhao, H., Ren, Q., Yang, T., Wu, H., & Li, H. (2021). North China block underwent
1160 simultaneous true polar wander and tectonic convergence in late Jurassic: New paleomagnetic
1161 constraints. *Earth and Planetary Science Letters*, *567*, 117012.
1162 Gao, Y., Zhang, S., Zhao, H., Ren, Q., Yang, T., Wu, H., & Li, H. (2021). North China block underwent
1163 simultaneous true polar wander and tectonic convergence in late Jurassic: New paleomagnetic
1164 constraints. *Earth and Planetary Science Letters, 567*, 117012.
1165 Garza, R. S. M., Acton, G. D., & Geissman, J. W. (1998). Carboniferous through Jurassic paleomagnetic
1166 data and their bearing on rotation of the Colorado Plateau. *Journal of Geophysical Research: Solid*
1167 *Earth, 103*(B10), 24179-24188.
1168 Gerritsen, D., Vaes, B., and van Hinsbergen, D. J. (2022). Influence of data filters on the position and
1169 precision of paleomagnetic poles: what is the optimal sampling strategy?. *Geochemistry, Geophysics,*
1170 *Geosystems*, e2021GC010269.
1171 Gibbons, A. D., Whittaker, J. M., & Müller, R. D. (2013). The breakup of East Gondwana: Assimilating
1172 constraints from Cretaceous ocean basins around India into a best-fit tectonic model. *Journal of*
1173 *geophysical research: solid earth*, *118*(3), 808-822.
1174 Globerman, B. R., & Irving, E. (1988). Mid-Cretaceous paleomagnetic reference field for North America:
1175 Restudy of 100 Ma intrusive rocks from Arkansas. *Journal of Geophysical Research, 93*(B10).
1176 doi:10.1029/JB093iB10p11721
1177 Goldreich, P., and Toomre, A. (1969). Some remarks on polar wandering. *Journal of Geophysical*
1178 *Research*, *74*(10), 2555-2567.
1179 González, V. R., Renda, E., Vizán, H., Ganerød, M., Puigdomenech, C., & Zaffarana, C. (2022). Deformation
1180 along the Deseado Massif (Patagonia, Argentina) during the Jurassic Period and its relationship
1181 with the Gondwana breakup: paleomagnetic and geochronological constraints. *Tectonophysics,*
1182 *834*, 229389.
1183 Gordon, R. G., and Livermore, R. A. (1987). Apparent polar wander of the mean-lithosphere reference
1184 frame. *Geophysical Journal International*, *91*(3), 1049-1057.
1185 Gradstein, F. M., Ogg, J. G., Schmitz, M. D., & Ogg, G. M. (2020). *Geologic time scale 2020*: Elsevier.
1186 Granot, R., & Dyment, J. (2015). The Cretaceous opening of the South Atlantic Ocean. *Earth and*
1187 *Planetary Science Letters*, *414*, 156-163.
1188 Granot, R., and Dyment, J. (2018). Late Cenozoic unification of East and West Antarctica. *Nature*
1189 *Communications*, *9*(1), 1-10.
1190 Granot, R., Cande, S., Stock, J., & Damaske, D. (2013). Revised Eocene-Oligocene kinematics for the
1191 West Antarctic rift system. *Geophysical Research Letters, 40*(2), 279-284.

1192 Gunderson, J. A., & Sheriff, S. D. (1991). A new Late Cretaceous paleomagnetic pole from the Adel
1193 Mountains, west central Montana. *Journal of Geophysical Research, 96*(B1). doi:10.1029/90jb01963
1194 Gürer, D., Granot, R., & van Hinsbergen, D. J. (2022). Plate tectonic chain reaction revealed by noise in
1195 the Cretaceous quiet zone. *Nature Geoscience, 15*(3), 233-239.
1196 Hagstrum, J. T., & Lipman, P. W. (1986). Paleomagnetism of the structurally deformed Latir volcanic
1197 field, northern New Mexico: Relations to formation of the Questa caldera and development of the
1198 Rio Grande rift. *Journal of Geophysical Research: Solid Earth, 91*(B7), 7383-7402.
1199 doi:10.1029/JB091iB07p07383
1200 Handford, B., Biggin, A., Haldan, M., & Langereis, C. (2021). Analyzing Triassic and Permian
1201 Geomagnetic Paleosecular Variation and the Implications for Ancient Field Morphology.
1202 *Geochemistry, Geophysics, Geosystems, 22*(11), e2021GC009930.
1203 Hansma, J., and Tohver, E. (2020). Southward drift of eastern Australian hotspots in the paleomagnetic
1204 reference frame is consistent with global true polar wander estimates. *Frontiers in Earth Science*,
1205 489.
1206 Hargraves, R. B. (1989). Paleomagnetism of mesozoic kimberlites in southern Africa and the
1207 cretaceous apparent polar wander curve for Africa. *Journal of Geophysical Research, 94*(B2).
1208 doi:10.1029/JB094iB02p01851
1209 Harlan, S. S., & Morgan, L. A. (2010). Paleomagnetic results from Tertiary volcanic strata and
1210 intrusions, Absaroka Volcanic Supergroup, Yellowstone National Park and vicinity: Contributions
1211 to the North American apparent polar wander path. *Tectonophysics, 485*(1-4), 245-259.
1212 doi:10.1016/j.tecto.2009.12.025
1213 Harlan, S. S., Geissman, J. W., Whisner, S. C., & Schmidt, C. J. (2008). Paleomagnetism and geochronology
1214 of sills of the Doherty Mountain area, southwestern Montana: Implications for the timing of fold-
1215 and-thrust belt deformation and vertical-axis rotations along the southern margin of the Helena
1216 salient. *Geological Society of America Bulletin, 120*(9-10), 1091-1104. doi:10.1130/b26313.1
1217 Harrison, C. G. A., and Lindh, T. (1982). A polar wandering curve for North America during the
1218 Mesozoic and Cenozoic. *Journal of Geophysical Research: Solid Earth*, *87*(B3), 1903-1920.
1219 Heslop, D., and Roberts, A. P. (2016). Estimation and propagation of uncertainties associated with
1220 paleomagnetic directions. *Journal of Geophysical Research: Solid Earth*, *121*(4), 2274-2289.
1221 Heslop, D., and Roberts, A. P. (2020). Uncertainty propagation in hierarchical paleomagnetic
1222 reconstructions. *Journal of Geophysical Research: Solid Earth*, *125*(6), e2020JB019488.
1223 Hospers, J. (1954). Rock magnetism and polar wandering. *Nature*, *173*(4416), 1183-1184.
1224 Hussain, A. G., Schult, A., & Soffel, H. (1979). Palaeomagnetism of the basalts of Wadi Abu Tereifiya,
1225 Mandisha and dioritic dykes of Wadi Abu Shihat, Egypt. *Geophysical Journal International, 56*(1),
1226 55-61.
1227 Irving, E. (1964). *Paleomagnetism and its application to geological and geophysical problems*. New
1228 York: Wiley.

1229 Irving, E. (1977). Drift of the major continental blocks since the Devonian. *Nature*, 270(5635), 304-
1230 309.
1231 Irving, E. (1979). Paleopoles and paleolatitudes of North America and speculations about displaced
1232 terrains. *Canadian Journal of Earth Sciences*, *16*(3), 669-694.
1233 Irving, E., & Irving, G. (1982). Apparent polar wander paths Carboniferous through Cenozoic and the
1234 assembly of Gondwana. *Geophysical Surveys, 5*(2), 141-188.
1235 Irving, E., and Irving, G. A. (1982). Apparent polar wander paths Carboniferous through Cenozoic and
1236 the assembly of Gondwana. *Geophysical Surveys*, *5*(2), 141-188.
1237 Jarboe, N. A., Koppers, A. A., Tauxe, L., Minnett, R., and Constable, C. (2012). The online MagIC Database:
1238 data archiving, compilation, and visualization for the geomagnetic, paleomagnetic and rock
1239 magnetic communities. In *AGU Fall Meeting Abstracts* (Vol. 2012, pp. GP31A-1063).
1240 Jay, A. E., Niocaill, C. M., Widdowson, M., Self, S., & Turner, W. (2009). New palaeomagnetic data from
1241 the Mahabaleshwar Plateau, Deccan Flood Basalt Province, India: implications for the
1242 volcanostratigraphic architecture of continental flood basalt provinces. *Journal of the Geological*
1243 *Society*, *166*(1), 13-24.
1244 Johnson, C. L., and McFadden, P. (2007). Time-averaged field and paleosecular
1245 variation. *Geomagnetism*, *5*, 417-453.
1246 Kapawar, M. R., and Mamilla, V. (2020). Paleomagnetism and rock magnetism of early Cretaceous
1247 Rajmahal basalts, NE India: Implications for paleogeography of the Indian subcontinent and
1248 migration of the Kerguelen hotspot. *Journal of Asian Earth Sciences, 201*.
1249 Kent, D. V., & Witte, W. K. (1993). Slow apparent polar wander for North America in the Late Triassic
1250 and large Colorado Plateau rotation. *Tectonics, 12*(1), 291-300.
1251 Kent, D. V., and Irving, E. (2010). Influence of inclination error in sedimentary rocks on the Triassic
1252 and Jurassic apparent pole wander path for North America and implications for Cordilleran
1253 tectonics. *Journal of Geophysical Research: Solid Earth*, *115*(B10).
1254 Kent, D. V., and Muttoni, G. (2020). Pangea B and the late paleozoic ice age. *Palaeogeography,*
1255 *Palaeoclimatology, Palaeoecology*, *553*, 109753.
1256 Kent, D. V., Kjarsgaard, B. A., Gee, J. S., Muttoni, G., & Heaman, L. M. (2015). Tracking the Late Jurassic
1257 apparent (or true) polar shift in U-Pb-dated kimberlites from cratonic North America (Superior
1258 Province of Canada). *Geochemistry, Geophysics, Geosystems*, *16*(4), 983-994.
1259 Kent, D. V., Olsen, P. E., Muttoni, G., & Et-Touhami, M. (2021). A Late Permian paleopole from the
1260 Ikakern Formation (Argana basin, Morocco) and the configuration of Pangea. *Gondwana*
1261 *Research*, *92*, 266-278.
1262 Kidane, T., Carlut, J., Courtillot, V., Gallet, Y., Quidelleur, X., Gillot, P. Y., & Haile, T. (1999). Paleomagnetic
1263 and geochronological identification of the Réunion subchron in Ethiopian Afar. *Journal of*
1264 *Geophysical Research: Solid Earth, 104*(B5), 10405-10419. doi:10.1029/1999jb900014
1265 Kidane, T., Courtillot, V., Manighetti, I., Audin, L., Lahitte, P., Quidelleur, X., . . . Haile, T. (2003). New
1266 paleomagnetic and geochronologic results from Ethiopian Afar: Block rotations linked to rift

overlap and propagation and determination of a ~2 Ma reference pole for stable Africa. *Journal of Geophysical Research: Solid Earth, 108*(B2). doi:10.1029/2001jb000645

Kodama, K. P., (2009). Simplification of the anisotropy-based inclination correction technique for magnetite-and haematite-bearing rocks: a case study for the Carboniferous Glenshaw and Mauch Chunk Formations, North America. *Journal of Geophysical Research.*, 176(2), 467-477.

Kodama, K. P., (2012). *Paleomagnetism of sedimentary rocks: Process and interpretation*. John Wiley and Sons.

Koymans, M. R., van Hinsbergen, D. J. J., Pastor-Galán, D., Vaes, B., & Langereis, C. G. (2020). Towards FAIR paleomagnetic data management through Paleomagnetism. org 2.0. *Geochemistry, Geophysics, Geosystems*, *21*(2), e2019GC008838.

Kristjánsson, L., Gudmundsson, M. T., Smellie, J. L., McIntosh, W. C., & Esser, R. (2005). Palaeomagnetic, 40Ar/39Ar, and stratigraphical correlation of Miocene–Pliocene basalts in the Brandy Bay area, James Ross Island, Antarctica. *Antarctic Science, 17*(3), 409-417. doi:10.1017/s0954102005002853

Kulakov, E. V., Torsvik, T. H., Doubrovine, P. V., Slagstad, T., Ganerød, M., Silkoset, P., & Werner, S. C. (2021). Jurassic fast polar shift rejected by a new high-quality paleomagnetic pole from southwest Greenland. *Gondwana Research*.

Labails, C., Olivet, J. L., Aslanian, D., & Roest, W. R. (2010). An alternative early opening scenario for the Central Atlantic Ocean. *Earth and Planetary Science Letters*, *297*(3-4), 355-368.

Lanci, L., Tohver, E., Wilson, A., and Flint, S. (2013). Upper Permian magnetic stratigraphy of the lower Beaufort Group, Karoo Basin. *Earth and Planetary Science Letters, 375*, 123-134.

Latyshev, A. V., Lapkovskii, A. A., Veselovskiy, R. V., Fetisova, A. M., and Krivolutskaya, N. A. (2021b). Paleomagnetism of the Permian–Triassic Siberian Traps Intrusions from the Kulumbe River Valley, Northwestern Siberian Platform. *Izvestiya, Physics of the Solid Earth, 57*(3), 375-394.

Latyshev, A., Krivolutskaya, N., Ulyakhina, P., Fetisova, A., Veselovskiy, R., Pasenko, A., et al. (2021a). Paleomagnetism of the Permian-Triassic intrusions from the Norilsk region (the Siberian platform, Russia): Implications for the timing and correlation of magmatic events, and magmatic evolution. *Journal of Asian Earth Sciences, 217*.

Leroy, S., Mauffret, A., Patriat, P. and Mercier de Lépinay, B., (2000). An alternative interpretation of the Cayman trough evolution from a reidentification of magnetic anomalies. *Geophysical Journal International,* 141(3): 539-557.

Linares, E., & Valencio, D. A. (1975). Paleomagnetism and K-Ar ages of some trachybasaltic dikes from Río de Los Molinos, Province of Córdoba, Republic of Argentina. *Journal of Geophysical Research, 80*(23), 3315-3321. doi:10.1029/JB080i023p03315

Lock, J., and McElhinny, M. W. (1991). Database design. In *The Global Paleomagnetic Database* (pp. 317-327). Springer, Dordrecht.

1303 Lotfy, H., & Van der Voo, R. (2007). Tropical northeast Africa in the middle–late Eocene:
1304 Paleomagnetism of the marine-mammals sites and basalts in the Fayum province, Egypt. *Journal of*
1305 *African Earth Sciences, 47*(3), 135-152. doi:10.1016/j.jafrearsci.2006.12.005
1306 Mankinen, E. A. (2008). Paleomagnetic study of late Miocene through Pleistocene igneous rocks from
1307 the southwestern USA: Results from the historic collections of the U.S. Geological Survey Menlo
1308 Park laboratory. *Geochemistry, Geophysics, Geosystems, 9*(5), n/a-n/a. doi:10.1029/2008gc001957
1309 Mankinen, E. A., & Cox, A. (1988). Paleomagnetic investigation of some volcanic rocks from the
1310 McMurdo volcanic province, Antarctica. *Journal of Geophysical Research, 93*(B10).
1311 doi:10.1029/JB093iB10p11599
1312 McElhinny, M. W., and McFadden, P. L. (2000). *Paleomagnetism: continents and oceans*. Elsevier.
1313 McElhinny, M. W., Embleton, B. J. J., and Wellman, P. (1974). A synthesis of Australian Cenozoic
1314 palaeomagnetic results. *Geophysical Journal International*, *36*(1), 141-151.
1315 McFadden, P. L., and McElhinny, M. W. (1995). Combining groups of paleomagnetic directions or
1316 poles. *Geophysical Research Letters*, *22*(16), 2191-2194.
1317 McQuarrie, N., & Wernicke, B. P. (2005). An animated tectonic reconstruction of southwestern North
1318 America since 36 Ma. *Geosphere, 1*(3), 147-172.
1319 McQuarrie, N., and Wernicke, B. P. (2005). An animated tectonic reconstruction of southwestern North
1320 America since 36 Ma. *Geosphere*, *1*(3), 147-172.
1321 Meert, J. G., & Tamrat, E. (2006). Paleomagnetic evidence for a stationary Marion hotspot: Additional
1322 paleomagnetic data from Madagascar. *Gondwana Research, 10*(3-4), 340-348.
1323 doi:10.1016/j.gr.2006.04.008
1324 Meert, J. G., Pivarunas, A. F., Evans, D. A., Pisarevsky, S. A., Pesonen, L. J., Li, Z. X., ... and Salminen, J. M.
1325 (2020). The magnificent seven: a proposal for modest revision of the quality
1326 index. *Tectonophysics*, *790*, 228549.
1327 Mejia, V., Böhnel, H., Opdyke, N. D., Ortega-Rivera, M. A., Lee, J. K. W., & Aranda-Gomez, J. J. (2005).
1328 Paleosecular variation and time-averaged field recorded in late Pliocene-Holocene lava flows from
1329 Mexico. *Geochemistry, Geophysics, Geosystems, 6*(7), n/a-n/a. doi:10.1029/2004gc000871
1330 Metelkin, D. V., Kazansky, A. Y., Bragin, V. Y., Tsel'movich, V. A., Lavrenchuk, A. V., and Kungurtsev, L.
1331 V. (2007). Paleomagnetism of the Late Cretaceous intrusions from the Minusa trough (southern
1332 Siberia). *Russian Geology and Geophysics, 48*(2), 185-198.
1333 Molina-Garza, R. S., Acton, G. D., and Geissman, J. W. (1998). Carboniferous through Jurassic
1334 paleomagnetic data and their bearing on rotation of the Colorado Plateau. *Journal of Geophysical*
1335 *Research: Solid Earth*, *103*(B10), 24179-24188.
1336 Molina-Garza, R. S., van Hinsbergen, D. J. J., Rogers, R. D., Ganerød, M., and Dekkers, M. J. (2012). The
1337 Padre Miguel Ignimbrite Suite, central Honduras: Paleomagnetism, geochronology, and tectonic
1338 implications. *Tectonophysics, 574-575*, 144-157.

1339 Moulin, M., Fluteau, F., Courtillot, V., Marsh, J., Delpech, G., Quidelleur, X., et al. (2011). An attempt to
1340 constrain the age, duration, and eruptive history of the Karoo flood basalt: Naude's Nek section
1341 (South Africa). *Journal of Geophysical Research, 116*(B7).
1342 Moulin, M., Fluteau, F., Courtillot, V., Marsh, J., Delpech, G., Quidelleur, X., & Gérard, M. (2017). Eruptive
1343 history of the Karoo lava flows and their impact on early Jurassic environmental change. *Journal of*
1344 *Geophysical Research: Solid Earth*, *122*(2), 738-772.
1345 Mueller, C. O., & Jokat, W. (2019). The initial Gondwana break-up: a synthesis based on new potential
1346 field data of the Africa-Antarctica Corridor. *Tectonophysics*, *750*, 301-328.
1347 Müller, R. D., Royer, J. Y., Cande, S. C., Roest, W. R., & Maschenkov, S. (1999). New constraints on the
1348 Late Cretaceous/Tertiary plate tectonic evolution of the Caribbean. *Sedimentary basins of the*
1349 *world*, *4*, 33-59.
1350 Müller, R. D., Sdrolias, M., Gaina, C., & Roest, W. R. (2008). Age, spreading rates, and spreading
1351 asymmetry of the world's ocean crust. *Geochemistry, Geophysics, Geosystems*, *9*(4).
1352 Müller, R. D., Seton, M., Zahirovic, S., Williams, S. E., Matthews, K. J., Wright, N. M., ... and Cannon, J.
1353 (2016). Ocean basin evolution and global-scale plate reorganization events since Pangea
1354 breakup. *Annual Review of Earth and Planetary Sciences*, *44*(1), 107-138.
1355 Müller, R. D., Zahirovic, S., Williams, S. E., Cannon, J., Seton, M., Bower, D. J., . . . Liu, S. (2019). A global
1356 plate model including lithospheric deformation along major rifts and orogens since the Triassic.
1357 *Tectonics, 38*(6), 1884-1907.
1358 Muttoni, G., and Kent, D. V. (2019). Jurassic monster polar shift confirmed by sequential paleopoles
1359 from Adria, promontory of Africa. *Journal of Geophysical Research: Solid Earth*, *124*(4), 3288-3306.
1360 Muttoni, G., Dallanave, E., and Channell, J. E. T. (2013). The drift history of Adria and Africa from 280
1361 Ma to Present, Jurassic true polar wander, and zonal climate control on Tethyan sedimentary
1362 facies. *Palaeogeography, Palaeoclimatology, Palaeoecology*, *386*, 415-435.
1363 Muttoni, G., Erba, E., Kent, D.V. and Bachtadse, V., (2005). Mesozoic Alpine facies deposition as a result
1364 of past latitudinal plate motion. *Nature*, 434(7029): 59-63.
1365 Muttoni, G., Kent, D. V., Garzanti, E., Brack, P., Abrahamsen, N., & Gaetani, M. (2003). Early permian
1366 pangea 'B'to late permian pangea 'A'. *Earth and Planetary Science Letters*, *215*(3-4), 379-394.
1367 Owen-Smith, T. M., Ganerød, M., van Hinsbergen, D. J., Gaina, C., Ashwal, L. D., & Torsvik, T. H. (2019).
1368 Testing early cretaceous Africa–South America fits with new palaeomagnetic data from the
1369 Etendeka Magmatic Province (Namibia). *Tectonophysics*, *760*, 23-35.
1370 Pastor-Galán, D. (2022). From supercontinent to superplate: Late Paleozoic Pangea's inner
1371 deformation suggests it was a short-lived superplate. *Earth-Science Reviews*, *226*, 103918.
1372 Phillips, J. D., and Forsyth, D. (1972). Plate tectonics, paleomagnetism, and the opening of the Atlantic.
1373 *Geological Society of America Bulletin*, 83(6), 1579-1600.
1374 Pierce, J., Zhang, Y., Hodgin, E. B., & Swanson-Hysell, N. L. (2022). Quantifying inclination shallowing
1375 and representing flattening uncertainty in sedimentary paleomagnetic poles.

1376 Pierce, J., Zhang, Y., Hodgin, E. B., and Swanson-Hysell, N. L. (2022). Quantifying inclination shallowing
1377 and representing flattening uncertainty in sedimentary paleomagnetic poles.
1378 Replumaz, A., & Tapponnier, P. (2003). Reconstruction of the deformed collision zone between India
1379 and Asia by backward motion of lithospheric blocks. *Journal of Geophysical Research: Solid*
1380 *Earth*, *108*(B6).
1381 Reynolds, R. L., Hudson, M. R., & Hon, K. (1986). Paleomagnetic evidence for the timing of collapse and
1382 resurgence of the Lake City Caldera, San Juan Mountains, Colorado. *Journal of Geophysical Research,*
1383 *91*(B9). doi:10.1029/JB091iB09p09599
1384 Riisager, J., Perrin, M., Riisager, P., & Ruffet, G. (2000). Paleomagnetism, paleointensity and
1385 geochronology of Miocene basalts and baked sediments from Velay Oriental, French Massif Central.
1386 *Journal of Geophysical Research: Solid Earth, 105*(B1), 883-896. doi:10.1029/1999jb900337
1387 Riisager, J., Riisager, P., & Pedersen, A. K. (2003). Paleomagnetism of large igneous provinces: case-
1388 study from West Greenland, North Atlantic igneous province. *Earth and Planetary Science Letters,*
1389 *214*(3-4), 409-425.
1390 Riisager, J., Riisager, P., & Pedersen, A. K. (2003). The C27n-C26r geomagnetic polarity reversal
1391 recorded in the west Greenland flood basalt province: How complex is the transitional field?
1392 *Journal of Geophysical Research: Solid Earth, 108*(B3).
1393 Riisager, P., Knight, K. B., Baker, J. A., Ukstins Peate, I., Al-Kadasi, M., Al-Subbary, A., & Renne, P. R.
1394 (2005). Paleomagnetism and 40Ar/39Ar Geochronology of Yemeni Oligocene volcanics:
1395 Implications for timing and duration of Afro-Arabian traps and geometry of the Oligocene
1396 paleomagnetic field. *Earth and Planetary Science Letters, 237*(3-4), 647-672.
1397 doi:10.1016/j.epsl.2005.06.016
1398 Roest, W. R., & Srivastava, S. P. (1989). Sea-floor spreading in the Labrador Sea: A new
1399 reconstruction. *Geology*, *17*(11), 1000-1003.
1400 Rose, I. R., Zhang, Y., and Swanson-Hysell, N. L. (2022). Bayesian paleomagnetic Euler pole inversion
1401 for paleogeographic reconstruction and analysis. *Journal of Geophysical Research: Solid*
1402 *Earth*, *127*(10), e2021JB023890.
1403 Rowley, D. B. (2019). Comparing paleomagnetic study means with apparent wander paths: A case
1404 study and paleomagnetic test of the Greater India versus Greater Indian Basin hypotheses.
1405 *Tectonics*, 38(2), 722-740.
1406 Ruiz González, V., Renda, E. M., Vizán, H., Ganerød, M., Puigdomenech, C. G., and Zaffarana, C. B. (2022).
1407 Deformation along the Deseado Massif (Patagonia, Argentina) during the Jurassic Period and its
1408 relationship with the Gondwana breakup: paleomagnetic and geochronological constraints.
1409 *Tectonophysics, 834*.
1410 Ruiz-Martínez, V. C., Urrutia-Fucugauchi, J., & Osete, M. L. (2010). Palaeomagnetism of the Western
1411 and Central sectors of the Trans-Mexican volcanic belt-implications for tectonic rotations and
1412 palaeosecular variation in the past 11 Ma. *Geophysical Journal International, 180*(2), 577-595.

1413 Runcorn, S. K. (1959). On the hypothesis that the mean geomagnetic field for parts of geological time
1414 has been that of a geocentric axial multipole. *Journal of Atmospheric and Terrestrial Physics*, *14*(1-
1415 2), 167-174.
1416 Sahabi, M., Aslanian, D., & Olivet, J. L. (2004). A new starting point for the history of the central
1417 Atlantic. *Comptes Rendus Geoscience*, *336*(12), 1041-1052.
1418 Scealy, J. L., Heslop, D., Liu, J., & Wood, A. T. (2022). Directions Old and New: Palaeomagnetism and
1419 Fisher (1953) Meet Modern Statistics. *International Statistical Review*, *90*(2), 237-258.
1420 Schettino, A., and Scotese, C. R. (2005). Apparent polar wander paths for the major continents (200
1421 Ma to the present day): a palaeomagnetic reference frame for global plate tectonic
1422 reconstructions. *Geophysical Journal International*, *163*(2), 727-759.
1423 Seton, M., Müller, R. D., Zahirovic, S., Gaina, C., Torsvik, T., Shephard, G., ... and Chandler, M. (2012).
1424 Global continental and ocean basin reconstructions since 200 Ma. *Earth-Science Reviews*, *113*(3-4),
1425 212-270.
1426 Shive, P. N., & Frerichs, W. E. (1974). Paleomagnetism of the Niobrara Formation in Wyoming,
1427 Colorado, and Kansas. *Journal of Geophysical Research, 79*(20), 3001-3007.
1428 doi:10.1029/JB079i020p03001
1429 Shive, P. N., & Pruss, E. F. (1977). A paleomagnetic study of basalt flows from the Absaroka Mountains,
1430 Wyoming. *Journal of Geophysical Research, 82*(20), 3039-3048. doi:10.1029/JB082i020p03039
1431 Somoza, R. (2007). Eocene paleomagnetic pole for South America: Northward continental motion in
1432 the Cenozoic, opening of Drake Passage and Caribbean convergence. *Journal of Geophysical*
1433 *Research, 112*(B3). doi:10.1029/2006jb004610
1434 Somoza, R., & Zaffarana, C. B. (2008). Mid-Cretaceous polar standstill of South America, motion of the
1435 Atlantic hotspots and the birth of the Andean cordillera. *Earth and Planetary Science Letters, 271*(1-
1436 4), 267-277. doi:10.1016/j.epsl.2008.04.004
1437 Somoza, R., Singer, S., & Coira, B. (1996). Paleomagnetism of upper Miocene ignimbrites at the Puna:
1438 An analysis of vertical-axis rotations in the Central Andes. *Journal of Geophysical Research: Solid*
1439 *Earth, 101*(B5), 11387-11400. doi:10.1029/95jb03467
1440 Somoza, R., Singer, S., & Tomlinson, A. (1999). Paleomagnetic study of upper Miocene rocks from
1441 northern Chile: Implications for the origin of Late Miocene-Recent tectonic rotations in the
1442 southern Central Andes. *Journal of Geophysical Research: Solid Earth, 104*(B10), 22923-22936.
1443 doi:10.1029/1999jb900215
1444 Srivastava, S. P., & Roest, W. R. (1996). Comment on "Porcupine plate hypothesis" by MF Gerstell and
1445 JM Stock (Marine Geophysical Researches 16, pp. 315–323, 1994). *Marine Geophysical*
1446 *Researches*, *18*(5), 589-593.
1447 Steiner, M. B. (2003). A cratonic Middle Jurassic paleopole: Callovian-Oxfordian stillstand (J-2 cusp),
1448 rotation of the Colorado Plateau, and Jurassic North American apparent polar
1449 wander. *Tectonics*, *22*(3).

1450 Steiner, M. B. (2003). A cratonic Middle Jurassic paleopole: Callovian-Oxfordian stillstand (J-2 cusp),
1451 rotation of the Colorado Plateau, and Jurassic North American apparent polar wander. *Tectonics,*
1452 *22*(3).
1453 Swanson-Hysell, N. L., Ramezani, J., Fairchild, L. M., and Rose, I. R. (2019). Failed rifting and fast
1454 drifting: Midcontinent Rift development, Laurentia's rapid motion and the driver of Grenvillian
1455 orogenesis. *Bulletin*, *131*(5-6), 913-940.
1456 Symons, D. T. A., Erdmer, P., & McCausland, P. J. A. (2003). New 42 Ma cratonic North American
1457 paleomagnetic pole from the Yukon underscores another Cordilleran paleomagnetism-geology
1458 conundrum. *Canadian Journal of Earth Sciences, 40*(10), 1321-1334. doi:10.1139/e03-047
1459 Tauxe, L., and Kent, D. V. (2004). A simplified statistical model for the geomagnetic field and the
1460 detection of shallow bias in paleomagnetic inclinations: was the ancient magnetic field dipolar?
1461 *Geophysical Monograph Series*, 145, 101-155.
1462 Tauxe, L., Banerjee, S. K., Butler, R. F., and van der Voo, R. (2010). *Essentials of paleomagnetism*.
1463 Berkeley, CA: University of California Press.
1464 Tauxe, L., Gans, P., & Mankinen, E. A. (2004). Paleomagnetism and40Ar/39Ar ages from volcanics
1465 extruded during the Matuyama and Brunhes Chrons near McMurdo Sound, Antarctica.
1466 *Geochemistry, Geophysics, Geosystems, 5*(6). doi:10.1029/2003gc000656
1467 Tauxe, L., Luskin, C., Selkin, P., Gans, P., & Calvert, A. (2004). Paleomagnetic results from the Snake
1468 River Plain: Contribution to the time-averaged field global database. *Geochemistry, Geophysics,*
1469 *Geosystems, 5*(8). doi:10.1029/2003gc000661
1470 Tebbens, S. F., and Cande, S. C. (1997). Southeast Pacific tectonic evolution from early Oligocene to
1471 present. *Journal of Geophysical Research: Solid Earth*, *102*(B6), 12061-12084.
1472 Thompson, R., and Clark, R. M. (1981). Fitting polar wander paths. *Physics of the Earth and Planetary*
1473 *Interiors*, *27*(1), 1-7.
1474 Torsvik, T. H., and Cocks, L. R. M. (2016). *Earth history and palaeogeography*. Cambridge University
1475 Press.
1476 Torsvik, T. H., Eide, E. A., Redfield, T. F., Lundin, E., Smethurst, M. A., & Ebbing, J. (2004). South Atlantic
1477 reconstructions: a self-consistent model. *NGU Report 2004.024*, 100.
1478 Torsvik, T. H., Müller, R. D., Van der Voo, R., Steinberger, B., and Gaina, C. (2008). Global plate motion
1479 frames: toward a unified model. *Reviews of Geophysics*, 46(3).
1480 Torsvik, T. H., Rousse, S., Labails, C., & Smethurst, M. A. (2009). A new scheme for the opening of the
1481 South Atlantic Ocean and the dissection of an Aptian salt basin. *Geophysical Journal*
1482 *International*, *177*(3), 1315-1333.
1483 Torsvik, T. H., Smethurst, M. A., Meert, J. G., Van der Voo, R., McKerrow, W. S., Brasier, M. D., et al.
1484 (1996). Continental break-up and collision in the Neoproterozoic and Palaeozoic—a tale of Baltica
1485 and Laurentia. *Earth-Science Reviews*, *40*(3-4), 229-258.

1486 Torsvik, T. H., Van der Voo, R., Preeden, U., Mac Niocaill, C., Steinberger, B., Doubrovine, P. V., et al.
1487 (2012). Phanerozoic polar wander, palaeogeography and dynamics. *Earth-Science Reviews*, 114(3-
1488 4), 325-368.
1489 Torsvik, T.H. and van der Voo, R., (2002). Refining Gondwana and Pangea palaeogeography: estimates
1490 of Phanerozoic non-dipole (octupole) fields. *Geophysical Journal International*, 151(3): 771-794.
1491 Torsvik, T.H., Doubrovine, P.V., Domeier, M. (2014). Continental drift (paleomagnetism). In: Rink, W.,
1492 Thompson, J. (eds) Encyclopedia of Scientific Dating Methods. Springer, Dordrecht.
1493 Tucholke, B.E. and Sibuet, J.-C. (2012). Problematic plate reconstruction. *Nature Geoscience*, 5(10):
1494 676-677.
1495 Vaes, B., Gallo, L. C., and van Hinsbergen, D. J. (2022). On pole position: causes of dispersion of the
1496 paleomagnetic poles behind apparent polar wander paths. *Journal of Geophysical Research: Solid*
1497 *Earth*, *127*(4), e2022JB023953.
1498 Vaes, B., Li, S., Langereis, C. G., and van Hinsbergen, D. J. (2021). Reliability of palaeomagnetic poles
1499 from sedimentary rocks. *Geophysical Journal International*, 225(2), 1281–1303.
1500 Van Alstine, D. R., and de Boer, J. (1978). A new technique for constructing apparent polar wander
1501 paths and the revised Phanerozoic path for North America. *Geology*, 6(3), 137-139.
1502 Van de Lagemaat, S. H., Swart, M. L., Vaes, B., Kosters, M. E., Boschman, L. M., Burton-Johnson, A., ... and
1503 Van Hinsbergen, D. J. (2021). Subduction initiation in the Scotia Sea region and opening of the
1504 Drake Passage: When and why?. *Earth-Science Reviews*, *215*, 103551.
1505 Van der Voo, R. (1990a). The reliability of paleomagnetic data. *Tectonophysics*, *184*(1), 1-9.
1506 Van der Voo, R. (1990b). Phanerozoic paleomagnetic poles from Europe and North America and
1507 comparisons with continental reconstructions. *Reviews of Geophysics*, *28*(2), 167-206.
1508 Van der Voo, R., and French, R. B. (1974). Apparent polar wandering for the Atlantic-bordering
1509 continents: Late Carboniferous to Eocene. *Earth-Science Reviews*, *10*(2), 99-119.
1510 Van der Voo, R., van Hinsbergen, D.J.J., Domeier, M., Spakman, W. and Torsvik, T.H., (2015). Latest
1511 Jurassic–earliest Cretaceous closure of the Mongol-Okhotsk Ocean: A paleomagnetic and
1512 seismological-tomographic analysis, Late Jurassic Margin of Laurasia–A Record of Faulting
1513 Accommodating Plate Rotation. *Geological Society of America Special Papers*, pp. 589-606.
1514 Van Hinsbergen, D. J. J., Straathof, G. B., Kuiper, K. F., Cunningham, W. D., & Wijbrans, J. (2008). No
1515 vertical axis rotations during Neogene transpressional orogeny in the NE Gobi Altai: coinciding
1516 Mongolian and Eurasian early Cretaceous apparent polar wander paths. *Geophysical Journal*
1517 *International, 173*(1), 105-126. doi:10.1111/j.1365-246X.2007.03712.x
1518 Van Hinsbergen, D. J., de Groot, L. V., van Schaik, S. J., Spakman, W., Bijl, P. K., Sluijs, A., et al. (2015). A
1519 paleolatitude calculator for paleoclimate studies. *PLoS One*, 10(6), e0126946.
1520 Van Hinsbergen, D. J., Spakman, W., Vissers, R. L., and van der Meer, D. G. (2017). Comment on
1521 "Assessing Discrepancies Between Previous Plate Kinematic Models of Mesozoic Iberia and Their
1522 Constraints" by Barnett-Moore Et Al. *Tectonics*, *36*(12), 3277-3285.

1523 Van Hinsbergen, D. J., Torsvik, T. H., Schmid, S. M., Maţenco, L. C., Maffione, M., Vissers, R. L., . . .
1524 Spakman, W. (2020). Orogenic architecture of the Mediterranean region and kinematic
1525 reconstruction of its tectonic evolution since the Triassic. *Gondwana Research, 81*, 79-229.
1526 Van Hinsbergen, D.J.J., Mensink, M., Langereis, C.G., Maffione, M., Spalluto, L., Tropeano, M. and Sabato,
1527 L., (2014). Did Adria rotate relative to Africa? *Solid Earth*, 5(2): 611-629.
1528 Vissers, R. L. M., & Meijer, P. T. (2012). Iberian plate kinematics and Alpine collision in the
1529 Pyrenees. *Earth-Science Reviews*, *114*(1-2), 61-83.
1530 Vissers, R. L. M., & Meijer, P. T. (2012). Mesozoic rotation of Iberia: Subduction in the Pyrenees?. *Earth-*
1531 *Science Reviews*, *110*(1-4), 93-110.
1532 Vizán, H. (1998). Paleomagnetism of the Lower Jurassic Lepáand Osta Arena formations, Argentine
1533 Patagonia. *Journal of South American Earth Sciences*, *11*(4), 333-350.
1534 Vugteveen, R. W., Barnes, A. E., & Butler, R. F. (1981). Paleomagnetism of the Roskruge and Gringo
1535 Gulch Volcanics, southeast Arizona. *Journal of Geophysical Research, 86*(B5).
1536 doi:10.1029/JB086iB05p04021
1537 Whittaker, J. M., Muller, R. D., Leitchenkov, G., Stagg, H., Sdrolias, M., Gaina, C., & Goncharov, A. (2007).
1538 Major Australian-Antarctic plate reorganization at Hawaiian-Emperor bend
1539 time. *Science*, *318*(5847), 83-86.
1540 Whittaker, J. M., Williams, S. E., & Müller, R. D. (2013). Revised tectonic evolution of the Eastern Indian
1541 Ocean. *Geochemistry, Geophysics, Geosystems*, *14*(6), 1891-1909.
1542 Williams, S. E., Whittaker, J. M., & Müller, R. D. (2011). Full-fit, palinspastic reconstruction of the
1543 conjugate Australian-Antarctic margins. *Tectonics*, *30*(6).
1544 Wright, N. M., Müller, R. D., Seton, M., & Williams, S. E. (2015). Revision of Paleogene plate motions in
1545 the Pacific and implications for the Hawaiian-Emperor bend. *Geology*, *43*(5), 455-458.
1546 Wright, N. M., Seton, M., Williams, S. E., & Mueller, R. D. (2016). The Late Cretaceous to recent tectonic
1547 history of the Pacific Ocean basin. *Earth-Science Reviews, 154*, 138-173.
1548 Wu, L., Murphy, J. B., Quesada, C., Li, Z. X., Waldron, J. W., Williams, S., et al. (2021). The amalgamation
1549 of Pangea: Paleomagnetic and geological observations revisited. *Bulletin*, 133(3-4), 625-646.
1550 Yang, Y.-T., Guo, Z.-X., Song, C.-C., Li, X.-B. and He, S., (2015). A short-lived but significant Mongol–
1551 Okhotsk collisional orogeny in latest Jurassic–earliest Cretaceous. *Gondwana Research*, 28(3):
1552 1096-1116.
1553 Yi, Z., Liu, Y., & Meert, J. G. (2019). A true polar wander trigger for the Great Jurassic East Asian
1554 Aridification. *Geology, 47*(12), 1112-1116.
1555 Yonkee, W.A. and Weil, A.B., (2015). Tectonic evolution of the Sevier and Laramide belts within the
1556 North American Cordillera orogenic system. *Earth-Science Reviews*, 150: 531-593.

Figures and tables

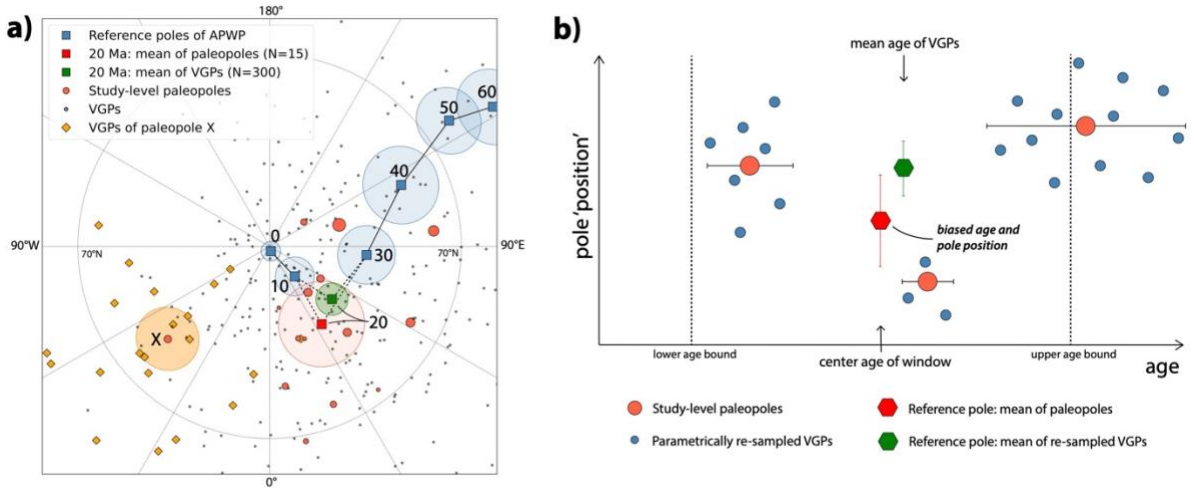

Fig. 1. **a)** Example of an apparent polar wander path for the last 60 Ma (blue squares, with 95% confidence regions). The 20 Ma reference pole is computed in two ways: by taking the mean of the 15 paleopoles (light red circles) – as done in the conventional approach to calculating APWPs – or by taking the mean of 300 VGPs (grey dots) that were used to calculate those paleopoles. Note the difference in the reference pole position (green versus red square) and the size of its 95% confidence region. The size of the paleopoles corresponds to the number of VGPs from which that paleopole is derived, ranging between 5 and 60. Paleopole X and the 20 VGPs from which it was calculated are highlighted in orange. **b)** Schematic comparison between the pole-based approach to calculating APWPs and the VGP-based approach developed by Vaes et al. (2022). Note that the oldest study-level paleopole does not contribute to the reference pole in the pole-based approach but that nearly half of its VGPs are used in the calculation of the reference pole in the VGP-based approach. This way, both the number of sites behind each paleopole and its spatial and temporal uncertainties are taken into account in the computation of the reference poles of an APWP. In the VGP-based approach used in this study, the mean age of the (re-sampled) VGPs is used for the reference pole, rather than the center age of the time window.

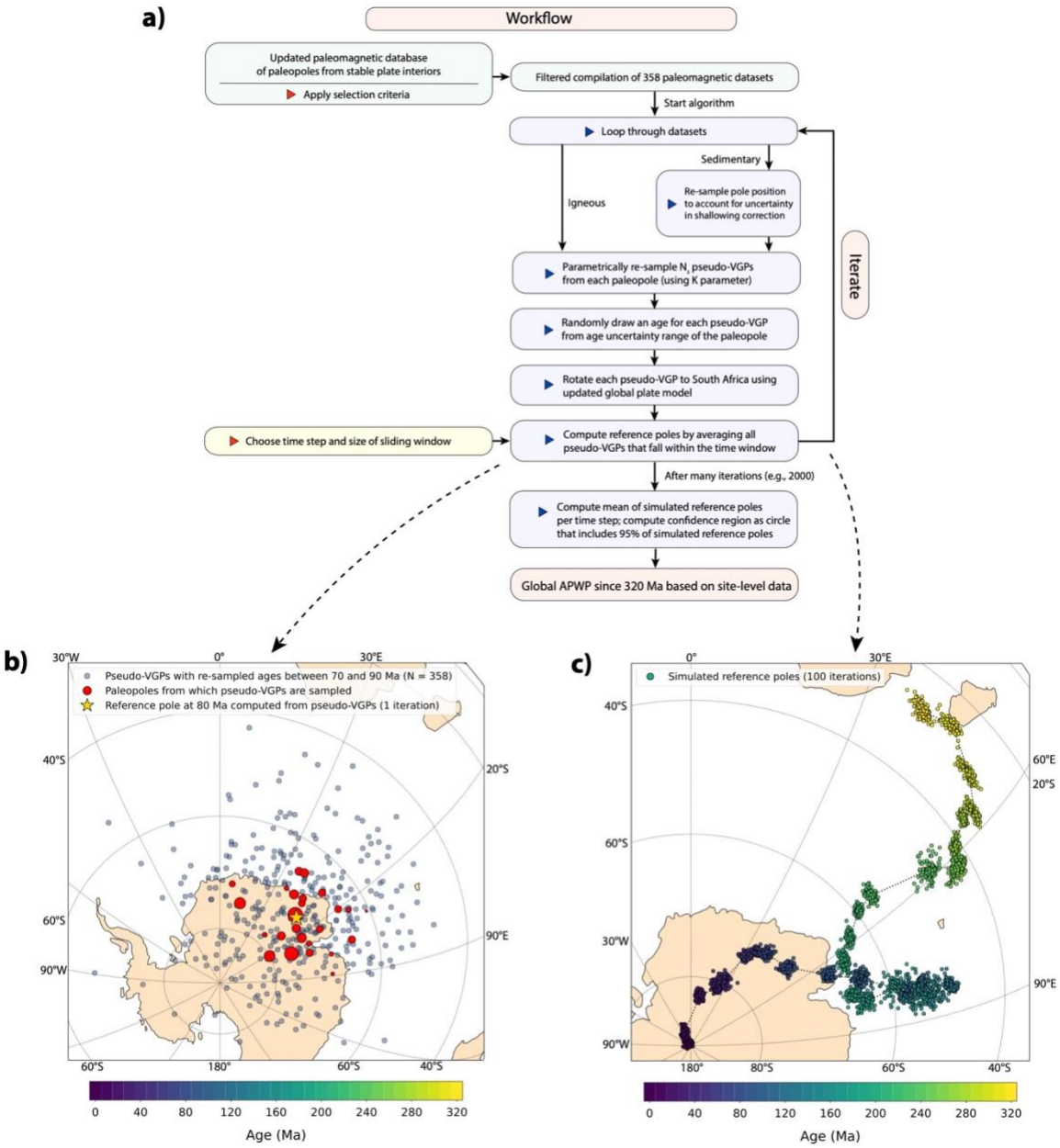

Fig. 2. a) Workflow for the computation of the new global APWP. **b)** Orthographic plot of the parametrically re-sampled VGPs with ages between 70 and 90 Ma (blue circles), which are derived from the paleopoles (red circles, size corresponds to number of VGPs sampled from pole) and used to compute a reference pole at 80 Ma. **c)** Orthographic plot showing the simulated reference poles obtained by 100 iterations.

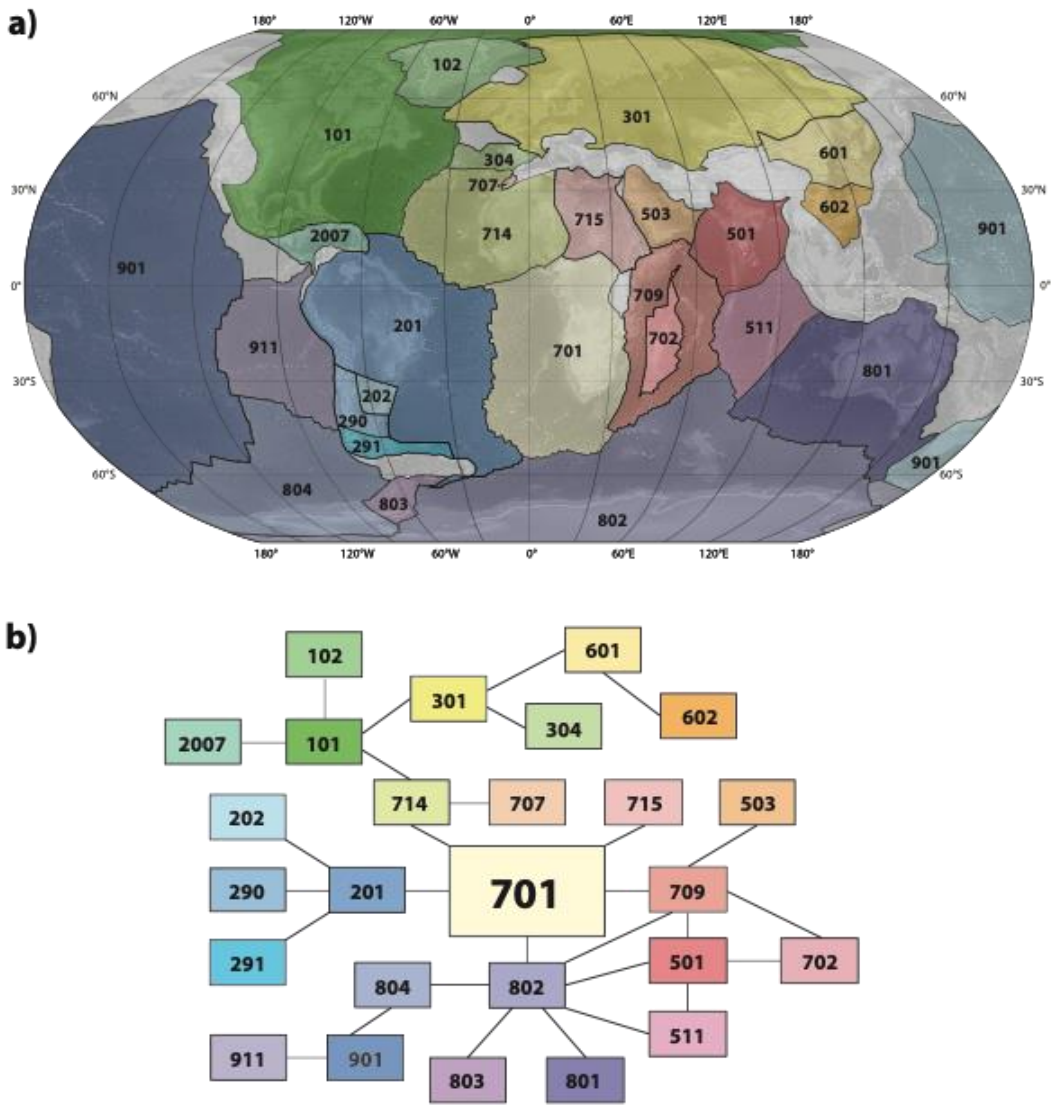

Fig. 3. a) Simplified global map of the tectonic plates from which the paleomagnetic data used for the global APWP is derived. **b)** Schematic representation of plate circuit. See Table 1 and S1 for more details. *Modified from van Hinsbergen et al. (2015).*

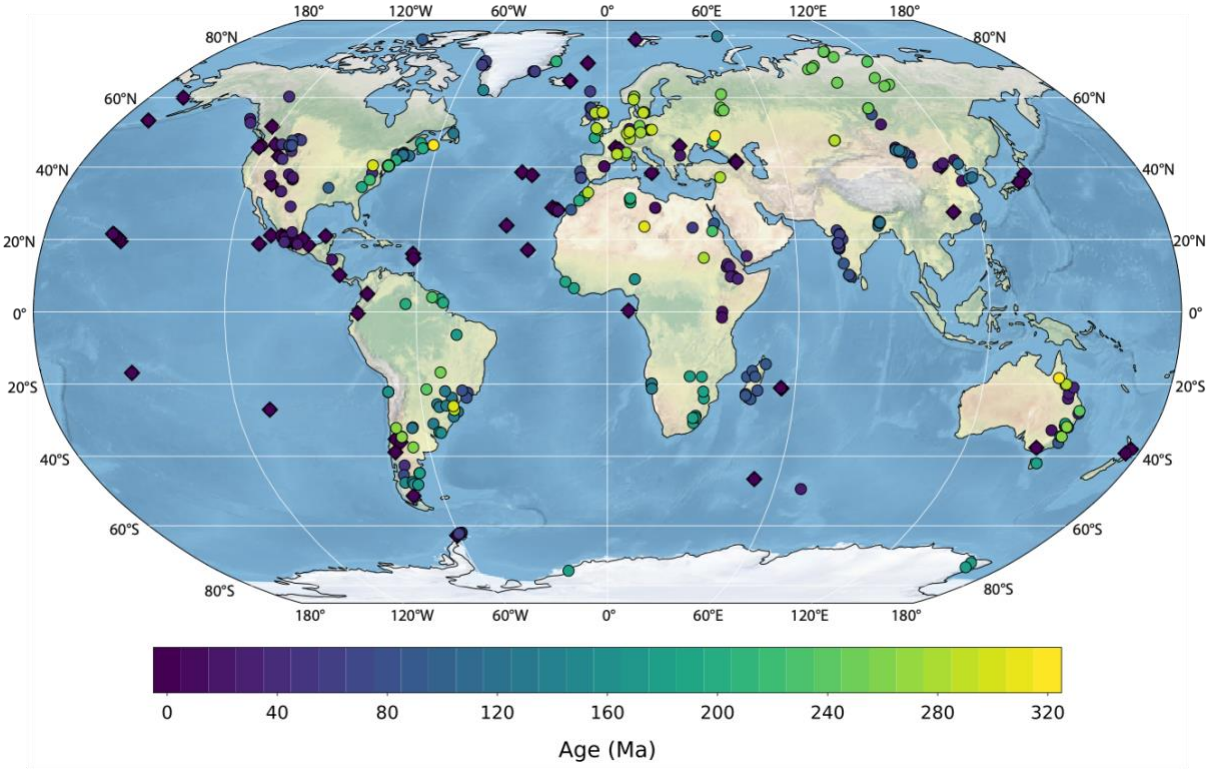

Fig. 4. Sampling locations of the 350 paleomagnetic datasets used for the calculation of the global APWP. Locations are colored by the mean age of the rocks. Diamonds indicate datasets from the PSV10 database (Cromwell et al., 2018).

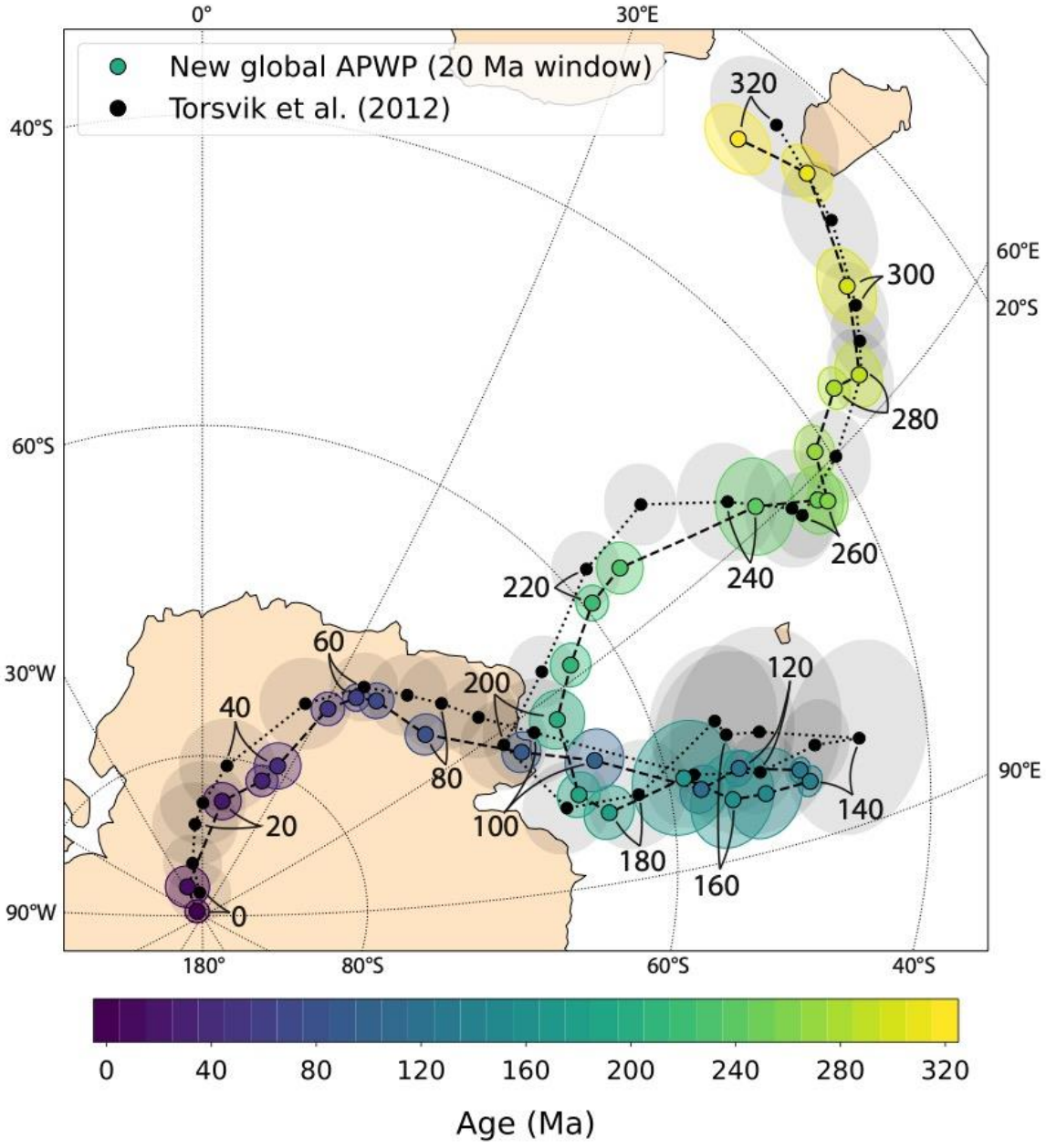

Fig. 5. Orthographic plot of the new global APWP for the last 320 Ma in South African coordinates, calculated using a 20 Ma sliding window. Reference poles and 95% confidence regions are colored by their age. Global APWP of Torsvik et al. (2012) is plotted with black circles (and light grey A95 confidence circles). Numbers indicate the center age of the time windows and are shown per 20 Ma.

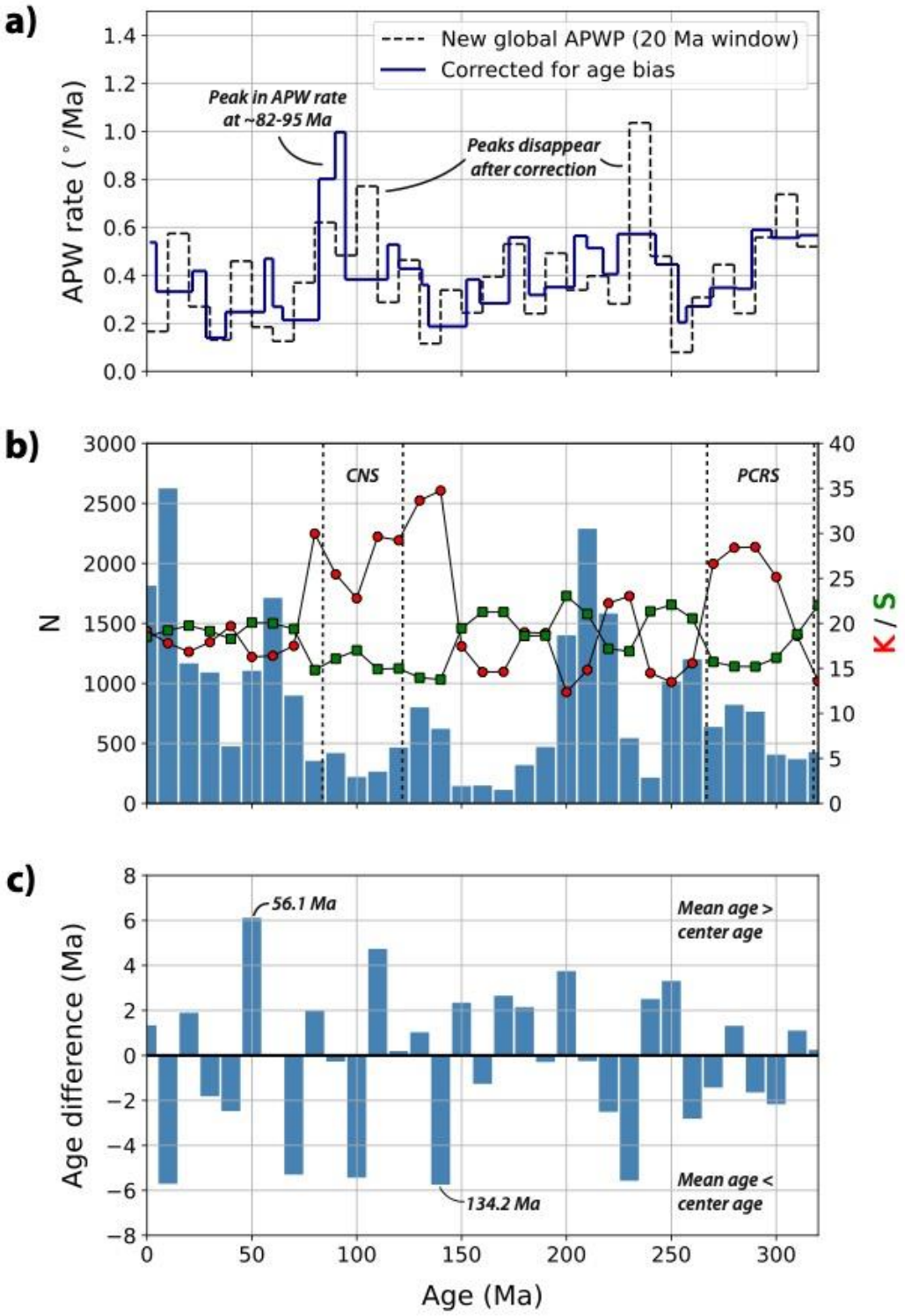

Fig. 6. a) APW rates derived from the new global APWP per 10 Ma age interval (black, dashed line). Rates computed using the mean ages of the *pseudo*-VGPs are shown by the blue line. **b)** Mean number of sites (N), K and VGP dispersion (S) of the *pseudo*-VGPs that fall within each time window. The age range of the Cretaceous Normal Superchron (CNS) and Permo-Carboniferous Reversed Superchron (PCRS) are indicated. **c)** Age difference between the mean age of the *pseudo*-VGPs and the center age of the time window.

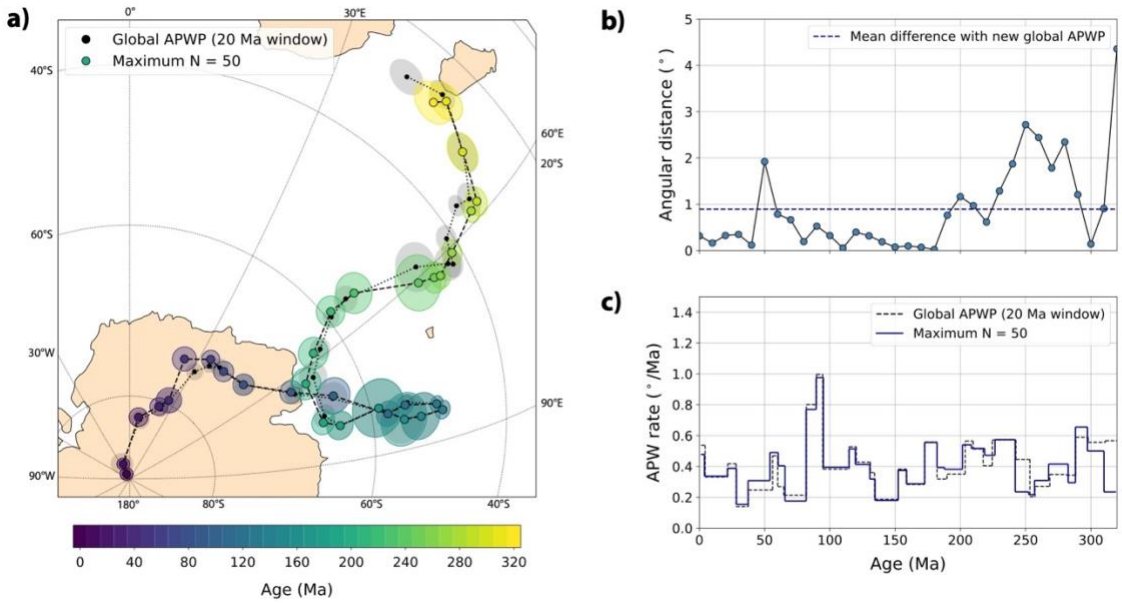

Fig. 7. a) Global APWP calculated with a maximum of N=50 per dataset. The global APWP of Fig. 5 is plotted with the black circles. **b)** Angular difference between the two APWPs. **c)** Comparison of APW rates.

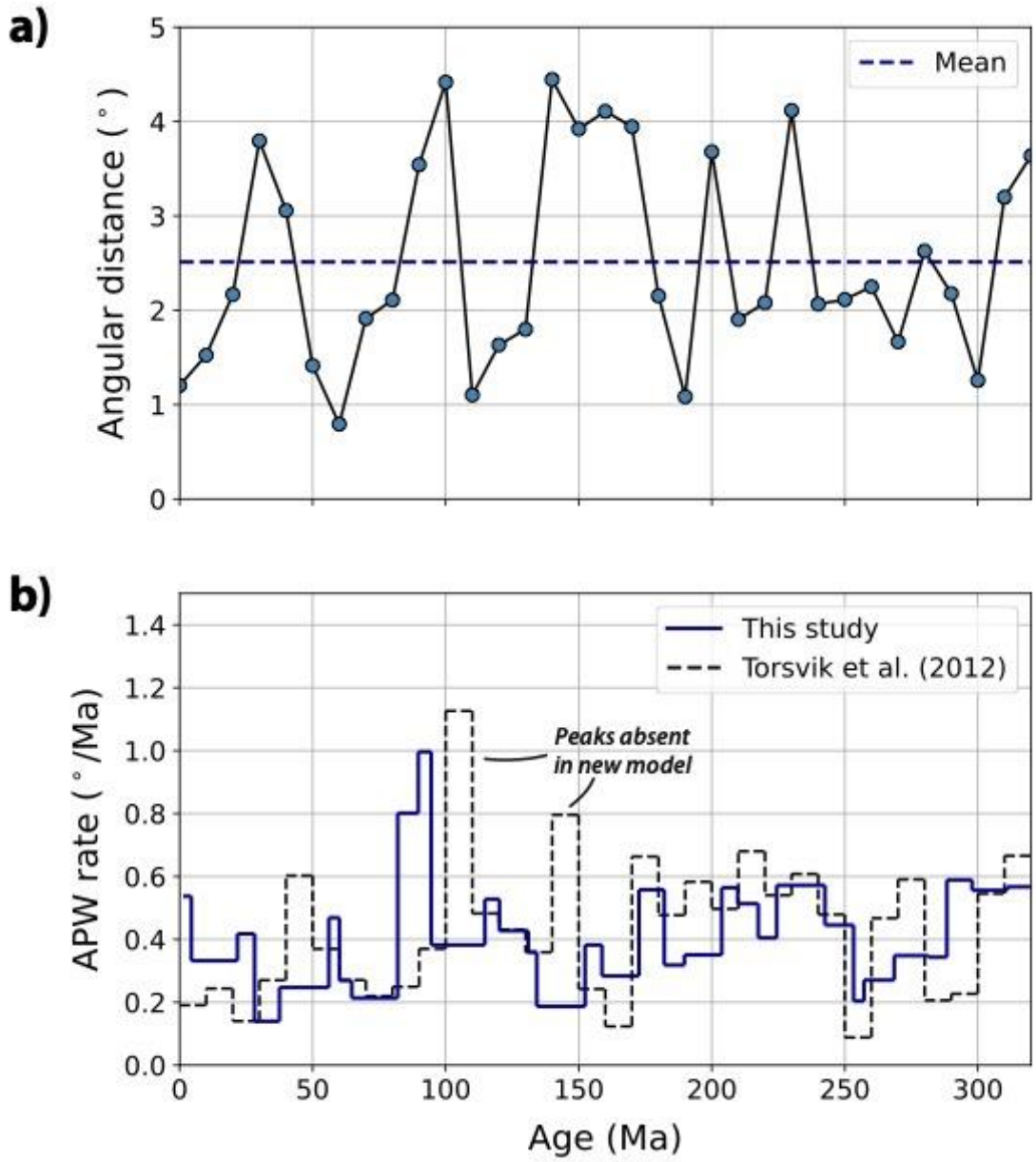

Fig. 8. a) Angular difference between the new VGP-based global APWP and the pole-based APWP of Torsvik et al. (2012), both in South African coordinates. The dashed blue line is the mean angular distance of 2.5°. **b)** APW rates determined in this study compared to those derived from the global APWP of Torsvik et al. (2012).

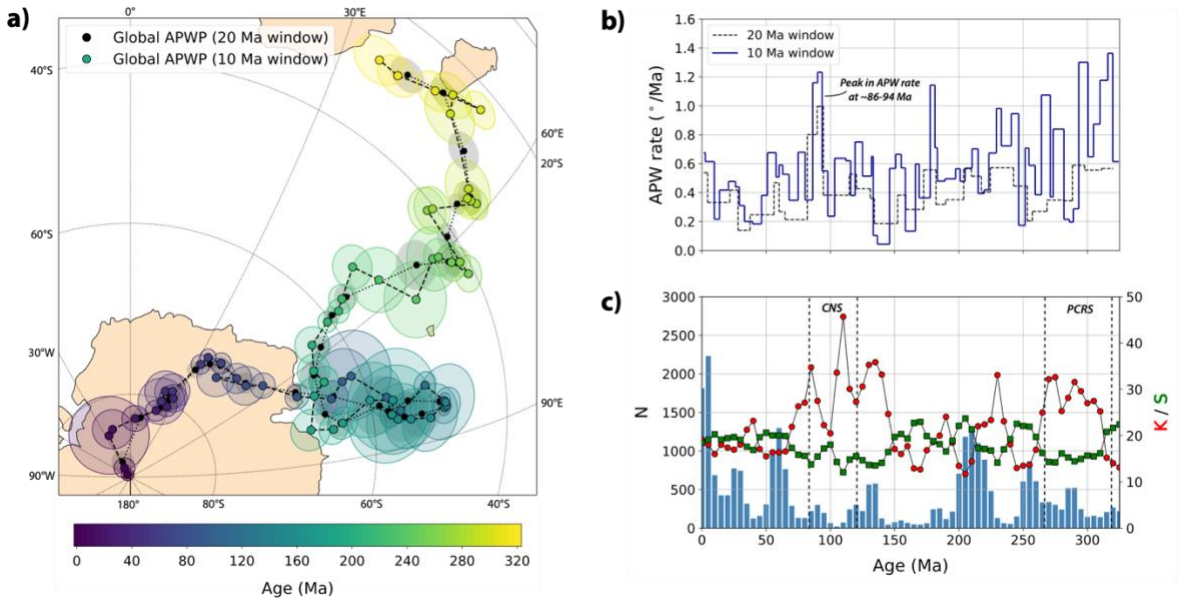

Fig. 9. a) Global APWP for the last 325 Ma (in South African coordinates) computed at a 5 Ma resolution with a 10 Ma window. The path calculated using a 20 Ma window is plotted with the black circles. **b)** Comparison of APW rates. **c)** Statistical parameters for the 5 Ma-resolution-APWP; see Fig. 6 for more information.

Plate	ID	Moves relative to	Age range (Ma)	References	Notes
North America	101	Northwest Africa	0 - 203	DeMets et al. (2015),Müller et al. (1999, 2008), Gürer et al. (2022), van Hinsbergen et al. (2020), Sahabi et al., (2004), Labails et al. (2010)	Fixed to Northwest Africa from 203 to 330 Ma*
Greenland	102	North America	0 - 125	Gaina and Jakob (2019), Torsvik et al., (2008a), Roest and Srivastava (1989), Torsvik et al. (2012)	Fixed to North America from 125 to 330 Ma*
South America	201	South Africa	0 - 133.6	DeMets and Merkouriev (2019), Müller et al. (1999), Granot and Dyment (2015), Gaina et al. (2013), Torsvik et al. (2009)	Fixed to South Africa from 133.6 to 330 Ma*
Parana	202	South America	0 - 150	Torsvik et al. (2009)	Fixed to South America from 150 to 330 Ma*
Colorado	290	South America	0 - 150	Torsvik et al. (2009)	Fixed to South America from 150 to 330 Ma*
Patagonia	291	South America	0 - 190	Torsvik et al. (2009)	Fixed to South America from 190 to 330 Ma*
Eurasia	301	North America	0 - 220	DeMets et al. (2015), Vissers and Meijer (2012a, b), Srivastava and Roest (1989, 1996), Torsvik et al. (2008a), Alvey (2009)	Fixed to North America from 220 to 330 Ma*
Iberia	304	Eurasia	0 - 83.65^	Vissers and Meijer (2012a, b)	
India	501	Somalia	0 - 59.237	DeMets and Merkouriev (2021)	
		Capricorn	59.237 - 83.65	Bull et al. (2010)	Correction for motion since ~16 Ma between Capricorn plate and India (see DeMets and Merkouriev, 2021)
		Madagascar	83.65 - 126.51	Gibbons et al. (2013)	
		Antarctica	126.51 - 160	Gibbons et al. (2013)	Fixed to Antarctica from 160 to 330 Ma
Arabia	503	Somalia	0 - 35	DeMets and Merkouriev (2016), Fournier et al. (2010)	Fixed to Northeast Africa from 35 to 330 Ma
Capricorn	511	India	0 - 59.237	Bull et al. (2010)	Fixed to India between ~16 to ~59 Ma
		Antarctica	59.237 - 83.65^	Cande and Patriat (2015)	
North China	601	Eurasia	0 - 130^	Torsvik and Cocks (2016)	Assumed fixed to Eurasia
South China	602	North China	0 - 130^	Replumaz and Taponnier (2003)	Fixed to North China from 10 to 130 Ma
Madagascar	702	Somalia	0 - 170	Gaina et al. (2013)	Fixed to Somalia from 170 to 330 Ma
Moroccan Meseta	707	Northwest Africa	0 - 50	Van Hinsbergen et al. (2020)	Fixed to Northwest Africa from 50 to 330 Ma
Somalia	709	South Africa	0 - 19.535	DeMets and Merkouriev (2016)	Fixed to South Africa from ~20 to 330 Ma
Northwest Africa	714	South Africa	120 - 133.565	Torsvik et al. (2009)	Fixed to South Africa after 120 Ma and before 133.565 Ma*
Northeast Africa	715	South Africa	83.65 - 121.4	Torsvik et al. (2004)	Fixed to South Africa after 83.65 Ma and before 121.4 Ma*
Australia	801	Antarctica	0 - 136.657	Cande and Stock (2004), Whittaker et al. (2007, 2013), Williams et al. (2011)	Fixed to Antarctica from ~136 to 330 Ma
Antarctica	802	South Africa	0 - 51.724	DeMets et al. (2021)	
		Somalia	51.724 - 182	Cande and Patriat (2015), Mueller and Jokat (2019)	Fixed to Somalia from 182 to 330 Ma
Antarctic Peninsula	803	Antarctica	0 - 140	Van de Lagemaat et al. (2021)	Fixed to Antarctica from ~140-0 Ma
Marie Byrd Land	804	Antarctica	0 - 83.65^	Granot and Dyment (2018), Granot et al. (2013a, b), Cande and Stock (2004)	Fixed to Antarctica from ~62 Ma to 83.65 Ma (Van de Lagemaat et al., 2021)
Pacific	901	Marie Byrd Land	0 - 83.65^	Croon et al. (2008), Wright et al. (2015, 2016)	
Nazca	911	Pacific	0 - 22.34^	Tebbens and Cande (1997), Wright et al. (2016)	
Caribbean	2007	North America	0 - 38^	Leroy et al. (2000), Boschman et al. (2014)	Relative motion of Caribbean plate to Southern Cuba (North America) constrained by Cayman Trough anomalies

Table 1. Overview of the global plate circuit used to transfer paleomagnetic data to a single reference plate. See Fig. 3 for a graphical overview. Full rotation parameters, chrons and references per Euler rotation pole are listed in Table S1. * = fit in Pangea same as in Torsvik et al. (2012), ^ = maximum age to which plate is connected to South Africa (701) in plate circuit.

name	min_age	max_age	age	slat	slon	N	K	A95	plat	plon	plateID	Rlat	Rlon	lithology	f	p_std	authors	refno	DB
Prado section, Teruel, Spain	9.1	10.3	9.7	40.3	-1.1	246	16.5	2.3	-84.4	341.0	304	-84.3	350.9	sedimentary	0.5	6.5	Abels et al. (2009)		T12
Cascante, Spain	9.4	10.6	10.0	40.2	-1.1	81	15.4	4.1	-79.0	293.9	304	-79.7	297.9	sedimentary	0.9	4.34	Abdul Aziz et al. (2004)		T12
Jesus Maria and Atotonilco lavas	9.2	11.9	10.6	20.6	257.0	29	39.7	4.3	-80.7	292.3	101	-81.0	293.5	igneous			Goguitchaichvili et al. (2011)		this study
Volcanics, Jebel Soda, Libya	10.0	13.0	11.5	28.7	15.6	12	35.4	7.4	-78.4	16.1	715	-78.4	16.1	igneous			Schult and Soffel (1973)	50	T12
Volcanics, Jebel Soda, Libya	10.0	13.0	11.5	28.8	15.5	9	47.0	6.8	-69.0	4.0	715	-69.0	4.0	igneous			Ade-Hall et al. (1975)	60	T12
East African volcanics, Kenya and Tanzania	11.0	13.0	12.0	0.0	36.0	22	28.8	6.1	-86.5	6.6	709	-86.5	12.1	igneous			Reilly et al. (1976)	774	T12
Taatsyn Gol 3, Mongolia	12.1	13.3	12.7	45.5	101	7	14.5	16.4	-71.6	358.0	301	-71.2	1.8	igneous			Hankard et al. (2007a)		this study
Ethiopian traps, Debre Sina	10.6	14.9	12.8	9.9	39.8	30	27.7	5.1	-83.8	26.9	715	-83.8	26.9	igneous			Lhuillier & Gilder (2018)		this study
Miocene volcanics, Canary Islands	5.0	21.0	13.0	28.0	344.0	99	16.0	3.5	-81.9	294.4	714	-81.9	294.4	igneous			Watkins (1973)	25	T12
Volcanics, Kenya	12.0	15.0	13.5	-1.6	35.9	14	20.8	8.9	-80.1	214.3	709	-80.3	211.7	igneous			Patel and Raja (1979)	1517	T12
Padre Miguel Ignimbrite Suite, Honduras	14.3	16.3	15.3	14.4	272.9	33	24.5	5.2	-80.0	322.9	2007	-80.4	329.7	igneous			Molina-Garza et al. (2012)		this study
Hongshiya	14.0	18.0	16.0	36.2	118.5	9	57.8	6.8	-84.3	53.5	601	-82.7	58.1	igneous			Zhao et al. (1994)		this study
Leucitite	15.0	17.2	16.1	-32.84	146.45	17	20.5	8.6	-80.2	95.4	801	-82.8	33.6	igneous			Hansma and Tohver (2018)		this study
Trosky volcano, Czech Republic	15.7	17.3	16.5	50.52	15.23	11	21.5	10.1	-76.9	261.1	301	-78.6	263.0	igneous			Petronis et al. (2015)		this study
Hannuoba	15.0	24.0	19.5	40.2	112.7	16	36.3	6.2	-83.7	52.3	601	-81.5	57.7	igneous			Pan et al. (2005)		this study
Ust-Bokson, Mongolia	19.5	20.3	19.9	52.1	100.3	9	32.1	9.2	-69.8	6.5	301	-68.7	12.6	igneous			Hankard et al. (2007a)		this study
Jantetelco granodiorites & Tepexco volcanics	18.8	22.8	20.8	18.7	261.3	26	17.4	7.0	-78.4	4.28	101	-78.7	15.2	igneous			Duarte et al. (2015)		this study
Stoddard Mountain laccolith	20.0	22.0	21.0	37.6	246.6	19	54.3	4.6	-82.9	346.2	101	-83.5	359.7	igneous			Petronis et al. (2004)		T12
Suhindol volcanics	19.4	23.5	21.5	43.23	25.15	11	25.2	9.3	-84.1	242.1	301	-86.5	236.7	igneous			van Hinsbergen et al. (2008a)		this study
Dinan Bay lavas	18.9	24.4	21.7	53.7	227.3	13	19.0	9.8	-82.7	301.7	101	-83.8	309.1	igneous			Irving et al. (2000)		T12
Younger plutons	22.0	23.0	22.5	36.6	254.5	11	34.8	7.8	-87.1	189.5	101	-86.6	176.2	igneous			Hagstrum and Johnson (1986)	1402	T12
Pingzhuang	22.0	23.0	22.5	42.0	119.2	17	49.9	5.1	-88.0	300.0	601	-88.0	22.1	igneous			Shi et al. (2002)		this study
Lake City Caldera	22.0	24.0	23.0	38.0	252.7	17	9.2	12.4	-76.4	30.3	101	-76.2	41.5	igneous			Reynolds et al. (1986)	1300	T12
Main Range Volcano and Tweed Volcano	20.2	26.7	23.5	-28.20	153.00	56	22.5	4.1	-74.2	74.8	801	-74.4	24.2	igneous			Wellman (1975)		this study
Latir volcanics	21.0	26.0	23.5	36.8	254.6	43	14.2	6.0	-80.9	331.2	101	-81.9	342.8	igneous			Hagstrum and Lipman (1986)	1299	T12
Volcanics Germany	18.0	30.0	24.0	50.8	8.0	40	15.4	6.0	-77.8	310.8	301	-78.9	323.9	igneous			Schreiber and Rotsch (1998)	3282	T12
Zhangjiakou	17.0	33.0	25.0	41.1	114.7	8	9.0	19.5	-84.4	223.2	601	-86.6	201.3	igneous			Zheng (1991)		this study
Conejos and Hinsdale Formation	23.0	29.0	26.0	37.2	254.4	23	15.2	8.0	-79.7	342.6	101	-80.5	356.4	igneous			Brown and Golombek (1997)	3130	T12
Kerguelen islands (Antarctic Plate)	24.0	30.0	27.0	-49.3	69.5	233	16.5	2.3	-85.5	9.3	802	-81.9	33.3	igneous			Camps et al. (2007)		T12
Springsure Volcano	27.3	28.9	28.1	-24.10	148.10	18	13.7	9.7	-70.5	120.6	801	-82.4	70.6	igneous			Hansma and Tohver (2019)		this study
Ignimbrita Panalillo Superior	24.8	31.3	28.1	22.0	259.0	41	27.4	3.6	-68.6	338.1	101	-69.5	349.6	igneous			González-Naranjo et al. (2012)		this study
Afro-Arabian flood volcanic province, Yemen	27.0	31.0	29.0	15.4	44.1	48	33.6	3.6	-74.2	69.1	503	-78.4	42.9	igneous			Riisager et al. (2005)		T12
Peak Range	28.2	31.2	29.7	-22.66	147.97	29	10.1	8.8	-64.6	111.8	801	-75.9	73.0	igneous			Hansma and Tohver (2019)		this study
Ethiopian traps, Belessa	29.2	30.5	29.9	12.4	37.7	42	44.9	3.3	-80.5	60.6	715	-80.5	60.6	igneous			Lhuillier & Gilder (2018)		this study
Lima Limo section, Ethiopian Traps	29.4	30.4	29.9	13.2	37.9	79	22.7	3.4	-78.2	33.0	715	-78.2	33.0	igneous			Ahn et al. (2021)		this study
Mongollon–Datil volcanics	24.0	36.0	30.0	33.3	252.1	61	17.6	4.5	-81.9	323.6	101	-83.1	343.5	igneous			Diehl et al. (1988)	1315	T12
Mongollon–Datil volcanics	24.0	36.0	30.0	33.3	252.2	39	21.0	5.1	-82.8	316.2	101	-84.2	336.4	igneous			McIntosh et al. (1992)	2631	T12
Ethiopian Traps, Ethiopia	29.0	31.0	30.0	12.4	38.6	53	28.9	3.7	-77.0	28.0	715	-77.0	28.0	igneous			Rochette et al. (1998)	3209	T12
Ethiopian Flood basalts, Abbay and Kessen gorges, Ethiopia	29.0	31.0	30.0	9.7	38.8	16	17.8	9.0	-83.0	13.3	715	-83.0	13.3	igneous			Kidane et al. (2002)	3496	T12
Mongolia, Jaran Plateau and Bogd Plateaus	30.2	30.4	30.3	44.8	100.7	13	25.1	8.4	-81.6	94.5	301	-77.9	88.7	igneous			Dupont-Nivet et al. (2011)		this study
Hillsborough Volcano	33.1	34.1	33.6	-20.98	149.00	14	32.2	7.1	-67.1	121.4	801	-80.6	68.8	igneous			Hansma and Tohver (2019)		this study
Liverpool Volcano	33.0	34.4	33.7	-31.70	150.20	36	25.7	4.8	-71.1	95.5	801	-74.8	28.5	igneous			Wellman (1969)		this study
Southern Plateau volcanics, Ethiopia	30.0	38.0	34.0	9.1	41.0	22	24.4	6.4	-75.1	350.3	709	-75.3	351.8	igneous			Schult (1974)	40	T12
Tecalitlan Dikes	33.2	36.8	35.0	19.3	257.0	12	30.8	8.0	-75.7	346.6	101	-76.0	7.2	igneous			Rosas-Elguera et al. (2011)		this study
Mariscal Mountain Gabbro	35.0	39.0	37.0	29.1	256.8	18	42.5	5.4	-80.0	5.3	101	-79.1	31.6	igneous			Harlan et al. (1995)	2943	T12
Ramsay Island lavas	36.0	41.0	38.5	52.5	228.7	11	41.0	7.0	-78.2	299.9	101	-80.6	322.7	igneous			Irving et al. (2000)		T12
Talerua Member lavas	38.0	40.0	39.0	70.4	305.2	13	32.7	7.4	-76.3	21.5	102	-75.0	42.0	igneous			Schmidt et al. (2005)		T12
Mongolia, Khaton Sudal	38.8	40.0	39.4	44.5	101.3	7	45.1	9.1	-76.7	60.1	301	-70.5	65.6	igneous			Dupont-Nivet et al. (2011)		this study
Khaton Sudal, Mongolia	38.8	40.0	39.4	44.5	101.4	8	61.5	7.1	-71.9	22.6	301	-67.0	36.6	igneous			Hankard et al. (2007a)		this study
Beaver River alkalic complex	41.5	42.5	42.0	60.3	234.7	21	39.8	5.1	-79.2	325.8	101	-80.2	358.0	igneous			Symons et al. (2003)		T12
Monterey intrusives	42.0	47.0	44.5	38.4	280.6	11	12.3	13.6	-85.5	63.7	101	-81.7	84.7	igneous			Ressetar and Martin (1980)	1865	T12
Rattlesnake Hills volcanics	42.0	50.0	46.0	42.3	248.1	18	13.9	9.6	-79.4	326.2	101	-80.2	3.0	igneous			Sheriff and Shive (1980)	1712	T12
Bitterroot Dome dike swarm	44.0	51.0	47.0	46.4	245.2	11	34.9	7.8	-72.0	341.6	101	-72.0	9.0	igneous			Doughty and Sheriff (1992)	2560	T12
Eocene volcanics Patagonia	42.0	56.0	49.0	-42.6	290.0	36	18.0	5.7	-81.0	337.4	291	-74.2	34.1	igneous			Somoza (2007)		T12
Robinson Anticline intrusives	48.0	52.0	50.0	46.2	248.5	16	26.6	7.3	-77.1	325.8	101	-78.1	359.0	igneous			Harlan et al. (1988)	1348	T12

Absorako volcanics	45.0	55.0	50.0	44.5	249.8	42	13.5	6.2	-83.1	326.3	101	-83.5	15.9	igneous	Harlan and Morgan (2010)		T12
Combined Eocene intrusives	47.0	54.0	50.5	47.9	249.9	94	18.6	3.5	-82.7	347.2	101	-81.8	31.4	igneous	Diehl et al. (1983)	1270	T12
Ezcurra Inlet & Point Hennequin groups	47.8	56.0	51.9	-62.1	301.7	22	16.7	7.8	-79.0	48.0	803	-69.6	50.0	igneous	Watts et al. (1984)		this study
Barrington Volcano, New South Wales	52.0	54.0	53.0	-32.0	151.4	33	23.2	5.3	-70.5	125.6	801	-79.8	21.5	igneous	Wellman et al. (1969)	592	T12
Nuussuaq lavas, Kanisut Member	53.0	55.0	54.0	70.7	305.5	20	11.1	10.3	-74.6	339.4	102	-77.6	11.0	igneous	Riisager et al. (2003b)		T12
South Shetland Islands	52.2	56.5	54.4	-62.2	301.0	15	8.0	14.4	-82.1	2.6	803	-73.4	31.2	igneous	Gao et al. (2018)		this study
Kangerdlugsuaq dykes, Irminger	53.0	54.0	54.5	68.2	329.0	11	31.8	8.2	-62.9	0.4	102	-64.4	25.3	igneous	Faller and Soper (1979)	1604	T12
Skaergaard Intrusion	55.0	56.0	55.5	68.2	328.3	30	25.1	5.4	-61.0	345.0	102	-63.7	9.1	igneous	Schwarz et al. (1979)	1432	T12
Khuts Uul, Mongolia	56.3	57.9	57.1	43.2	104.6	14	34.9	6.8	-69.6	328	301	-69.2	358.8	igneous	Hankard et al. (2008)		this study
Svartenhuk lavas	54.0	61.5	57.8	71.4	305.5	30	9.3	9.1	-62.0	349.7	102	-64.2	16.0	igneous	Chauvet et al. (2019)		this study
Jacobsen Fjord dykes	53.0	60.0	59.0	68.2	329.0	22	33.3	5.5	-67.7	357.7	102	-69.2	27.7	igneous	Faller and Soper (1979)	1604	T12
East Gilf Kebir Plateau basalts	57.3	60.7	59.0	23.3	27.3	13	80.0	4.7	-71.7	23.5	715	-71.7	23.5	igneous	Lotfy and Odah (2015)		this study
Arran dikes, Scotland	58.8	60.0	59.4	55.6	354.8	413	17.8	1.7	-81.7	359.8	301	-75.1	42.8	igneous	Dagley et al. (1978)	1041	T12
Jacobsen Fjord basalts	59.0	60.0	59.5	68.2	329.0	39	11.1	7.2	-56.0	3.0	102	-57.3	27.7	igneous	Faller and Soper (1979)	1604	T12
Arran intrusives and extrusives	58.0	61.0	59.5	55.5	354.8	165	27.4	2.1	-80.2	339.6	301	-76.1	29.4	igneous	Hodgson et al. (1990)	3433	T12
Ardnamurchan complex, Scotland	59.6	60.4	60.0	56.7	353.8	62	23.8	3.8	-77.0	355.0	301	-71.7	31.3	igneous	Dagley et al. (1984)	1377	T12
Faeroe flood volcanics	59.5	60.7	60.1	61.9	353.1	43	14.2	6.0	-71.4	334.7	301	-69.6	8.4	igneous	Riisager et al. (2002)	3494	T12
Svartenhuk lavas, Vaigat Formation	60.0	61.0	60.5	71.6	305.9	10	25.1	9.8	-76.2	37.9	102	-73.7	73.2	igneous	Riisager et al. (2003b)		T12
Nuusuaq and Disko lavas, Vaigat Formation	60.0	61.0	60.5	70.3	305.1	14	19.8	9.2	-64.8	321.5	102	-69.4	345.5	igneous	Riisager et al. (2003a)		T12
Rhum and Canna igneous, Scotland	59.7	61.7	60.7	57.0	353.5	107	15.7	3.6	-81.0	359.0	301	-74.5	41.5	igneous	Dagley and Mussett (1981)	1169	T12
Mull lavas, Scotland	59.7	62.0	60.9	56.3	353.9	26	23.3	6.0	-73.3	346.2	301	-69.5	20.2	igneous	Ganerød et al. (2008)		T12
Torris, Snow, Half Moon, King George, Admirality lavas and intrusions	56.0	66.0	61.0	-62.4	300.3	10	19.8	11.1	-82.7	355.2	803	-73.4	28.0	igneous	Poblete et al. (2011)		this study
Antrim Lava, Ireland	59.6	62.6	61.1	54.9	353.9	37	15.0	6.3	-78.9	347.0	301	-74.1	30.8	igneous	Ganerød et al. (2010)		T12
Muck and Eigg igneous	60.9	61.4	61.2	56.9	353.8	133	13.0	3.5	-74.0	351.0	301	-69.5	24.7	igneous	Dagley and Mussett (1986)	1204	T12
Sumber Uul - Tulga, Mongolia	56.2	68.0	62.1	43	104	14	85.0	4.3	-85.2	272.5	301	-84.0	56.5	igneous	Hankard et al. (2008)		this study
Combined Palaeocene intrusions	59.0	67.0	63.0	47.6	251.1	36	20.2	5.4	-81.8	1.4	101	-81.1	38.4	igneous	Diehl et al. (1983)	1270	T12
Mount Pavagarh Traps, Gujrat, India	60.0	68.0	64.0	22.5	73.5	16	52.5	5.1	-39.2	105.6	501	-71.6	63.1	igneous	Verma and Mital (1974)	94	T12
Deccan Traps, Mahabaleshwar, India	64.0	67.0	65.5	17.9	73.6	28	12.8	7.4	-40.0	96.0	501	-69.2	43.4	igneous	Kono et al. (1972)	107	T12
Deccan Traps, Nagpur to Bombay traverse, India	64.0	67.0	65.5	20.0	75.0	16	37.9	6.1	-38.4	102.4	501	-71.3	57.6	igneous	Vandamme et al. (1991)	393	T12
Deccan dyke swarms, western India	64.0	67.0	65.5	21.5	74.3	11	23.0	9.7	-37.2	99.5	501	-68.9	54.3	igneous	Prasad et al. (1996)	3094	T12
Khumbarli Ghat, Mahabeleshwar Plateau, India	64.0	67.0	65.5	17.4	73.7	15	24.6	7.9	-44.7	107.8	501	-78.7	54.2	igneous	Jay et al. (2009)		T12
Varandah Ghat, Mahabeleshwar Plateau, India	64.0	67.0	65.5	18.1	73.6	15	28.8	7.2	-33.5	106.7	501	-68.7	73.6	igneous	Jay et al. (2009)		T12
Wai-Panchgani, Mahabeleshwar Plateau, India	64.0	67.0	65.5	17.9	73.8	16	14.7	10.0	-36.8	85.9	501	-61.3	35.7	igneous	Jay et al. (2009)		T12
Kelgar, Mahabeleshwar Plateau, India	64.0	67.0	65.5	17.9	73.7	16	21.2	8.2	-42.3	96.6	501	-71.1	39.3	igneous	Jay et al. (2009)		T12
Tapola, Mahabeleshwar Plateau, India	64.0	67.0	65.5	17.8	73.7	17	17.1	8.9	-38.2	95.5	501	-67.7	46.0	igneous	Jay et al. (2009)		T12
Matheran Ghat, Mahabeleshwar Plateau, India	64.0	67.0	65.5	19.0	73.3	17	36.0	6.0	-36.6	108.4	501	-72.1	73.6	igneous	Jay et al. (2009)		T12
Ambenali Ghat, Mahabeleshwar Plateau, India	64.0	67.0	65.5	17.9	73.6	34	16.8	6.2	-38.8	104.5	501	-72.5	61.2	igneous	Jay et al. (2009)		T12
Nandurbar-Dhule dykes, India	63.0	68.4	65.7	21.3	74.3	13	13.5	11.7	-40.5	104.5	501	-74.2	57.7	igneous	Das et al. (2021)		this study
Western Ghats, Deccan Traps, India	64.0	68.5	66.3	19.0	73.5	50	28.7	3.8	-37.8	102.6	501	-71.7	57.9	igneous	Chenet et al. (2009)		this study
Late Cretaceous mafic dikes in Kerala	65.0	70.0	67.5	10.2	76.1	10	56.8	6.5	-37.7	107.0	501	-74.8	66.1	igneous	Radhakrishna et al.(2012)		this study
Central Kerala dykes, India	68.0	70.0	69.0	9.7	76.7	6	33.4	11.8	-34.6	94.0	501	-67.1	42.7	igneous	Radhakrishna et al. (1994)	2754	T12
Itatiaia and Passa Quatro Complexes, Brazil	67.0	74.0	70.5	-22.4	315.2	18	37.8	5.7	-79.5	0.0	201	-69.6	46.7	igneous	Montes-Lauar et al. (1995)	3261	T12
Patagonian Plateau basalts, Chile, Argentina	64.0	79.0	71.5	-45.3	288.7	18	31.6	6.3	-78.7	358.4	291	-68.8	45.4	igneous	Butler et al. (1991)	2374	T12
Lisbon Basalts 1969, Portugal	70.0	74.0	72.0	38.83	-9.18	5	72.3	9.1	-73.7	19.6	304	-69.3	35.6	igneous	van der Voo (1969)		this study
Monchique Syenite I	70.0	74.0	72.0	37.06	-8.82	8	104.9	5.4	-73.5	344.6	304	-71.9	7.0	igneous	van der Voo (1969)		this study
Monchique Syenite II	70.0	74.0	72.0	37.06	-8.82	27	47.8	4.1	-77.1	347.1	304	-75.1	13.9	igneous	Storetvedt et al. (1990)		this study
Adel Mountain volcanics	71.0	81.0	76.0	47.5	248.1	26	16.7	7.2	-83.4	20.9	101	-80.0	61.7	igneous	Gunderson and Sheriff (1991)	2370	T12
Minusa trough intrusions, Siberia	74.0	79.0	76.5	55.0	99.2	16	37.5	6.1	-82.8	8.5	301	-73.3	55.1	igneous	Metelkin et al. (2007)		this study
Doherty Mountain sills	76.5	77.5	77.0	45.9	248.1	5	33.6	13.4	-80.8	358.1	101	-78.2	42.6	igneous	Harlan et al. (2008)		T12
Elkhorn Mountains	77.0	83.0	80.0	46.1	248.0	15	16.8	9.6	-80.3	9.5	101	-76.2	52.7	igneous	Diehl (1991)	2382	T12
Maudlow Formation welded tuffs	75.0	85.0	80.0	46.1	248.9	11	22.7	9.8	-69.8	27.8	101	-65.1	60.3	igneous	Swenson and McWilliams (1989)	2397	T12
Sao Sabastiao Island Intrusions, Brazil	78.0	84.0	81.0	-23.8	314.7	18	50.7	4.9	-79.4	331.9	201	-69.4	40.5	igneous	Montes-Lauar et al. (1995)	3261	T12
Pocos de Caldas Alkaline Complex, Brazil	78.0	90.0	84.0	-21.8	313.5	47	60.3	2.7	-83.2	320.1	201	-71.9	48.5	igneous	Montes-Lauar et al. (1995)	3261	T12
Volcanics, Massif d'Androy Andria	84.0	90.0	87.0	-24.2	46.0	6	36.0	11.3	-64.0	63.0	702	-63.5	63.1	igneous	Andriamirado and Roche (1969)	547	T12
Volcanics, Mailaka Andria	84.0	90.0	87.0	-18.0	44.4	10	35.2	8.3	-70.3	63.1	702	-69.8	63.4	igneous	Andriamirado (1971)	708	T12
Volcanics, Mangoky–Anilahy Andria	84.0	90.0	87.0	-22.8	44.3	11	21.8	10.0	-73.7	73.1	702	-73.2	73.3	igneous	Andriamirado (1971)	708	T12
Volcanics, Antanimena Andria	84.0	90.0	87.0	-16.4	46.0	12	48.7	6.3	-66.1	49.7	702	-65.7	50.1	igneous	Andriamirado (1971)	708	T12
Volcanics, Southeast Coast Andria	84.0	90.0	87.0	-21.8	48.0	14	42.1	6.2	-65.8	35.6	702	-65.5	36.2	igneous	Andriamirado (1971)	708	T12
Volcanics, Southwest Madagascar	84.0	90.0	87.0	-23.2	44.3	41	68.1	2.7	-76.8	68.2	702	-76.3	68.8	igneous	Torsvik et al. (1998)	3210	T12
Dolerites, east Madagascar	84.0	90.0	87.0	-18.0	47.0	16	38.8	6.0	-65.5	38.0	702	-65.2	38.5	igneous	Storetvedt et al. (1992)	3211	T12
Late Cretaceous mafic dikes in Kerala	85.0	90.0	87.5	10.2	76.1	6	42.1	10.4	-26.8	113.1	501	-72.7	67.6	igneous	Radhakrishna et al.(2012)		this study

Yongtai	87.9	88.6	88.3	25.7	119.0	19	76.5	3.9	-83.1	332.6	602	-73.4	62.3	igneous			Huang et al. (2012)		this study
St. Mary Islands, western India	91.0	91.4	91.2	13.4	74.7	7	42.1	9.4	-14.2	117.8	501	-61.8	84.2	igneous			Torsvik et al. (2000)		T12
d'Analava complex	91.3	91.9	91.6	-14.5	50.1	5	41.6	12.0	-66.7	43.5	702	-66.4	44.0	igneous			Meert and Tamrat (2006)		T12
Amma Fatma section, Morocco	89.4	93.9	91.7	28.2	348.2	88	38.7	2.5	-64.3	76.3	707	-65.0	75.1	sedimentary	0.70	4.0	Ruiz-Martinez et al. (2011)		this study
Wadi Natash volcanics, Egypt	86.0	100.0	93.0	24.4	34.3	15	44.4	5.8	-69.3	78.1	715	-69.4	78.3	igneous			Schult et al. (1981)	1500	T12
Khurmun Uul - Shovon basalts, Mongolia	90.8	96.0	93.4	44.2	103.4	23	22.2	6.6	-84.7	15.0	301	-66.5	73.5	igneous			Hankard et al. (2007b)		this study
Mount Dromedary Intrusion	92.0	96.0	94.0	-36.30	150.70	22	11.5	9.5	-55.9	138.6	801	-68.6	76.4	igneous			Robertson (1963)		this study
Axel Heiberg lavas	93.2	97.2	95.2	79.4	267.6	36	15.0	6.4	-70.4	17.0	101	-58.9	64.9	igneous			Tarduno et al. (2002)		this study
Magnet Cove and other intrusions	98.0	102.0	100.0	34.3	267.5	20	34.0	5.7	-74.1	12.5	101	-61.5	68.3	igneous			Globerman and Irving (1988)	1322	T12
Cuttingsville	99.7	100.3	100.0	43.5	287.1	5	50.2	10.9	-72.1	17.0	101	-59.2	69.7	igneous			McEnroe (1996)	3087	T12
Tsost Magmatic Field, Mongolia	94.7	107.0	100.9	44.3	102.2	7	19.2	14.1	-82.1	324.9	301	-68.1	68.4	igneous			van Hinsbergen et al. (2008b)		this study
Little Rattlesnake Complex	108.0	114.0	111.0	43.0	288.9	12	71.2	5.2	-71.5	2.6	101	-56.6	69.3	igneous			McEnroe (1996)	3087	T12
Pleasant Mountain	111.7	112.5	112.1	44.0	289.2	5	88.5	8.2	-77.4	5.0	101	-61.3	75.8	igneous			McEnroe (1996)	3087	T12
Suhongtu	110.6	114.1	112.4	41.2	104.1	31	64.4	3.2	-80.3	20.3	601	-56.4	81.4	igneous			Ren et al. (2004); Zhu et al. (2008)		this study
Burnt Meadow Mountains	112.4	112.8	112.6	43.9	289.1	10	51.9	6.8	-75.7	28.5	101	-57.7	85.1	igneous			McEnroe (1996)	3087	T12
Cretaceous Lamproites	109.1	116.6	112.9	23.8	87.0	11	30.5	8.4	-14.9	107.6	501	-58.8	62.7	igneous			Radhakrishna et al. (2017)		this study
Rajmahal Traps, West Bengal and Bihar, India	115.0	117.0	116.0	24.8	87.7	16	91.0	6.0	-3.2	117.5	501	-51.3	86.6	igneous			McDougall and McElhinny (1970)	633	T12
Rajmahal Traps, Bihar, India	115.0	117.0	116.0	24.6	87.7	25	29.8	5.4	-7.0	117.0	501	-54.9	84.3	igneous			Klootwijk (1971)	678	T12
Rajmahal Traps, West Bengal, India	115.0	117.0	116.0	25.0	87.4	19	10.6	10.8	-9.3	124.8	501	-58.5	97.5	igneous			Das et al. (1996)	2977	T12
Rajamahal Traps, North Rajmahal Hills, India	115.0	117.0	116.0	24.7	87.5	8	52.8	7.7	-6.5	120.2	501	-55.1	89.9	igneous			Tarduno et al. (2001)		T12
Hongyan	114.0	118.0	116.0	36.9	121.2	11	27.3	8.9	-86.5	341.1	601	-61.9	88.1	igneous			Charles et al. (2012)		this study
Rajmahal Traps, Bihar, India	116.0	118.0	117.0	24.7	87.7	34	53.7	3.4	-9.4	116.6	501	-57.0	82.5	igneous			Rao and Rao (1996)	3095	T12
South-East Artz Bogd, Mongolia	115.4	119.3	117.4	44.4	102.5	24	38.1	4.9	-75.6	312.3	301	-64.8	64.2	igneous			van Hinsbergen et al. (2008b)		this study
Weideshan	116.0	120.0	118.0	37.2	122.4	9	33.7	9.0	-80.1	0.1	601	-56.7	79.1	igneous			Charles et al. (2011)		this study
Jianchang	117.0	121.0	119.0	40.9	119.8	5	31.5	7.6	-81.1	44.2	601	-52.9	90.3	igneous			Qin et al., 2008		this study
Alfred Complex	118.0	122.0	120.0	43.5	289.3	14	64.1	5.0	-74.0	29.8	101	-53.5	87.8	igneous			McEnroe (1996b)	3036	T12
Cape Neddick	120.2	121.0	120.6	43.2	291.4	12	67.5	5.3	-74.8	354.8	101	-57.1	73.3	igneous			McEnroe (1996b)	3036	T12
Vulcanitas Cerro Colorado Formation, Cordoba, Argentina	115.0	127.0	121.0	-32.0	-64.0	6	27.5	13.0	-81.0	14.0	202	-49.6	71.3	igneous			Valencio (1972)	123	T12
South-East ih Bogd, Mongolia	118.2	124.3	121.3	44.8	100.7	21	34.3	5.7	-83.7	16.4	301	-56.0	88.2	igneous			van Hinsbergen et al. (2008b)		this study
Tatnic Complex	120.0	124.0	122.0	43.3	289.3	10	65.2	6.0	-65.9	27.8	101	-44.8	86.0	igneous			McEnroe (1996b)	3036	T12
Florianopolis dyke swarm, Santa Catarina Island, Brazil	119.0	128.3	123.7	-27.7	311.5	65	47.3	2.6	-89.1	3.3	201	-56.5	76.0	igneous			Raposo et al. (1998)	3190	T12
South-East Baga Bogd, Mongolia	122.7	124.7	123.7	44.8	101.9	29	18.8	6.3	-79.9	339.9	301	-57.9	79.0	igneous			van Hinsbergen et al. (2008b)		this study
El Salto–Almafuerte lavas, Cordoba, Argentina	119.0	129.0	124.0	-32.2	-64.2	15	39.4	6.2	-72.0	25.0	202	-39.3	73.3	igneous			Mendia (1978)	1087	T12
Lebanon diorite	122.0	128.0	125.0	43.4	289.2	5	70.9	9.1	-71.0	16.9	101	-50.1	83.5	igneous			McEnroe (1996b)	3036	T12
Notre Dame Bay dikes	122.0	136.0	129.0	49.5	304.6	10	99.5	4.9	-67.2	30.8	101	-44.6	91.6	igneous			Lapointe (1979)	1854	T12
Ponta Grossa dykes, Brazil	129.2	131.4	130.3	-24.5	310.0	115	43.8	2.0	-82.4	30.3	201	-47.0	77.7	igneous			Raposo and Ernesto (1995)	2958	T12
Ponta Grossa dykes	129.2	131.4	130.3	-23.8	310.0	24	35.7	5.0	-88.1	222.0	201	-56.2	78.0	igneous			Cervantes-Solano et al. (2015)		this study
Serra Geral basalts, Brazil	131.0	135.0	133.0	-29.0	310.0	37	40.4	3.7	-84.6	115.4	202	-52.0	86.8	igneous			Pacca and Hiodo (1976)	765	T12
Kaoko lavas, Namibia	131.0	136.0	133.5	-20.0	14	40	59.3	3.0	-48.3	86.6	701	-48.3	86.6	igneous			Gidskehaug et al. (1975)	126	T12
Etendeka, Namibia	131.0	136.0	133.5	-20.0	14.1	21	26.1	6.3	-47.5	88.9	701	-47.5	88.9	igneous			Owen-Smith et al. (2019)		this study
Etendeka LIP (upper), Namibia	131.0	136.0	133.5	-19.9	14.1	33	30.3	4.6	-47.2	84.2	701	-47.2	84.2	igneous			Dodd et al. (2015)		this study
Etendeka LIP (lower), Namibia	131.0	136.0	133.5	-21.3	14.2	37	26.2	4.7	-52.3	91.7	701	-52.3	91.7	igneous			Dodd et al. (2015)		this study
Parana flood basalt, Alto Paraguay Formation, Paraguay	132.0	136.0	134.0	-25.6	-54.9	18	65.0	4.3	-86.2	359.2	201	-52.3	75.6	igneous			Goguitchaichvili et al. (2013)		this study
Posadas Formation, Parana flood basalts	132.0	136.0	134.0	-26.4	-54.3	26	45.6	4.2	-89.7	339.1	201	-55.3	78.8	igneous			Mena et al. (2010)		this study
Arapey volcanics, Uruguay	132.0	136.0	134.0	-31.0	303.0	29	42.0	4.2	-84.8	95.8	202	-50.2	85.2	igneous			Cervantes-Solano et al. (2010)		this study
Central Parana Magmatic Province	132.0	136.0	134.0	-26.0	308.0	96	34.3	2.5	-84.1	69.2	201	-50.4	84.4	igneous			Owen-Smith et al. (2019)		this study
Northern Parana Magmatic Province, Brazil	132.0	136.0	134.0	-22.0	308.0	128	48.0	1.8	-82.7	84.5	201	-50.3	87.9	igneous			Ernesto et al. (2021)		this study
Franz Josef Land LIP	125.0	145.0	135.0	80.7	56.0	40	26.2	4.5	-68.9	357.5	301	-46.3	73.4	igneous			Abashev et al. (2018)		this study
Southwest Greenland dykes	144.2	151.0	147.6	62.3	310.2	40	25.1	4.6	-69.3	5.0	102	-50.9	85.9	igneous			Kulakov et al. (2021)		this study
La Negra south	151.2	154.4	152.8	-22.2	289.8	18	11.2	10.8	-84.5	76.4	290	-48.0	84.1	igneous			Fu et al. (2020)		this study
Posades and Sierra Colorado ignimbrites, Argentina	153.0	157.0	155.0	-47.4	-71.8	16	24.5	7.6	-81.0	172.0	291	-57.9	90.4	igneous			Iglesia-Llanos et al. (2003)	3535	T12
Chon Aike Formation, Argentina	151.5	158.5	155.0	-47.2	-69.0	23	13.3	8.6	-84.3	191.3	291	-56.9	83.0	igneous			Ruiz González et al. (2019)		this study
La Mathilde Formation, Patagonia	156.7	158.1	157.4	-47.8	291.2	10	13.6	13.6	-84.1	179.2	291	-56.4	85.1	igneous			Ruiz Gonzalez et al. (2022)		this study
Nico Perez dykes, Uruguay	154.6	160.6	157.6	-33.3	-55.6	8	30.0	10.2	-87.0	197.3	202	-55.7	79.8	igneous			Lossada et al. (2014)		this study
Zapican dike swarm, Uruguay	154.6	160.6	157.6	-33.5	-55.0	19	22.7	7.2	-86.4	178.9	202	-58.2	83.4	igneous			Cervantes-Solano et al. (2020)		this study
Intrusive rocks, Nigeria	150.0	170.0	160.0	9.0	8.6	6	27.8	13.0	-62.5	61.6	714	-61.3	65.8	igneous			Marton and Marton (1976)	1081	T12
La Negra north	162.2	169.4	165.8	-22.2	289.8	28	13.8	7.6	-84.3	180.9	290	-56.8	84.4	igneous			Fu et al. (2020)		this study
Chon Aike Formation, Patagonia	166.0	170.0	168.0	-48.0	292.6	13	10.3	13.5	-81.2	207.7	291	-59.7	81.4	igneous			Vizan (1998)		this study
Gingenbullen Dolerite	167.0	177.0	172.0	-34.5	150.3	7	9.2	21.0	-52.0	153.0	801	-46.3	66.2	igneous			Thomas et al. (2000)		this study
West Maranhao Basalts, Brazil	173.0	177.0	175.0	-6.4	-47.4	15	31.8	6.9	-85.3	262.5	201	-58.5	72.7	igneous			Schult and Guerreiro (1979)	1431	T12
Garrawilla volcanics and Nombi extrusives	177.0	183.0	180.0	-31.0	150.0	14	16.8	10.0	-46.1	175.2	801	-59.7	77.2	igneous			Schmidt (1976)	780	T12

Batoka basalts, northern Zimbabwe	177.5	183.3	180.4	-17.9	26.2	5	27.4	14.9	-63.9	80.6	701	-63.9	80.6	igneous			Jones et al. (2001)		T12
Northern Victoria Land - Kirkpatrick Basalts	179.5	182.5	181.0	-71.8	162.0	8	28.0	9.3	-72.0	236.0	802	-51.3	54.0	igneous			Rolf & Henjes-Kunst (2003)		this study
Gair Mesa, Kirkpatrick basalts	179.5	182.5	181.0	-73.3	162.9	22	22.9	7.0	-66.4	222.7	802	-55.2	64.3	igneous			Lemna et al. (2016)		this study
Marifil Complex, Patagonia	177.0	185.0	181.0	-44.8	-65.7	25	12.2	8.7	-80.5	203.5	291	-58.9	83.4	igneous			Vizan (1998)		this study
Naude's Nek section, Karoo LIP	180.1	182.8	181.5	-30.76	28.04	15	30.8	7.0	-76.0	88.8	701	-76.0	88.8	igneous			Moulin et al. (2011)		this study
Oxbow-Moteng Pass section, Karoo LIP	180.1	182.8	181.5	-28.8	28.7	29	27.9	5.2	-65.3	87.9	701	-65.3	87.9	igneous			Moulin et al. (2017)		this study
Karroo dolerites combined, South Africa, Zimbabwe	179.0	187.0	183.0	-24.0	31.0	10	16.4	12.3	-65.4	75.1	701	-65.4	75.1	igneous			McElhinny and Jones (1965)	317	T12
Karroo lavas, Central Africa, Zimbabwe, Mozambique	179.0	187.0	183.0	-18.0	30.0	9	42.4	8.0	-57.0	84.0	701	-57.0	84.0	igneous			McElhinny et al. (1968)	635	T12
Tasmanian dolerite	179.0	187.0	183.0	-42.0	147.5	21	38.3	5.2	-50.7	174.5	801	-59.0	68.2	igneous			Schmidt and McDougall (1977)	1113	T12
Ferrar dolerites, Northern Prince Albert Mountains	179.0	187.0	183.0	-74.5	342.0	15	59.5	5.5	-47.8	225.5	802	-71.4	85.7	igneous			Lanza and Zanella (1993)	2721	T12
Stormberg lavas (Lesotho basalts), South Africa	179.0	187.0	183.0	-29.3	28.6	47	32.6	3.7	-71.6	93.5	701	-71.6	93.5	igneous			Kosterov and Perrin (1996)	3090	T12
Marifil Formation, North Patagonia, Argentina	178.0	188.0	183.0	-44.8	-65.6	10	19.2	11.3	-83.0	138.0	290	-53.3	90.1	igneous			Iglesia-Llanos et al. (2003)	3535	T12
Lesotho basalts	179.0	187.0	183.0	-29.4	27.8	15	15.2	10.1	-63.7	88.5	701	-63.7	88.5	igneous			Prevot et al. (2003)		this study
Scania basalts	178.0	191.0	184.5	55.5	14.0	21	16.4	8.1	-69.0	283.0	301	-63.2	84.8	igneous			Bylund and Halvorsen (1993)	2720	T12
Diabase dykes and sills, Liberia	183.5	188.1	185.8	6.5	349.5	25	31.0	5.3	-68.5	62.4	714	-67.3	67.4	igneous			Dalrympie et al. (1975)	140	T12
Marangudzi Ring Complex, Zimbabwe	183.0	189.0	186.0	-22.1	30.7	8	47.5	8.1	-70.7	106.7	701	-70.7	106.7	igneous			Brock (1968)	470	T12
Combined dikes	189.0	193.0	191.0	46.8	294.0	8	36.4	9.3	-74.9	256.0	101	-67.6	87.8	igneous			Hodych and Hayatsu (1988)	1932	T12
Kerforne dykes, France	190.0	196.0	193.0	48.3	355.5	7	36.0	10.2	-61.3	258.8	301	-75.4	87.8	igneous			Sichler and Perrin (1993)	2743	T12
Freetown Complex, Sierra Leone	190.0	196.0	193.0	8.3	346.8	13	55.8	5.6	-82.9	32.7	714	-82.4	48.7	igneous			Hargraves et al. (1999)	3287	T12
Piedmont dikes	190.0	198.0	194.0	34.5	278.5	20	24.5	6.8	-67.9	275.3	101	-63.0	68.7	igneous			Dooley and Smith (1982)	1796	T12
French Guyana dikes, Brazil	190.3	200.3	195.3	3.5	307.5	26	50.7	4.0	-81.2	235.1	201	-63.6	72.7	igneous			Nomade et al. (2000)	3378	T12
Cassipore dykes, Brazil	192.7	202.0	197.4	2.5	308.5	17	48.0	5.2	-79.8	208.6	201	-65.5	82.3	igneous			Ernesto et al. (2003)		this study
Roraima dykes, CAMP, Brazil	197.4	201.1	199.3	2.1	-63.3	7	84.6	6.6	-80.1	235.0	201	-64.6	71.7	igneous			Ernesto et al. (2003)		this study
Ighrem and Foum Zguid dykes, Morocco	198.0	202.0	200.0	30.2	7.5	23	55.0	4.1	-73.0	64.7	707	-72.4	68.8	igneous			Palencia-Ortas et al. (2011)		T12
North Mountain basalt	199.5	201.4	200.5	45.3	295.3	9	26.0	10.3	-66.4	251.9	101	-71.9	68.9	igneous			Hodych and Hayatsu (1988)	1932	T12
Hartford basin	199.6	202.0	200.8	42.0	287.4	315	12.9	2.3	-66.6	268.2	101	-65.4	66.7	sedimentary	0.5	1.15	Kent and Olsen (2008)		T12
Morrocan Intrusives, Morocco	199.0	203.0	201.0	32.0	352.5	27	16.7	7.0	-71.0	36.0	707	-71.0	40.3	igneous			Bardon et al. (1973)	148	T12
Central Atlantic Magmatic Province, Morocco	199.0	203.0	201.0	31.2	7.3	5	16.9	19.1	-73.0	61.3	707	-72.5	65.5	igneous			Knight et al. (2004)		T12
Argana Flows. Morocco	199.0	203.0	201.0	30.7	350.8	13	48.0	6.0	-69.2	55.5	707	-68.8	59.2	igneous			Ruiz-Martinez et al. (2012)		T12
Central Atlantic Magmatic Province, Morocco	199.0	203.0	201.0	31.4	7.5	99	31.4	2.6	-60.0	61.6	707	-59.5	64.2	igneous			Font et al. (2011)		this study
Newark Martinsville core	199.3	209.5	204.4	40.6	285.4	302	8.8	2.9	-67.8	276.1	101	-62.3	70.1	sedimentary	0.5	1.45	Kent and Tauxe (2005)		T12
Newark Westonville	205.4	208.6	207.0	40.2	285.4	246	10.6	2.9	-66.6	266.5	101	-66.0	67.2	sedimentary	0.5	1.43	Kent and Tauxe (2005)		T12
Gipsdalen and Fleming Fjord Formations	207.0	211.0	209.0	71.5	337.3	222	16.1	2.4	-52.5	279.0	102	-67.6	36.5	sedimentary	0.5	4.95	Kent and Tauxe (2005)		T12
Andesites, Ukraine	202.6	217.7	210.2	47.3	37.4	12	47.9	6.3	-50.0	286.4	301	-66.4	40.7	igneous			Yuan et al. (2011)		T12
Newark Somerset core	208.6	213.4	211.0	40.5	285.4	309	17.0	2.0	-61.7	275.3	101	-61.6	57.1	sedimentary	0.6	1.0	Kent and Tauxe (2005)		T12
Newark Rutgers core	213.0	215.0	214.0	40.5	285.6	336	31.0	1.4	-60.1	277.1	101	-60.3	54.5	sedimentary	0.7	0.7	Kent and Tauxe (2005)		T12
Newark Titusville core	215.0	219.0	217.0	40.3	285.1	308	23.2	1.7	-59.9	279.5	101	-59.2	54.9	sedimentary	0.6	0.83	Kent and Tauxe (2005)		T12
Newark Nursery core	218.5	224.0	221.0	40.3	285.2	194	17.3	2.5	-60.5	281.6	101	-58.4	56.7	sedimentary	0.4	1.23	Kent and Tauxe (2005)		T12
Dan River–Danville Basin	217.0	225.0	221.0	36.5	280.5	333	25.2	1.6	-59.0	279.6	101	-58.8	53.3	sedimentary	0.5	0.76	Kent and Tauxe (2005)		T12
Newark Princeton core	221.0	233.0	227.0	40.4	285.4	148	34.6	2.0	-54.2	286.6	101	-53.2	48.7	sedimentary	0.6	1.03	Kent and Tauxe (2005)		T12
Taimyr Sills, Siberia	227.0	229.2	228.1	74.8	100.6	11	74.7	5.3	-47.1	301.6	301	-57.8	39.2	igneous			Walderhaug et al. (2005)		T12
Gezira, Egypt	224.0	234.0	229.0	22.3	33.6	10	75.5	5.6	-54.6	46.2	715	-55.1	46.0	igneous			Lotfy & Elaal (2018)		this study
Dolerite dykes, Suriname	227.0	237.0	232.0	4.0	305.0	10	61.3	6.2	-82.0	320.0	201	-52.7	66.4	igneous			Veldkamp et al. (1971)	701	T12
Udzha, Siberian Platform	232.0	245.0	238.5	71.4	115.3	18	10.5	11.2	-60.3	332.4	301	-46.3	70.7	igneous			Veselovskiy et al. (2012)		this study
Alto Paraguay Province, Paraguay/Brazil	240.2	242.8	241.5	-21.5	-57.9	26	23.0	6.0	-78.0	319.0	201	-51.1	60.5	igneous			Ernesto et al. (2015)		this study
Brisbane Tuffs	237.0	247.1	242.1	-27.47	153.0	6	31.7	12.1	-56.5	153.1	801	-46.3	59.1	igneous			Robertson (1963)		this study
Puesto Viejo Formation Volcanics, Mendoza	235.3	254.7	245.0	-34.6	-68.3	14	30.6	7.3	-76.7	312.4	290	-48.6	58.5	igneous			Domeier et al. (2011c)		T12
Taimyr basalts, Siberia	242.5	254.5	248.5	74.9	100.5	10	12.0	14.5	-59.3	325.8	301	-49.0	67.4	igneous			Walderhaug et al. (2005)		T12
Kotuy River Siberian Traps, Siberia	248.4	251.6	250.0	73.0	102.4	5	31.0	13.9	-52.7	328.4	301	-44.8	59.6	igneous			Veselovsky et al. (2003)		T12
Siberian Traps Mean recalculated, Siberia	248.4	251.6	250.0	66.1	111.6	5	19.5	17.7	-52.8	334.4	301	-41.8	62.3	igneous			Kravchinsky et al. (2002)		T12
Siberian Traps, YG locality	250.4	252.4	251.4	64.0	115.0	9	36.2	8.7	-65.2	320.9	301	-52.9	75.3	igneous			Konstantinov et al. (2014)		this study
Siberian Traps, Nizhneudinsk-Octyabrskiy group	250.4	252.4	251.4	56.8	99.4	9	14.9	13.8	-44.5	329.1	301	-40.0	50.6	igneous			Latyshev et al. (2018)		this study
Siberian Traps, Tura lavas	250.4	252.4	251.4	56.8	99.4	12	11.5	13.4	-45.5	312.8	301	-50.2	42.9	igneous			Latyshev et al. (2018)		this study
Siberian Traps, RD locality	250.4	252.4	251.4	63.5	112.5	19	15.4	8.8	-53.0	313.5	301	-53.1	54.1	igneous			Konstantinov et al. (2014)		this study
Kulumber river intrusions, Siberia	250.4	252.4	251.4	68.9	86.4	33	13.4	7.1	-47.4	323.1	301	-45.1	50.7	igneous			Latyshev et al. (2021b)		this study
Siberian Traps, Nizhnyaya Tunguska river	250.4	252.4	251.4	64.6	94.4	35	24.5	5.0	-56.2	313.6	301	-54.1	59.2	igneous			Latyshev et al. (2018)		this study
Siberian Traps, Norilsk-Maymecha-Kotuy	250.4	252.4	251.4	70.0	90.0	49	23.2	4.3	-52.9	327.1	301	-45.6	59.3	igneous			Pavlov et al. (2019)		this study
Norils region intrusions, Siberia	251.3	252.3	251.8	69.3	88.5	31	24.7	5.3	-54.5	320.8	301	-49.7	59.0	igneous			Latyshev et al. (2021a)		this study
East European Platform, Zhukov	246.7	259.5	253.1	56.2	42.6	106	17.3	3.4	-53.2	349.5	301	-34.7	69.5	sedimentary	0.9	3.0	Fetisova et al. (2017)		this study
East European Platform, Puchezh	246.7	259.5	253.1	57.0	43.2	157	19.7	2.6	-41.0	326.3	301	-39.6	45.3	sedimentary	0.9	3.0	Fetisova et al. (2017)		this study
East European Platform, Oskii S"ezd	246.7	259.5	253.1	56.2	44.0	108	8.7	4.9	-59.6	322.1	301	-50.9	66.8	sedimentary	0.4	3.0	Fetisova et al. (2018)		this study

Araguainha impact structure, Brazil	252.2	257.2	254.7	-16.8	-53.0	28	83.5	3.6	-84.2	326.6	201	-53.0	70.2	igneous			Yokoyama et al. (2014)		this study
East European Platform, Sukhona	251.9	259.5	255.7	61.0	45.0	210	13.9	2.7	-49.2	345.9	301	-33.8	64.0	sedimentary	0.7	3.0	Fetisova et al. (2018)		this study
East European Platform, Nelben	251.9	259.5	255.7	51.7	11.7	82	34.5	2.7	-57.3	341.7	301	-40.7	70.3	sedimentary	0.7	3.0	Fetisova et al. (2018)		this study
SW England, Aylesbeare Mudstone	254.2	264.3	259.3	50.6	-3.4	81	22.4	3.4	-65.6	325.9	301	-50.9	76.7	sedimentary	0.49	3.82	Hounslow et al. (2016)		this study
Gonfaron 1, Lodeve	259.4	264.3	261.9	43.3	6.3	118	69.1	1.6	-54.0	348.9	301	-35.5	70.0	sedimentary	0.8	0.97	Evans et al. (2014)		this study
Sierra Chica, La Pampa	261.0	264.6	263.0	-37.5	-65.3	35	54.9	3.3	-80.1	349.0	290	-44.8	68.6	igneous			Domeier et al. (2011b)		T12
Upper Choiyoi Group, Mendoza	261.5	265.5	263.5	-34.7	-68.3	40	31.4	4.1	-73.7	315.6	290	-46.6	55.0	igneous			Domeier et al. (2011c)		T12
Gerrigong Volcanics	263.5	265.1	264.3	-34.6	150.8	17	16.3	9.1	-56.9	154.8	801	-47.2	58.5	igneous			Belica et al. (2017)		this study
Werrie Basalt	263.4	269.4	266.4	-31.9	151.0	9	10.8	16.4	-61.2	128.7	801	-34.9	49.7	igneous			Klootwijk et al. (2003)		this study
Tambillos, Uspallate Basin, Argentina	259.6	274.4	267.0	-32.2	290.5	16	33.5	6.5	-78.9	319.6	290	-48.2	62.4	igneous			Rapalini and Vilas (1991)	2475	T12
Lunner dikes, Norway	268.3	274.7	271.0	60.3	10.5	8	103.8	5.5	-52.9	344.4	301	-36.9	66.8	igneous			Torsvik et al. (1988)	3188	T12
Lunner dikes, Norway	268.3	274.7	271.0	60.3	10.5	25	68.7	3.5	-50.9	343.6	301	-36.0	64.5	igneous			Dominguez et al. (2011)		T12
Dome de Barrot, France	269.2	274.4	271.8	44.0	6.6	206	41.8	1.5	-47.2	324.5	301	-44.2	51.2	sedimentary	1	0	Haldan et al. (2009)		this study
Lodeve basin redbeds	264.3	283.3	273.8	43.7	3.4	146	33.3	2.1	-41.7	336.7	301	-33.9	52.1	sedimentary	0.8	0.79	Haldan et al. (2009)		this study
Bohemian Massif igneous, Germany	275.0	280.0	277.5	49.8	12.0	9	65.4	6.4	-42.3	345.9	301	-29.2	58.0	igneous			Soffel and Harzer (1991)	2356	T12
Scania melaphyre dikes, Sweden	274.0	282.0	278.0	55.7	13.7	8	35.9	9.4	-54.0	351.5	301	-34.3	71.2	igneous			Bylund (1974)	2222	T12
Jebel Nehoud Ring Complex, Kordofan, Sudan	278.0	282.0	280.0	14.9	30.5	8	102.7	5.5	-40.8	71.3	715	-41.2	71.2	igneous			Bachtadse et al. (2002)	3504	T12
Trachytes, Ukraine	280.0	285.2	282.6	37.2	37.8	19	54.9	4.6	-49.4	359.7	301	-27.4	71.4	igneous			Yuan et al. (2011)		T12
Exeter Lavas, UK	280.0	291.0	285.5	51.0	356.0	9	62.5	6.6	-48.0	343.0	301	-34.5	61.4	igneous			Cornwell (1967)	411	T12
Western Meseta, Morocco	277.0	294.6	285.8	33.0	353.6	18	27.1	6.8	-41.4	52.1	707	-41.1	53.9	igneous			Domeier et al. (2020)		this study
Black Forest volcanics, Germany	281.0	291.0	286.0	48.0	8.0	7	82.1	6.7	-51.6	359.6	301	-29.1	73.1	igneous			Konrad and Nairn (1972)	170	T12
Mauchline lavas, Scotland	279.0	293.0	286.0	55.5	-4.6	5	36.4	12.8	-46.2	348.0	301	-30.8	62.5	igneous			Harcombe-Smee et al. (1996)	3093	T12
Mount Leyshon Intrusive Complex, Australia	280.0	292.0	286.0	-20.3	146.3	34	16.4	6.3	-43.2	137.3	801	-33.0	72.2	igneous			Clark and Lackie (2003)		this study
Tuckers Igneous Complex, Australia	280.0	292.0	286.0	-20.1	146.5	42	11.5	6.8	-47.5	143.0	801	-38.3	69.2	igneous			Clark and Lackie (2003)		this study
NE Kazakhstan lavas 1	282.8	289.8	286.3	47.5	80.7	65	48.8	2.5	-33.2	338.2	301	-27.3	45.8	igneous			Bazhenov et al. (2014)		this study
NE Kazakhstan lavas 2	283.8	290.8	287.3	47.5	80.7	88	48.0	2.2	-44.1	340.6	301	-33.3	56.5	igneous			Bazhenov et al. (2016)		this study
Oslo Graben, Krokskogen and Vestfold	284.0	292.0	288.0	59.4	10.2	104	52.2	1.9	-48.2	335.5	301	-38.6	57.8	igneous			Haldan et al. (2014)		this study
Lodeve basin redbeds	283.3	293.5	288.4	43.7	3.4	143	98.2	1.2	-47.1	333.9	301	-38.9	55.9	sedimentary	0.8	0.68	Haldan et al. (2009)		this study
Saar–Nahe volcanics, Germany	288.0	293.0	290.5	49.5	7.0	11	20.8	10.2	-41.1	349.2	301	-26.6	59.0	igneous			Berthold et al. (1965)	712	T12
Nahe volcanics, Germany	288.0	293.0	290.5	50.0	8.0	5	104.8	7.5	-46.0	347.0	301	-31.2	61.8	igneous			Nijenhuis (1961)	940	T12
Itarare Group, Parana Basin, Brazil	283.3	298.9	291.1	-27.2	310.4	119	32.7	2.3	-63.2	347.5	201	-34.4	55.2	sedimentary	0.8	6.0	Franco et al. (2012)		this study
Scania dolerite dikes, Sweden	287.0	300.0	293.5	55.5	13.5	6	85.6	7.3	-37.0	354.0	301	-21.1	58.9	igneous			Mulder (1971)	2211	T12
Alnwick Sill, High Green and St. Oswalds Chapel Dyke (Whin Sill), UK	292.0	296.0	294.0	55.4	-1.6	17	47.1	7.7	-47.1	337.1	301	-37.1	57.5	igneous			Liss et al. (2004)		T12
Holy Island Sill and Dyke (Whin Sill), UK	292.0	296.0	294.0	55.7	-1.8	20	36.2	5.5	-35.4	346.8	301	-23.9	53.1	igneous			Liss et al. (2004)		T12
Silesia volcanics, Poland	285.0	305.0	295.0	50.6	16.1	8	41.0	8.8	-43.0	354.0	301	-25.5	63.3	igneous			Birkenmajer et al. (1968)	465	T12
Glenshaw Formation	298.9	307.0	303.0	40.5	280.0	23	16.1	7.8	-27.9	294.5	101	-31.0	27.6	sedimentary	0.7	0.58	Kodama (2009)		T12
Mafra Formation, Brazil	298.9	307.0	303.0	-26.1	310.2	111	55.9	1.8	-51.9	344.3	201	-25.4	47.0	sedimentary	1	0.0	Brandt et al. (2019)		this study
Moscovian, Murzuq basin, Algeria	307.0	315.2	311.1	23.6	11.9	113	25.4	2.7	-22.3	53.5	715	-22.8	53.1	sedimentary	0.6	3.1	Amenna et al. (2014)		this study
Tashkovska Donbas, Ukraine	315.2	323.4	319.3	48.8	38.6	84	35.4	2.6	-38.4	339.5	301	-30.1	50.9	sedimentary	0.7	1.7	Meijers et al. (2010)		T12
Newcastle range volcanics	315.6	328.2	321.9	-18.4	143.8	15	26.2	7.6	-63.4	125.0	801	-33.9	45.9	igneous			Anderson et al. (2003)	3561	T12
Magdalen Basin	315.2	330.3	322.8	46.2	298.7	262	12.4	2.6	-27.9	299.5	101	-28.3	31.6	sedimentary	0.60	1.5	Opdyke et al. (2014)		this study

Table 2. Paleomagnetic database used to compute the global apparent polar wander path for the last 320 Ma. NB: Data for the last 10 Ma from the PSV10 database are not included in this table. For the complete database, see Table S2.

Abbreviations: min_age and max_age = lower and upper boundaries of age uncertainty range; slat/slon = latitude and longitude of (mean) sampling location; N = number of paleomagnetic sites used to compute the paleopole; A95 = radius of the 95% confidence circle about the mean of the distribution of VGPs; K = Fisher (1953) precision parameter of the distribution of VGPs; plat/plon = paleopole latitude and longitude (south pole); plateID = plate identification number (see Fig. 2 and Table 1); Rlat/Rlon = paleopole latitude and longitude in coordinate frame of South Africa; f = flattening factor (only for sedimentary data), p_std = standard deviation of the assumed normal distributed co-latitudes, obtained from E/I correction (only for sedimentary data); DB = database in which entry is listed (T12 = Torsvik et al. (2012), PSV10 = Cromwell et al. (2018) or added in this study).

Window	Age	N	P95	Longitude	Latitude	Mean K	Mean CSD	Mean E
0	1.3	1811.5	0.7	313.2	-89.6	19.1	18.5	1.07
10	4.4	2609.7	1.3	334.1	-87.9	17.8	19.2	1.06
20	21.7	1156.7	1.1	9.4	-82.7	17.0	19.7	1.10
30	28.2	1091.0	1.0	23.2	-80.8	17.9	19.1	1.09
40	37.5	475.0	1.4	26.1	-79.6	19.6	18.3	1.14
50	56.1	1101.3	1.0	31.0	-75.2	16.3	20.1	1.11
60	60.0	1707.5	0.8	35.2	-73.7	16.4	20.0	1.08
70	64.7	896.5	1.1	39.1	-73.1	17.5	19.4	1.12
80	82.0	350.1	1.3	51.5	-72.6	29.9	14.8	1.16
90	89.7	412.9	1.2	64.9	-68.2	25.5	16.1	1.17
100	94.6	217.3	1.9	71.5	-64.2	22.8	17.0	1.21
110	114.7	259.5	1.5	80.7	-57.9	29.6	14.9	1.26
120	120.2	458.1	1.1	80.0	-55.0	29.3	15.0	1.18
130	131.0	798.2	0.8	82.7	-50.7	33.6	14.0	1.10
140	134.2	621.8	0.9	84.1	-50.0	34.7	13.8	1.12
150	152.4	144.3	2.8	83.7	-53.4	17.5	19.4	1.24
160	158.7	148.9	3.0	83.1	-55.8	14.6	21.2	1.24
170	172.6	112.5	3.5	78.6	-58.9	14.7	21.2	1.28
180	182.1	319.5	1.7	79.5	-64.2	19.0	18.6	1.29
190	189.7	470.1	1.4	75.3	-65.8	18.9	18.7	1.18
200	203.7	1399.0	1.8	63.5	-65.4	12.4	23.1	1.09
210	209.7	2287.7	1.3	58.1	-62.9	14.8	21.0	1.06
220	217.5	1583.0	1.1	53.8	-59.5	22.2	17.2	1.07
230	224.4	543.6	1.6	53.1	-56.7	23.0	16.9	1.12
240	242.5	215.4	2.9	58.3	-46.8	14.5	21.4	1.21
250	253.3	1017.2	2.1	61.7	-42.7	13.5	22.1	1.08
260	257.2	1200.3	1.6	62.4	-42.1	15.6	20.5	1.08
270	268.6	637.2	1.6	58.5	-41.0	26.6	15.7	1.13
280	281.3	819.1	1.3	56.2	-36.9	28.4	15.2	1.11
290	288.4	763.9	2.0	57.0	-34.6	28.4	15.2	1.18
300	297.8	405.8	2.5	52.1	-30.8	25.1	16.2	1.26
310	311.1	368.0	1.9	45.3	-26.6	18.6	18.8	1.42
320	320.3	427.9	2.4	39.8	-28.2	13.6	22.0	1.33

Table 3. Global APWP for the last 320 Ma in South African coordinates, calculated using a 20 Ma window. The center age of the window and the mean age of the re-sampled VGPs in that window are listed. N and P95 are the average number of re-sampled VGPs that fall within the time window and the 95% confidence region of the reference pole (in degrees). Mean K, CSD and E are the average Fisher (1953) precision parameter, circular standard deviation and elongation of the re-sampled VGPs.

			North America		South America		Eurasia		India		Australia		Antarctica		Pacific	
Window	**Age**	**P95**	**Plon**	**Plat**	**Plon**	**Plat**	**Plon**	**Plat**	**Plon**	**Plat**	**Plon**	**Plat**	**Plon**	**Plat**	**Plon**	**Plat**
0	1.3	0.7	313.2	-89.6	313.2	-89.6	313.2	-89.6	313.2	-89.6	313.2	-89.6	313.2	-89.6	313.2	-89.6
10	4.4	1.3	330.3	-87.5	290.2	-87.7	309.8	-87.6	90.4	-88.0	135.2	-86.3	298.1	-87.6	231.7	-86.6
20	21.7	1.1	356.6	-82.3	332.1	-84.6	350.3	-83.5	67.6	-81.7	98.5	-81.4	345.5	-84.2	277.7	-86.0
30	28.2	1.0	2.8	-80.9	329.1	-84.4	357.3	-82.8	88.9	-76.8	108.5	-75.1	353.4	-84.2	251.7	-86.0
40	37.5	1.4	355.2	-80.3	313.3	-83.5	345.0	-82.7	101.7	-72.7	114.7	-71.2	341.0	-84.4	238.3	-82.3
50	56.1	1.0	0.5	-76.5	328.3	-81.1	352.9	-79.7	101.2	-63.3	110.3	-68.1	3.9	-83.0	239.0	-80.0
60	60.0	0.8	7.1	-74.5	337.2	-80.8	354.3	-79.3	96.3	-52.6	112.9	-66.8	9.5	-83.8	220.7	-78.3
70	64.7	1.1	7.5	-74.7	337.2	-81.2	351.9	-79.6	98.8	-39.0	116.6	-65.9	13.0	-85.2	202.9	-73.0
80	82.0	1.3	12.6	-76.7	337.8	-84.1	359.3	-81.8	103.2	-31.8	125.7	-63.4	66.3	-88.9	187.1	-65.7
90	89.7	1.2	17.8	-77.8	9.2	-85.7	359.4	-83.1	111.7	-23.3	130.6	-58.9	150.0	-85.8		
100	94.6	1.9	14.6	-77.2	36.5	-84.3	357.9	-82.2	114.0	-17.6	135.6	-56.3	167.4	-82.8		
110	114.7	1.5	22.4	-74.5	57.7	-80.2	18.2	-80.9	116.0	-9.9	139.1	-51.2	166.3	-78.0		
120	120.2	1.1	12.1	-74.4	65.6	-85.4	4.3	-79.6	114.6	-8.2	145.5	-52.2	187.2	-76.9		
130	131.0	0.8	8.5	-71.7	70.4	-85.3	5.9	-76.6	115.7	-0.1	146.0	-47.0	178.6	-73.1		
140	134.2	0.9	4.7	-72.4	66.4	-83.9	359.9	-76.6	120.0	1.8	150.3	-44.5	183.5	-69.6		
150	152.4	2.8	349.1	-74.9	89.7	-86.7	338.6	-76.3	124.9	-2.6	160.2	-44.8	198.1	-65.4		
160	158.7	3.0	330.3	-75.8	137.6	-87.8	320.9	-74.4	128.8	-5.5	167.4	-44.3	205.8	-61.5		
170	172.6	3.5	303.0	-74.1	221.2	-86.5	303.0	-69.7	129.7	-9.8	173.0	-46.1	214.0	-59.8		
180	182.1	1.7	275.6	-73.9	215.1	-81.2	284.0	-67.0	133.7	-14.6	181.7	-45.1	220.2	-54.7		
190	189.7	1.4	268.0	-71.0	224.5	-79.4	280.2	-63.6	133.1	-17.0	184.3	-46.7	224.4	-54.5		
200	203.7	1.8	268.4	-65.3	247.2	-77.4	286.0	-58.7	128.6	-19.7	185.2	-51.6	231.8	-57.1		
210	209.7	1.3	273.0	-62.5	262.4	-76.9	294.0	-56.8	125.0	-19.7	182.6	-54.6	234.9	-60.1		
220	217.5	1.1	278.5	-59.5	278.6	-75.8	303.0	-54.8	120.8	-19.0	178.2	-57.7	238.3	-63.8		
230	224.4	1.6	283.2	-58.1	289.9	-75.4	307.5	-53.7	118.3	-17.5	173.4	-59.0	238.8	-66.6		
240	242.5	2.9	301.7	-55.8	330.2	-74.4	324.8	-52.9	113.4	-8.3	154.2	-57.0	222.3	-75.5		
250	253.3	2.1	310.1	-55.1	346.6	-73.0	332.7	-53.0	112.5	-3.7	147.4	-54.1	203.6	-77.6		
260	257.2	1.6	311.5	-55.0	349.2	-72.7	334.0	-53.0	112.4	-3.0	146.6	-53.5	199.9	-77.7		
270	268.6	1.6	309.6	-52.1	343.8	-70.2	333.0	-50.0	109.5	-4.1	143.6	-56.1	207.1	-80.5		
280	281.3	1.3	312.1	-48.0	345.9	-65.8	336.4	-46.2	105.4	-2.4	135.7	-56.9	196.1	-84.8		
290	288.4	2.0	315.2	-46.8	350.1	-64.2	339.6	-45.3	104.3	-0.3	132.1	-55.5	168.6	-85.3		
300	297.8	2.5	314.3	-41.2	346.5	-58.8	339.8	-39.7	98.7	-0.4	122.9	-57.8	72.4	-87.5		
310	311.1	1.9	311.9	-34.1	341.3	-52.1	338.5	-32.4	91.4	-1.8	109.8	-60.9	20.4	-81.4		
320	320.3	2.4	306.0	-32.4	333.2	-50.8	333.0	-30.1	89.4	-6.6	106.9	-65.9	354.2	-78.7		

Table 4. Global APWP (20 Ma window) rotated into the coordinate frame of other major tectonic plates. See Table 3 for more information.